

Measurements of Higgs boson production and couplings in the four-lepton channel in pp collisions at center-of-mass energies of 7 and 8 TeV with the ATLAS detector

G. Aad *et al.*^{*}

(ATLAS Collaboration)

(Received 22 August 2014; published 16 January 2015)

The final ATLAS Run 1 measurements of Higgs boson production and couplings in the decay channel $H \rightarrow ZZ^* \rightarrow \ell^+\ell^-\ell'^+\ell'^-$, where $\ell, \ell' = e$ or μ , are presented. These measurements were performed using pp collision data corresponding to integrated luminosities of 4.5 and 20.3 fb^{-1} at center-of-mass energies of 7 and 8 TeV, respectively, recorded with the ATLAS detector at the LHC. The $H \rightarrow ZZ^* \rightarrow 4\ell$ signal is observed with a significance of 8.1 standard deviations, with an expectation of 6.2 standard deviations, at $m_H = 125.36$ GeV, the combined ATLAS measurement of the Higgs boson mass from the $H \rightarrow \gamma\gamma$ and $H \rightarrow ZZ^* \rightarrow 4\ell$ channels. The production rate relative to the Standard Model expectation, the signal strength, is measured in four different production categories in the $H \rightarrow ZZ^* \rightarrow 4\ell$ channel. The measured signal strength, at this mass, and with all categories combined, is $1.44^{+0.40}_{-0.33}$. The signal strength for Higgs boson production in gluon fusion or in association with $t\bar{t}$ or $b\bar{b}$ pairs is found to be $1.7^{+0.5}_{-0.4}$, while the signal strength for vector-boson fusion combined with WH/ZH associated production is found to be $0.3^{+1.6}_{-0.9}$.

DOI: 10.1103/PhysRevD.91.012006

PACS numbers: 14.80.Bn

I. INTRODUCTION

In the Standard Model (SM) the Brout-Englert-Higgs (BEH) mechanism is the source of electroweak symmetry breaking and results in the appearance of a fundamental scalar particle, the Higgs boson [1–3]. The ATLAS and CMS experiments have reported the observation of a particle in the search for the SM Higgs boson [4,5], where the most sensitive channels are $H \rightarrow ZZ^* \rightarrow 4\ell$, $H \rightarrow WW^* \rightarrow \ell\nu\ell\nu$ and $H \rightarrow \gamma\gamma$. An important step in the confirmation of the new particle as the SM Higgs boson is the measurement of its properties, which are completely defined in the SM once its mass is known. Previous ATLAS studies [6,7] have shown that this particle is consistent with the SM Higgs boson.

The Higgs boson decay to four leptons, $H \rightarrow ZZ^* \rightarrow 4\ell$, where $\ell = e$ or μ , provides good sensitivity for the measurement of the Higgs boson properties due to its high signal-to-background ratio, which is about 2 for each of the four final states: $\mu^+\mu^-\mu^+\mu^-$ (4μ), $e^+e^-\mu^+\mu^-$ ($2e2\mu$), $\mu^+\mu^-e^+e^-$ ($2\mu2e$), and $e^+e^-e^+e^-$ ($4e$), where the first lepton pair is defined to be the one with the dilepton invariant mass closest to the Z boson mass. The contribution to these final states from $H \rightarrow ZZ^*$, $Z^{(*)} \rightarrow \tau^+\tau^-$ decays is below the per mille level in the current analysis. The largest background in this search comes from continuum ($Z^{(*)}/\gamma^*$)($Z^{(*)}/\gamma^*$) production, referred to as ZZ^* hereafter. For the four-lepton events with an invariant

mass, $m_{4\ell}$, below about 160 GeV, there are also important background contributions from $Z + \text{jets}$ and $t\bar{t}$ production with two prompt leptons, where the additional charged lepton candidates arise from decays of hadrons with b - or c -quark content, from photon conversions or from mis-identification of jets.

Interference effects are expected between the Higgs boson signal and SM background processes. For the $H \rightarrow ZZ^* \rightarrow 4\ell$ channel, the impact of this interference on the mass spectrum near the resonance is negligible [8]. This analysis does not account for interference effects in the mass spectra.

In the SM, the inclusive production of the $H \rightarrow ZZ^* \rightarrow 4\ell$ final state is dominated by the gluon fusion (ggF) Higgs boson production mode, which represents 86% of the total production cross section for $m_H = 125$ GeV at $\sqrt{s} = 8$ TeV. Searching for Higgs boson production in the vector-boson fusion (VBF) and the vector-boson associated production (VH) modes allows further exploration of the coupling structure of the new particle. The corresponding fractions of the production cross section for VBF and VH are predicted to be 7% and 5%, respectively.

This paper presents the final ATLAS Run 1 results of the measurement of the SM Higgs boson production in the $H \rightarrow ZZ^* \rightarrow 4\ell$ decay mode, where the production is studied both inclusively and with events categorized according to the characteristics of the different production modes. The categorized analysis allows constraints to be placed on possible deviations from the expected couplings of the SM Higgs boson. The data sample used corresponds to an integrated luminosity of 4.5 fb^{-1} at a center-of-mass energy of 7 TeV and 20.3 fb^{-1} at a center-of-mass energy of 8 TeV, collected in the years 2011 and 2012, respectively.

* Full author list given at the end of the article.

Published by the American Physical Society under the terms of the Creative Commons Attribution 3.0 License. Further distribution of this work must maintain attribution to the author(s) and the published articles title, journal citation, and DOI.

The method adopted to extract the production rates simultaneously provides a measurement of the Higgs boson mass. The measurement of the Higgs boson mass for this channel, performed in combination with the $H \rightarrow \gamma\gamma$ decay mode, is discussed in Ref. [9] and is only covered briefly here. This paper contains a full description of the signal and background simulation, the object reconstruction and identification, the event selection and the background estimations of the $H \rightarrow ZZ^* \rightarrow 4\ell$ decay mode, providing the details for other Run 1 final results, including the combined mass measurement, reported elsewhere. The corresponding final Run 1 CMS results for the $H \rightarrow ZZ^* \rightarrow 4\ell$ decay mode have been reported in Ref. [10].

The present analysis improves on the earlier result [6] with the following changes: (a) the electron identification uses a multivariate likelihood instead of a cut-based method, improving the background rejection at a fixed efficiency; (b) the electron transverse energy (E_T) measurement has been improved by a refined cluster energy reconstruction in the calorimeter and by combining the electron cluster energy with the track momentum for low- E_T electrons; (c) the energy scale for electrons and momentum scale for muons have both been improved; (d) the inclusion of final-state radiation (FSR) off charged leptons has been extended to noncollinear photons; (e) a multivariate discriminant against the ZZ^* background has been introduced to improve the signal-to-background ratio for the ggF production mode; (f) the estimates of the reducible $\ell\ell + \text{jets}$ and $t\bar{t}$ background processes have been improved; (g) the sensitivity for different production modes has been improved, both by introducing a new VH category with two jets in the final state and by using multivariate techniques for this category and the VBF category.

The ATLAS detector is briefly described in Sec. II, and the signal and background simulation is presented in Sec. III. The object reconstruction and identification, the event selection and categorization, and the background estimation are presented in Secs. IV, V and VI, respectively. The multivariate discriminants and the signal and background modeling are discussed in Secs. VII and VIII. Finally, the systematic uncertainties and the results are presented in Secs. IX and X.

II. THE ATLAS DETECTOR

The ATLAS detector [11] is a multipurpose particle detector with approximately forward-backward symmetric cylindrical geometry.¹ The inner tracking detector (ID)

¹The ATLAS experiment uses a right-handed coordinate system with its origin at the nominal interaction point (IP) in the center of the detector and the z -axis along the beam pipe. The x -axis points from the IP to the center of the LHC ring, and the y -axis points upward. Cylindrical coordinates (r, ϕ) are used in the transverse plane, ϕ being the azimuthal angle around the beam pipe. The pseudorapidity is defined in terms of the polar angle θ as $\eta = -\ln \tan(\theta/2)$.

consists of a silicon pixel detector, which is closest to the interaction point, and a silicon microstrip detector surrounding the pixel detector, both covering $|\eta| < 2.5$, followed by a transition radiation straw-tube tracker (TRT) covering $|\eta| < 2$. The ID is surrounded by a thin superconducting solenoid providing a 2 T axial magnetic field. A highly segmented lead/liquid-argon (LAr) sampling electromagnetic calorimeter measures the energy and the position of electromagnetic showers with $|\eta| < 3.2$. The LAr calorimeter includes a presampler (for $|\eta| < 1.8$) and three sampling layers, longitudinal in shower depth, for $|\eta| < 2.5$. LAr sampling calorimeters are also used to measure hadronic showers in the end-caps ($1.5 < |\eta| < 3.2$) and electromagnetic and hadronic showers in the forward ($3.1 < |\eta| < 4.9$) regions, while an iron/scintillator tile calorimeter measures hadronic showers in the central region ($|\eta| < 1.7$).

The muon spectrometer (MS) surrounds the calorimeters and is designed to detect muons in the pseudorapidity range up to $|\eta| = 2.7$. The MS consists of one barrel ($|\eta| < 1.05$) and two end-cap regions. A system of three large superconducting air-core toroid magnets, each with eight coils, provides a magnetic field with a bending integral of about 2.5 T m in the barrel and up to 6 T m in the end-caps. Monitored drift-tube chambers in both the barrel and end cap regions and cathode strip chambers covering $|\eta| > 2$ are used as precision chambers, whereas resistive plate chambers in the barrel and thin gap chambers in the end caps are used as trigger chambers, covering up to $|\eta| = 2.4$. The chambers are arranged in three layers, so high- p_T particles traverse at least three stations with a lever arm of several meters.

A three-level trigger system selects events to be recorded for offline analysis.

III. SIGNAL AND BACKGROUND SIMULATION

The $H \rightarrow ZZ^* \rightarrow 4\ell$ signal is modeled using the Powheg-Box Monte Carlo (MC) event generator [12–16], which provides separate calculations for the ggF and VBF production mechanisms with matrix elements up to next-to-leading order (NLO) in the QCD coupling constant. The description of the Higgs boson transverse momentum (p_T) spectrum in the ggF process is reweighted to follow the calculation of Refs. [17,18], which includes QCD corrections up to next-to-next-to-leading order (NNLO) and QCD soft-gluon resummations up to next-to-next-to-leading logarithm (NNLL). The effects of non-zero quark masses are also taken into account [19]. Powheg-Box is interfaced to PYTHIA8.1 [20,21] for showering and hadronization, which in turn is interfaced to PHOTOS [22,23] for QED radiative corrections in the final state. PYTHIA8.1 is used to simulate the production of a Higgs boson in association with a W or a Z boson (VH) or with a $t\bar{t}$ pair ($t\bar{t}H$). The production of a Higgs boson in association with a $b\bar{b}$ pair ($b\bar{b}H$) is included in the signal

yield assuming the same m_H dependence as for the $t\bar{t}H$ process, while the signal efficiency is assumed to be equal to that for ggF production.

The Higgs boson production cross sections and decay branching ratios, as well as their uncertainties, are taken from Refs. [24,25]. The cross sections for the ggF process have been calculated to NLO [26–28] and NNLO [29–31] in QCD. In addition, QCD soft-gluon resummations calculated in the NNLL approximation are applied for the ggF process [32]. NLO electroweak (EW) radiative corrections are also applied [33,34]. These results are compiled in Refs. [35–37] assuming factorization between QCD and EW corrections. For the VBF process, full QCD and EW corrections up to NLO [38–40] and approximate NNLO QCD [41] corrections are used to calculate the cross section. The cross sections for the associated WH/ZH production processes are calculated at NLO [42] and at NNLO [43] in QCD, and NLO EW radiative corrections are applied [44]. The cross section for associated Higgs boson production with a $t\bar{t}$ pair is calculated at NLO in QCD [45–48]. The cross section for the $b\bar{b}H$ process is calculated in the four-flavor scheme at NLO in QCD [49–51] and in the five-flavor scheme at NNLO in QCD [52] and combined via the Santander matching scheme [25,53].

The Higgs boson decay widths for the WW and ZZ four-lepton final states are provided by PROPHECY4F [54,55], which includes the complete NLO QCD + EW corrections and interference effects between identical final-state fermions. The other Higgs boson decay widths, e.g. $\gamma\gamma$, $\tau\tau$, $b\bar{b}$, etc., are obtained with HDECAY [56] and combined with the PROPHECY4F results to obtain the $H \rightarrow ZZ^* \rightarrow 4\ell$ branching ratios. Table I gives the production cross sections and branching ratios for $H \rightarrow ZZ^* \rightarrow 4\ell$, which are used to normalize the signal simulation, for several values of m_H .

The QCD scale uncertainties for $m_H = 125$ GeV [24] amount to $+7\%$ and -8% for the ggF process, from $\pm 1\%$ to $\pm 2\%$ for the VBF and associated WH/ZH production

processes and $+4\%$ and -9% for the associated $t\bar{t}H$ production process. The uncertainties on the production cross section due to uncertainties on the parton distribution functions (PDF) and the strong coupling constant, α_s , is $\pm 8\%$ for gluon-initiated processes and $\pm 4\%$ for quark-initiated processes, estimated by following the prescription in Ref. [57] and by using the PDF sets of CTEQ [58], MSTW [59] and NNPDF [60]. The PDF uncertainties are assumed to be 100% correlated among processes with identical initial states, regardless of whether they are signal or background [61].

The ZZ^* continuum background is modeled using Powheg-Box [62] for quark-antiquark annihilation and GG2ZZ [63] for gluon fusion. The PDF + α_s and QCD scale uncertainties are parametrized as functions of $m_{4\ell}$ as recommended in Ref. [25]. For the ZZ^* background at $m_{4\ell} = 125$ GeV, the quark-initiated (gluon-initiated) processes have a QCD scale uncertainty of $\pm 5\%$ ($\pm 25\%$), and $\pm 4\%$ ($\pm 8\%$) for the PDF and α_s uncertainties, respectively.

The $Z +$ jets production is modeled using ALPGEN [64] and is divided into two sources: $Z +$ light-jets, which includes $Zc\bar{c}$ in the massless c -quark approximation and $Zb\bar{b}$ with $b\bar{b}$ from parton showers, and $Zb\bar{b}$ using matrix-element calculations that take into account the b -quark mass. The MLM [65] matching scheme is used to remove any double counting of identical jets produced via the matrix-element calculation and the parton shower, but this scheme is not implemented for b -jets. Therefore, $b\bar{b}$ pairs with separation $\Delta R \equiv \sqrt{(\Delta\phi)^2 + (\Delta\eta)^2} > 0.4$ between the b -quarks are taken from the matrix-element calculation, whereas for $\Delta R < 0.4$ the parton-shower $b\bar{b}$ pairs are used. In this search the $Z +$ jets background is normalized using control samples from data. For comparison between data and simulation, the NNLO QCD FEWZ [66,67] and NLO QCD MCFM [68,69] cross-section calculations are used to normalize the simulations for inclusive Z boson and $Zb\bar{b}$ production, respectively. The $t\bar{t}$ background is modeled

TABLE I. Calculated SM Higgs boson production cross sections for gluon fusion, vector-boson fusion and associated production with a W or Z boson or with a $b\bar{b}$ or $t\bar{t}$ pair in pp collisions at \sqrt{s} of 7 and 8 TeV [24]. The quoted uncertainties correspond to the total theoretical systematic uncertainties calculated by adding in quadrature the QCD scale and PDF + α_s uncertainties. The decay branching ratio (B) for $H \rightarrow 4\ell$ with $\ell = e, \mu$, is reported in the last column [24].

m_H (GeV)	$\sigma(gg \rightarrow H)$ (pb)	$\sigma(qq' \rightarrow Hqq')$ (pb)	$\sigma(q\bar{q} \rightarrow WH)$ (pb)	$\sigma(q\bar{q} \rightarrow ZH)$ (pb)	$\sigma(q\bar{q}/gg \rightarrow b\bar{b}H/t\bar{t}H)$ (pb)	$B(H \rightarrow ZZ^* \rightarrow 4\ell)$ (10^{-3})
$\sqrt{s} = 7$ TeV						
123	15.6 ± 1.6	1.25 ± 0.03	0.61 ± 0.02	0.35 ± 0.01	0.26 ± 0.04	0.103 ± 0.005
125	15.1 ± 1.6	1.22 ± 0.03	0.58 ± 0.02	0.34 ± 0.01	0.24 ± 0.04	0.125 ± 0.005
127	14.7 ± 1.5	1.20 ± 0.03	0.55 ± 0.02	0.32 ± 0.01	0.23 ± 0.03	0.148 ± 0.006
$\sqrt{s} = 8$ TeV						
123	19.9 ± 2.1	1.61 ± 0.05	0.74 ± 0.02	0.44 ± 0.02	0.35 ± 0.05	0.103 ± 0.005
125	19.3 ± 2.0	1.58 ± 0.04	0.70 ± 0.02	0.42 ± 0.02	0.33 ± 0.05	0.125 ± 0.005
127	18.7 ± 1.9	1.55 ± 0.04	0.67 ± 0.02	0.40 ± 0.02	0.32 ± 0.05	0.148 ± 0.006

using POWHEG-BOX interfaced to PYTHIA8.1 for parton shower and hadronization, PHOTOS for QED radiative corrections and TAUOLA [70,71] for the simulation of τ lepton decays. SHERPA [72] is used for the simulation of WZ production.

Generated events are processed through the ATLAS detector simulation [73] within the GEANT4 framework [74]. Additional $p\bar{p}$ interactions in the same and nearby bunch crossings (pileup) are included in the simulation. The simulation samples are weighted to reproduce the observed distribution of the mean number of interactions per bunch crossing in the data.

IV. OBJECT RECONSTRUCTION AND IDENTIFICATION

The $H \rightarrow ZZ^* \rightarrow 4\ell$ channel has a small rate but is a relatively clean final state where the signal-to-background ratio *vis-à-vis* the reducible backgrounds alone, i.e. ignoring the ZZ^* background, is above 6 for the present analysis. Significant effort was made to obtain a high efficiency for the reconstruction and identification of electrons and muons, while keeping the loss due to background rejection as small as possible. In particular, this becomes increasingly difficult for electrons as E_T decreases.

Electrons are reconstructed using information from the ID and the electromagnetic calorimeter. For electrons, background discrimination relies on the shower shape information available from the highly segmented LAr EM calorimeter, high-threshold TRT hits, as well as compatibility of the tracking and calorimeter information. Muons are reconstructed as tracks in the ID and MS, and their identification is primarily based on the presence of a matching track or tag in the MS. Finally, jets are reconstructed from clusters of calorimeter cells and calibrated using a dedicated scheme designed to adjust the energy measured in the calorimeter to that of the true jet energy on average.

A. Electron reconstruction and identification

Electron candidates are clusters of energy deposited in the electromagnetic calorimeter associated with ID tracks [75,76]. All candidate electron tracks are fitted using a Gaussian-sum filter [77] (GSF) to account for bremsstrahlung energy losses. The GSF fit brings the candidate electron E/p distribution closer to unity and improves the measured electron direction, resulting in better impact parameter resolution. For the 2012 (8 TeV) data set, the electron reconstruction was modified to allow for large bremsstrahlung energy losses. A second pass was added to the ATLAS track pattern recognition that allows for an electron hypothesis with larger energy loss to be tried after a first pass with a pion hypothesis. Furthermore, the track-to-cluster matching algorithm was improved, for example by incorporating an additional test that extrapolates tracks

to the calorimeter using the measured cluster energy rather than the track momentum. These improvements increased the electron reconstruction efficiency on average by 5% for electrons with E_T above 15 GeV, with a 7% improvement for E_T at 15 GeV, as measured with data [78].

The electron identification is based on criteria that require the longitudinal and transverse shower profiles to be consistent with those expected for electromagnetic showers, the track and cluster positions to match in η and ϕ , and the presence of high-threshold TRT hits. To maintain both large acceptance and good discrimination, the selection is kept “loose” for a large number of discriminating variables; for comparison, the most stringent electron identification would induce an additional 15% reduction in electron efficiency. Compared to the previous measurement [6], the electron identification was improved for the 2012 data set by moving from a cut-based method to a likelihood method. The likelihood allows the inclusion of discriminating variables that are difficult to use with explicit cuts without incurring significant efficiency losses. For example, the GSF fit measures a significant difference between the momenta at the start and end of the electron trajectory for only a fraction of true electrons so that requiring a large difference for all electrons would not be an efficient selection cut. The likelihood improves the rejection of light-flavor jets and photon conversions by a factor of 2 for the same signal efficiency. For the 2011 (7 TeV) data set, the electron reconstruction proceeds as described above, but without the improved pattern recognition and cluster-to-track matching. The electron identification used for the 2011 data set is the same cut-based identification as in the previous measurement [6]. Detailed descriptions of the likelihood identification used for the 2012 data set, the cut-based identification used for the 2011 data set and the corresponding efficiency measurements can be found in Refs. [78,79].

Finally, the electron transverse energy is computed from the cluster energy and the track direction at the interaction point. The cluster energy is the sum of the calibrated energy deposited in the cells in a fixed-size window in $\eta \times \phi$, different for the barrel and end-cap. The cluster energy is corrected for energy lost before the calorimeter, deposited in neighboring cells and beyond the calorimeter. Further corrections for the response dependence are applied as a function of the impact point within the central cluster cell. The cluster energy measurement was improved compared to the previous analysis [6] and is described elsewhere [76]. Several of the steps in the energy calibration were significantly improved including: (a) the addition of a multivariate technique to extract the cluster energy from the energy deposit in simulation, (b) additional corrections for response details not included in the simulation, and (c) equalization of the energy scales of the longitudinal calorimeter layers.

These improvements resulted in a significant reduction in the overall energy scale uncertainty (for example for

$|\eta| < 1.37$ the uncertainty is reduced from 0.4% to 0.04% for electrons of $E_T = 40$ GeV [76]) and have an important impact on the systematic uncertainty of the Higgs boson mass measurement [9]. In addition, a combined fit of the cluster energy and track momentum is applied to electrons with E_T below 30 GeV when the cluster E_T and the track p_T agree within their uncertainties. The combined fit improves the resolution of $m_{4\ell}$ for the $4e$ and $2\mu 2e$ final states by about 4%.

B. Muon reconstruction and identification

Four types of muon candidates are distinguished, depending on how they are reconstructed. Most muon candidates are identified by matching a reconstructed ID track with either a complete or partial track reconstructed in the MS [80,81]. If a complete MS track is present, the two independent momentum measurements are combined (combined muons); otherwise the momentum is measured using the ID, and the partial MS track serves as identification (segment-tagged muons). The muon reconstruction and identification coverage is extended by using tracks reconstructed in the forward region ($2.5 < |\eta| < 2.7$) of the MS, which is outside the ID coverage (standalone muons). In the center of the barrel region ($|\eta| < 0.1$), which lacks MS geometrical coverage, ID tracks with $p_T > 15$ GeV are identified as muons if their calorimetric energy deposition is consistent with a minimum ionizing particle (calorimeter-tagged muons). The inner detector tracks associated with muons that are identified inside the ID acceptance are required to have a minimum number of associated hits in each of the ID subdetectors to ensure good track reconstruction. The muon candidates outside the ID acceptance that are reconstructed only in the MS are required to have hits in each of the three stations they traverse. At most one standalone or calorimeter-tagged muon is used per event.

C. Final-state radiation recovery

The QED process of radiative photon production in Z decays is well modeled by simulation. Some of the FSR photons can be identified in the calorimeter and incorporated into the four-lepton measurement. A dedicated method to include the FSR photons in the reconstruction of Z bosons was developed. This method includes a search for collinear and noncollinear FSR photons, with the collinear search described in Ref. [82]. Collinear photons are only associated with muons² ($\Delta R_{\text{cluster},\mu} \leq 0.15$), and noncollinear photons can be associated with either muons or electrons ($\Delta R_{\text{cluster},\ell} > 0.15$).

At most one FSR photon is used per event, with priority given to collinear photons. The probability of having more

than one FSR per event with significant energy is negligible. The collinear photons are required to have a transverse energy of $E_T > 1.5$ GeV and a fraction of the total energy deposited in the front sampling layer of the calorimeter greater than 0.1. If more than one collinear photon is found, only the one with the highest E_T is kept. Noncollinear photons must have $E_T > 10$ GeV, be isolated (E_T below 4 GeV within a cone of size $\Delta R = 0.4$, excluding the photon itself), and satisfy strict (“tight”) identification criteria [83]. Again, only the highest- E_T noncollinear photon is retained, and only if no collinear photon is found.

The inclusion of a FSR photon in a four-lepton event is discussed below in Sec. V A. The collinear FSR selection recovers 70% of the FSR photons within the selected fiducial region with a purity of about 85%, where misidentified photons come from pileup and muon ionization. The noncollinear FSR selection has an efficiency of approximately 60% and a purity greater than 95% within the fiducial region.

In Fig. 1, the invariant mass distributions are shown for $Z \rightarrow \mu^+ \mu^-$ candidate events where either a collinear [Fig. 1(a)] or noncollinear [Fig. 1(b)] FSR photon is found. The invariant mass distributions are shown both before and after the addition of the FSR photons, for both data and simulation. Good agreement between data and simulation is observed.

D. Jet reconstruction

Jets are reconstructed using the anti- k_t algorithm [84,85] with a distance parameter $R = 0.4$. The inputs to the reconstruction are three-dimensional clusters of energy [86,87] in the calorimeter, calibrated to the electromagnetic energy scale and corrected for contributions from in-time and out-of-time pileup [88], and the position of the primary interaction vertex (see Sec. V). The algorithm for this clustering suppresses noise by keeping only cells with a significant energy deposit and their neighboring cells. Subsequently, the jets are calibrated to the hadronic energy scale using p_T - and η -dependent correction factors determined from simulation (2011 data set) and from data (2012 data set) [87,89]. The uncertainty on these correction factors is determined from control samples in data. To reduce the number of jet candidates originating from pileup vertices, jets with $p_T < 50$ GeV within the ID acceptance ($|\eta| < 2.4$) are required to have more than 50% (75% for 2011 data) of the summed scalar p_T of the tracks associated with the jet (within $\Delta R = 0.4$ around the jet axis) come from tracks of the primary vertex [90].

V. EVENT SELECTION

The data are subjected to quality requirements: if any relevant detector component is not operating correctly during a period when an event is recorded, the event is

²Photons collinear to electrons are included in the calorimeter shower.

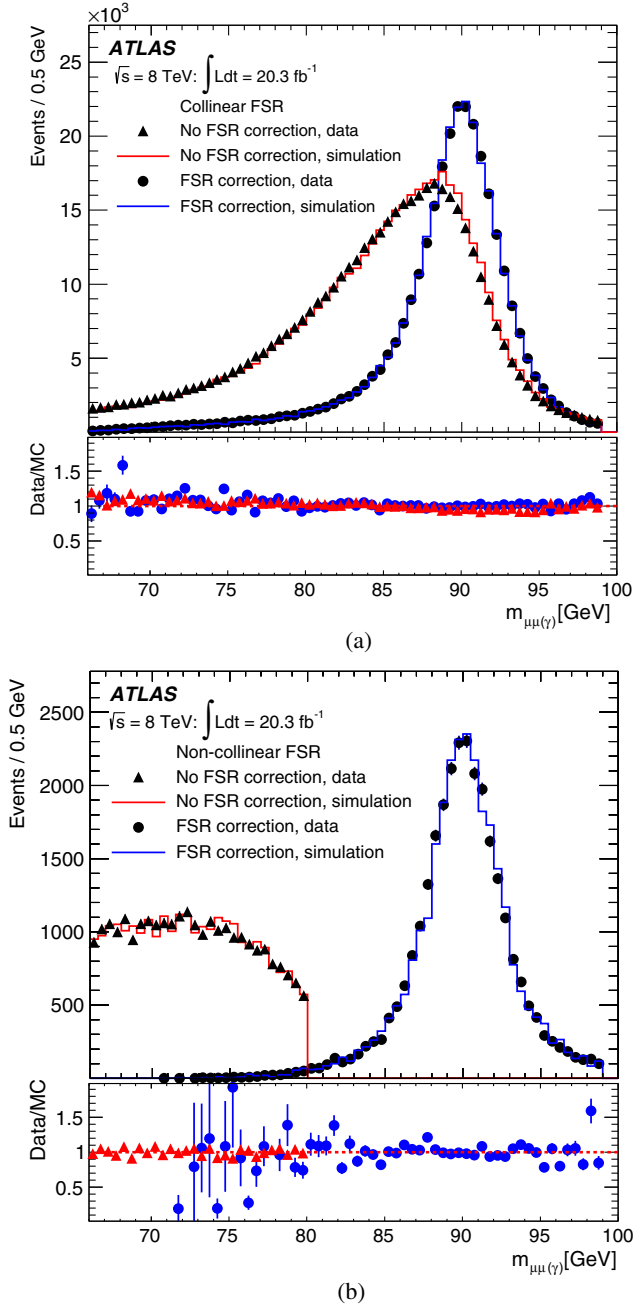


FIG. 1 (color online). (a) The invariant mass distributions of $Z \rightarrow \mu^+\mu^-(\gamma)$ events in data before collinear FSR correction (filled triangles) and after collinear FSR correction (filled circles), for events with a collinear FSR photon satisfying the selection criteria as described in Sec. IV C. The prediction of the simulation is shown before correction (red histogram) and after correction (blue histogram). (b) The invariant mass distributions of $Z \rightarrow \mu^+\mu^-(\gamma)$ events with a noncollinear FSR photon satisfying the selection criteria as described in Sec. IV C. The prediction of the simulation is shown before correction (red histogram) and after correction (blue histogram).

rejected. Events are required to have at least one vertex with three associated tracks with $p_T > 400$ MeV, and the primary vertex is chosen to be the reconstructed vertex with the largest track $\sum p_T^2$. Identical requirements are

applied to all four-lepton final states. For the inclusive analysis, four-lepton events are selected and classified according to their channel: 4μ , $2e2\mu$, $2\mu2e$, $4e$. These events are subsequently categorized according to their production mechanism to provide measurements of each corresponding signal strength.

A. Inclusive analysis

Four-lepton events were selected with single-lepton and dilepton triggers. The p_T (E_T) thresholds for single-muon (single-electron) triggers increased from 18 to 24 GeV (20 to 24 GeV) between the 7 and 8 TeV data, in order to cope with the increasing instantaneous luminosity. The dilepton trigger thresholds for 7 TeV data are set at 10 GeV p_T for muons, 12 GeV E_T for electrons and (6, 10) GeV for (muon, electron) mixed-flavor pairs. For the 8 TeV data, the thresholds were raised to 13 GeV for the dimuon trigger, to 12 GeV for the dielectron trigger and (8, 12) GeV for the (muon, electron) trigger; furthermore, a dimuon trigger with different thresholds on the muon p_T , 8 and 18 GeV, was added. The trigger efficiency for events passing the final selection is above 97% in the 4μ , $2\mu2e$ and $2e2\mu$ channels and close to 100% in the $4e$ channel for both 7 and 8 TeV data.

Higgs boson candidates are formed by selecting two same-flavor, opposite-sign lepton pairs (a lepton quadruplet) in an event. Each lepton is required to have a longitudinal impact parameter less than 10 mm with respect to the primary vertex, and muons are required to have a transverse impact parameter of less than 1 mm to reject cosmic-ray muons. These selections are not applied to standalone muons that have no ID track. Each electron (muon) must satisfy $E_T > 7$ GeV ($p_T > 6$ GeV) and be measured in the pseudorapidity range $|\eta| < 2.47$ ($|\eta| < 2.7$). The highest- p_T lepton in the quadruplet must satisfy $p_T > 20$ GeV, and the second (third) lepton in p_T order must satisfy $p_T > 15$ GeV ($p_T > 10$ GeV). Each event is required to have the triggering lepton(s) matched to one or two of the selected leptons.

Multiple quadruplets within a single event are possible: for four muons or four electrons there are two ways to pair the masses, and for five or more leptons there are multiple ways to choose the leptons. Quadruplet selection is done separately in each subchannel: 4μ , $2e2\mu$, $2\mu2e$, $4e$, keeping only a single quadruplet per channel. For each channel, the lepton pair with the mass closest to the Z boson mass is referred to as the leading dilepton and its invariant mass, m_{12} , is required to be between 50 and 106 GeV. The second, subleading, pair of each channel is chosen from the remaining leptons as the pair closest in mass to the Z boson and in the range $m_{\min} < m_{34} < 115$ GeV, where m_{\min} is 12 GeV for $m_{4\ell} < 140$ GeV, rises linearly to 50 GeV at $m_{4\ell} = 190$ GeV and then remains at 50 GeV for $m_{4\ell} > 190$ GeV. Finally, if more than one channel has a quadruplet passing the selection, the channel with the highest expected signal rate is kept, i.e. in the order 4μ ,

$2e2\mu$, $2\mu2e$, $4e$. The rate of two quadruplets in one event is below the per mille level.

Events with a selected quadruplet are required to have their leptons a distance $\Delta R > 0.1$ from each other if they are of the same flavor and $\Delta R > 0.2$ otherwise. For 4μ and $4e$ events, if an opposite-charge same-flavor dilepton pair is found with $m_{\ell\ell}$ below 5 GeV the event is removed.

The $Z + \text{jets}$ and $t\bar{t}$ background contributions are further reduced by applying impact parameter requirements as well as track- and calorimeter-based isolation requirements to the leptons. The transverse impact parameter significance, defined as the impact parameter in the transverse plane divided by its uncertainty, $|d_0|/\sigma_{d_0}$, for all muons (electrons) is required to be lower than 3.5 (6.5). The normalized track isolation discriminant, defined as the sum of the transverse momenta of tracks, inside a cone of size $\Delta R = 0.2$ around the lepton, excluding the lepton track, divided by the lepton p_T , is required to be smaller than 0.15.

The relative calorimetric isolation for electrons in the 2012 data set is computed as the sum of the cluster transverse energies E_T , in the electromagnetic and hadronic calorimeters, with a reconstructed barycenter inside a cone of size $\Delta R = 0.2$ around the candidate electron cluster, divided by the electron E_T . The electron relative calorimetric isolation is required to be smaller than 0.2. The cells within 0.125×0.175 in $\eta \times \phi$ around the electron barycenter are excluded. The pileup and underlying event contribution to the calorimeter isolation is subtracted event by event [91]. The calorimetric isolation of electrons in the 2011 data set is cell based (electromagnetic and hadronic calorimeters) rather than cluster based, and the calorimeter isolation relative to the electron E_T requirement is 0.3 instead of 0.2. In the case of muons, the relative calorimetric isolation discriminant is defined as the sum, ΣE_T , of the calorimeter cells above 3.4σ , where σ is the quadrature sum of the expected electronic and pileup noise, inside a cone of size $\Delta R < 0.2$ around the muon direction, divided by the muon p_T . Muons are required to have a relative calorimetric isolation less than 0.3 (0.15 in the case of stand-alone muons). For both the track- and calorimeter-based isolations any contributions arising from other leptons of the quadruplet are subtracted.

As discussed in Sec. IV C, a search is performed for FSR photons arising from any of the lepton candidates in the final quadruplet, and at most one FSR photon candidate is added to the 4ℓ system. The FSR correction is applied only to the leading dilepton, and priority is given to collinear photons. The correction is applied if $66 < m_{\mu\mu} < 89$ GeV and $m_{\mu\gamma} < 100$ GeV. If the collinear-photon search fails then the noncollinear FSR photon with the highest E_T is added, provided it satisfies the following requirements: $m_{\ell\ell} < 81$ GeV and $m_{\ell\ell\gamma} < 100$ GeV. The expected fraction of collinear (noncollinear) corrected events is 4% (1%).

For the 7 TeV data, the combined signal reconstruction and selection efficiency for $m_H = 125$ GeV is 39% for the 4μ channel, 25% for the $2e2\mu/2\mu2e$ channels and 17% for

the $4e$ channel. The improvements in the electron reconstruction and identification for the 8 TeV data lead to increases in these efficiencies by 10%–15% for the channels with electrons, bringing their efficiencies to 27% for the $2e2\mu/2\mu2e$ channels and 20% for the $4e$ channel.

After the FSR correction, the lepton four-momenta of the leading dilepton are recomputed by means of a Z -mass-constrained kinematic fit. The fit uses a Breit-Wigner Z line shape and a single Gaussian to model the lepton momentum response function with the Gaussian σ set to the expected resolution for each lepton. The Z -mass constraint improves the $m_{4\ell}$ resolution by about 15%. More complex momentum response functions were compared to the single Gaussian and found to have only minimal improvement for the $m_{4\ell}$ resolution.

Events satisfying the above criteria are considered candidate signal events for the inclusive analysis, defining a signal region independent of the value of $m_{4\ell}$.

B. Event categorization

To measure the rates for the ggF, VBF, and VH production mechanisms, discussed in Sec. III, each $H \rightarrow 4\ell$ candidate selected by the criteria described above is assigned to one of four categories (VBF enriched, VH-hadronic enriched, VH-leptonic enriched, or ggF enriched), depending on other event characteristics. A schematic view of the event categorization is shown in Fig. 2.

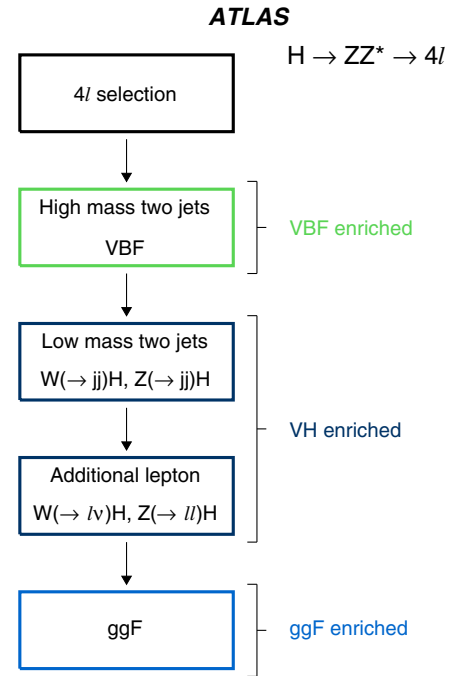


FIG. 2 (color online). Schematic view of the event categorization. Events are required to pass the four-lepton selection, and then they are assigned to one of four categories which are tested sequentially: VBF enriched, VH-hadronic enriched, VH-leptonic enriched, or ggF enriched.

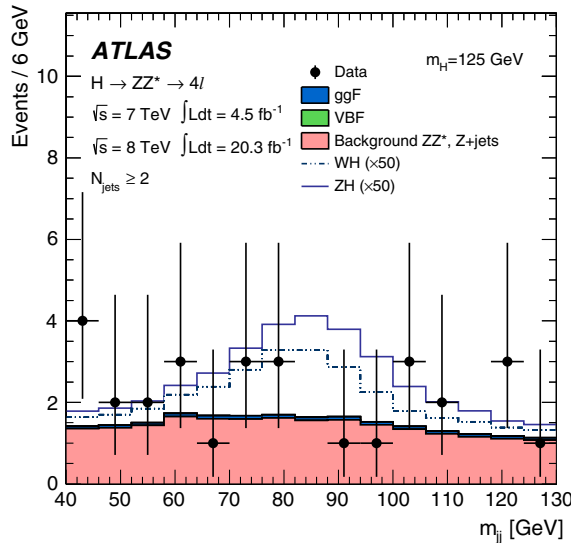


FIG. 3 (color online). Distributions of the dijet invariant mass for the events with at least two jets for the data (filled circles), the expected signal (solid and dot-dot-dashed histograms) and the backgrounds (filled histograms). The WH and ZH hadronic signals are scaled by a factor 50 and the ZH distribution is added on top of the WH distribution.

The VBF enriched category is defined by events with two high- p_T jets. The kinematic requirements for jets are $p_T > 25(30)$ GeV for $|\eta| < 2.5 (2.5 < |\eta| < 4.5)$. If more than two jets fulfill these requirements, the two highest- p_T jets are selected as VBF jets. The event is assigned to the VBF enriched category if the invariant mass of the dijet system, m_{jj} , is greater than 130 GeV, leading to a signal efficiency of approximately 55%. This category has a considerable contamination from ggF events, with 54% of the expected events in this category arising from production via gluon fusion.

Events that do not satisfy the VBF enriched criteria are considered for the VH-hadronic enriched category. The

same jet-related requirements are applied but with $40 < m_{jj} < 130$ GeV, as presented in Fig. 3. Moreover, the candidate has to fulfill a requirement on the output weight of a specific multivariate discriminant, presented in Sec. VII B. The signal efficiency for requiring two jets is 48% for VH and applying the multivariate discriminant brings the overall signal efficiency to 25%.

Events failing to satisfy the above criteria are next considered for the VH-leptonic enriched category. Events are assigned to this category if there is an extra lepton (e or μ), in addition to the four leptons forming the Higgs boson candidate, with $p_T > 8$ GeV and satisfying the same lepton requirements. The signal efficiency for the extra vector boson for the VH-leptonic enriched category is around 90% (100%) for the W (Z), where the Z has two leptons which can pass the extra lepton selection.

Finally, events that are not assigned to any of the above categories are associated with the ggF enriched category. Table II shows the expected yields for Higgs boson production and ZZ^* background events in each category from each of the production mechanisms, for $m_H = 125$ GeV and 4.5 fb^{-1} at $\sqrt{s} = 7 \text{ TeV}$ and 20.3 fb^{-1} at $\sqrt{s} = 8 \text{ TeV}$.

VI. Background Estimation

The rate of the ZZ^* background is estimated using simulation normalized to the SM cross section as described in Sec. III, while the rate and composition of the reducible $\ell\ell + \text{jets}$ and $t\bar{t}$ background processes are evaluated with data-driven methods. The composition of the reducible backgrounds depends on the flavor of the subleading dilepton pair, and different approaches are taken for the $\ell\ell + \mu\mu$ and the $\ell\ell + ee$ final states. These two cases are discussed in Secs. VIA and VIB, respectively, and the yields for all reducible backgrounds in the signal region are summarized in Tables V and VII. Finally, the small contribution from the WZ reducible background is

TABLE II. The expected number of events in each category (ggF enriched, VBF enriched, VH-hadronic enriched and VH-leptonic enriched), after all analysis criteria are applied, for each signal production mechanism ($ggF/b\bar{b}H/t\bar{t}H$, VBF, VH) at $m_H = 125$ GeV, for 4.5 fb^{-1} at $\sqrt{s} = 7 \text{ TeV}$ and 20.3 fb^{-1} at $\sqrt{s} = 8 \text{ TeV}$. The requirement $m_{4\ell} > 110$ GeV is applied.

Category	$gg \rightarrow H, q\bar{q}/gg \rightarrow b\bar{b}H/t\bar{t}H$	$qq' \rightarrow Hqq'$	$q\bar{q} \rightarrow W/ZH$
$\sqrt{s} = 7 \text{ TeV}$			
ggF enriched	2.06 ± 0.25	0.114 ± 0.005	0.067 ± 0.003
VBF enriched	0.13 ± 0.04	0.137 ± 0.009	0.015 ± 0.001
VH-hadronic enriched	0.053 ± 0.018	0.007 ± 0.001	0.038 ± 0.002
VH-leptonic enriched	0.005 ± 0.001	0.0007 ± 0.0001	0.023 ± 0.002
$\sqrt{s} = 8 \text{ TeV}$			
ggF enriched	12.0 ± 1.4	0.52 ± 0.02	0.37 ± 0.02
VBF enriched	1.2 ± 0.4	0.69 ± 0.05	0.10 ± 0.01
VH-hadronic enriched	0.41 ± 0.14	0.030 ± 0.004	0.21 ± 0.01
VH-leptonic enriched	0.021 ± 0.003	0.0009 ± 0.0002	0.13 ± 0.01

estimated from simulation. The background estimation follows the methods previously described in Refs. [4,92] with several improvements and additional cross-checks.

A. $\ell\ell + \mu\mu$ background

The $\ell\ell + \mu\mu$ reducible background arises from $Z +$ jets and $t\bar{t}$ processes, where the $Z +$ jets contribution has a $Zb\bar{b}$ heavy-flavor quark component in which the heavy-flavor quarks decay semileptonically, and a component arising from $Z +$ light-flavor jets with subsequent π/K in-flight decays. The number of background events from $Z +$ jets and $t\bar{t}$ production is estimated from an unbinned maximum likelihood fit, performed simultaneously to four orthogonal control regions, each of them providing information on one or more of the background components. The fit results are expressed in terms of yields in a reference control region, defined by applying the analysis event selection except for the isolation and impact parameter requirements to the subleading dilepton pair. The reference control region is also used for the validation of the estimates. Finally, the background estimates in the reference control region are extrapolated to the signal region.

The control regions used in the maximum likelihood fit are designed to minimize contamination from the Higgs boson signal and the ZZ^* background. The four control regions are

- (a) *Inverted requirement on impact parameter significance.* Candidates are selected following the analysis event selection, but (1) without applying the isolation requirement to the muons of the subleading dilepton and (2) requiring that at least one of the two muons fails the impact parameter significance requirement. As a result, this control region is enriched in $Zb\bar{b}$ and $t\bar{t}$ events.
- (b) *Inverted requirement on isolation.* Candidates are selected following the analysis event selection, but requiring that at least one of the muons of the subleading dilepton fails the isolation requirement. As a result, this control region is enriched in $Z +$ light-flavor-jet events (π/K in-flight decays) and $t\bar{t}$ events.
- (c) *$e\mu$ leading dilepton ($e\mu + \mu\mu$).* Candidates are selected following the analysis event selection, but requiring the leading dilepton to be an electron-muon pair. Moreover, the isolation and impact parameter

requirements are not applied to the muons of the subleading dilepton, which are also allowed to have the same or opposite charge sign. Events containing a Z -boson candidate decaying into e^+e^- or $\mu^+\mu^-$ pairs are removed with a requirement on the mass. This control region is dominated by $t\bar{t}$ events.

- (d) *Same-sign subleading dilepton.* The analysis event selection is applied, but for the subleading dilepton neither isolation nor impact parameter significance requirements are applied and the leptons are required to have the same charge sign (SS). This same-sign control region is not dominated by a specific background; all the reducible backgrounds have a significant contribution.

The expected composition for each control region is shown in Table III. The uncertainties on the relative yields between the control regions and the reference control region are introduced in the maximum likelihood fit as nuisance parameters. The residual contribution from ZZ^* and the contribution from WZ production, where—contrary to the $Z +$ jets and $t\bar{t}$ backgrounds—only one of the leptons in the subleading dilepton is expected to be a nonisolated backgroundlike muon, are estimated for each control region from simulation.

In all the control regions, the observable is the mass of the leading dilepton, m_{12} , which peaks at the Z mass for the resonant ($Z +$ jets) component and has a broad distribution for the nonresonant ($t\bar{t}$) component. For the $t\bar{t}$ component the m_{12} distribution is modeled by a second-order Chebyshev polynomial, while for the $Z +$ jets component it is modeled using a convolution of a Breit-Wigner distribution with a Crystal Ball function. The shape parameters are derived from simulation. In the combined fit, the shape parameters are constrained to be the same in each of the control regions, and are allowed to fluctuate within the uncertainties obtained from simulation. The results of the combined fit in the four control regions are shown in Fig. 4, along with the individual background components, while the event yields in the reference control region are summarized in Table IV. As a validation of the fit method, the maximum likelihood fit is applied to the individual control regions yielding estimates compatible to those of the combined fit; these are also summarized in Table IV.

The estimated yields in the reference control region are extrapolated to the signal region by multiplying each

TABLE III. Expected contribution of the $\ell\ell + \mu\mu$ background sources in each of the control regions.

Background	Control region			
	Inverted d_0	Inverted isolation	$e\mu + \mu\mu$	Same-sign
$Zb\bar{b}$	$32.8 \pm 0.5\%$	$26.5 \pm 1.2\%$	$0.3 \pm 1.2\%$	$30.6 \pm 0.7\%$
$Z +$ light-flavor jets	$9.2 \pm 1.3\%$	$39.3 \pm 2.6\%$	$0.0 \pm 0.8\%$	$16.9 \pm 1.6\%$
$t\bar{t}$	$58.0 \pm 0.9\%$	$34.2 \pm 1.6\%$	$99.7 \pm 1.0\%$	$52.5 \pm 1.1\%$

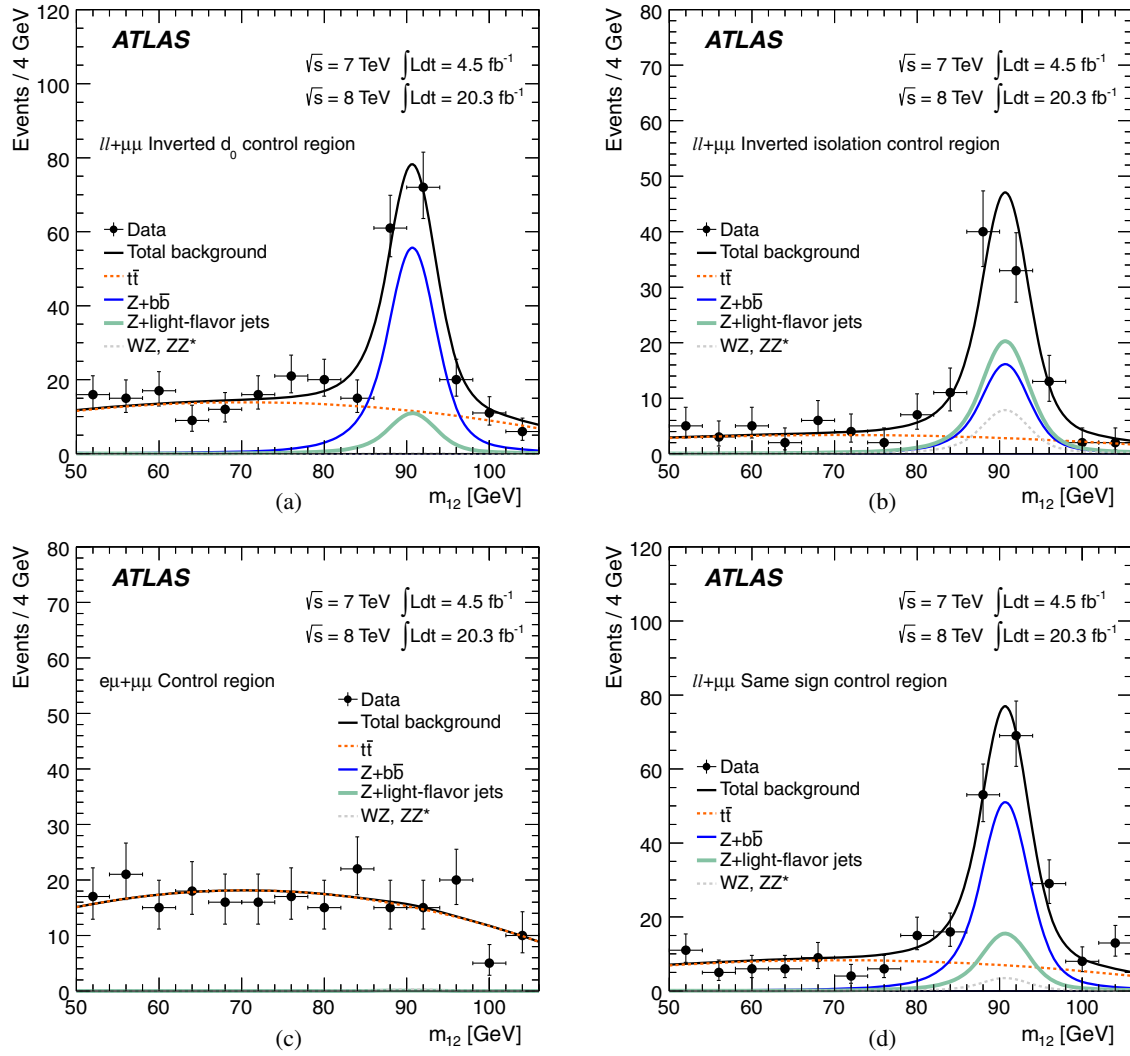


FIG. 4 (color online). The observed m_{12} distributions (filled circles) and the results of the maximum likelihood fit are presented for the four control regions: (a) inverted requirement on impact parameter significance, (b) inverted requirement on isolation, (c) $e\mu$ leading dilepton, where the backgrounds besides $t\bar{t}$ are small and not visible, and (d) same-sign subleading dilepton. The fit results are shown for the total background (black line) as well as the individual components: $Z +$ jets decomposed into $Z + b\bar{b}$ (blue line) and $Z +$ light-flavor jets (green line), $t\bar{t}$ (dashed red line), and the combined WZ and ZZ (dashed gray line), where the WZ and ZZ contributions are estimated from simulation.

background component by the probability of satisfying the isolation and impact parameter significance requirements, estimated from the relevant simulated sample. The systematic uncertainty in these transfer factors, stemming mostly from the size of the simulated sample, is 6% for $Zb\bar{b}$, 60% for $Z +$ light-flavor jets and 16% for $t\bar{t}$. Furthermore, these simulation-based efficiencies are validated with data using muons accompanying $Z \rightarrow \ell\ell$ candidates, where the leptons composing the Z boson candidate are required to satisfy isolation and impact parameter criteria. Events with four leptons, or with an opposite-sign dimuon with mass less than 5 GeV, are excluded. Based on the data/simulation agreement of the efficiencies in this control region an additional systematic uncertainty of 1.6% is added. Figure 5 shows the relative difference between the ID

and MS p_T measurements for combined muons for a subset of the $Z + X$ control region where the X represents a single combined muon. The contribution from π/K in-flight decays is clearly visible and well described by the simulation.

The reducible background estimates in the signal region are given in Table V, separately for the $\sqrt{s} = 7$ TeV and 8 TeV data. The uncertainties are separated into statistical and systematic contributions, where in the latter the transfer factor uncertainty and the fit systematic uncertainties are included.

B. $\ell\ell + ee$ background

The background for subleading electron pairs arises from jets misidentified as electrons. The background is classified

TABLE IV. Data-driven $\ell\ell + \mu\mu$ background estimates for the $\sqrt{s} = 7$ TeV and $\sqrt{s} = 8$ TeV data, expressed as yields in the reference control region, for the combined fit and fits to the individual control regions. In the individual control regions only the total $Z +$ jets contribution can be determined, while the $e\mu + \mu\mu$ control region is only sensitive to the $t\bar{t}$ background. The statistical uncertainties are also shown.

Reducible background yields for 4μ and $2e2\mu$ in reference control region				
Control region	$Zb\bar{b}$	$Z +$ light-flavor jets	Total $Z +$ jets	$t\bar{t}$
Combined fit	159 ± 20	49 ± 10	208 ± 22	210 ± 12
Inverted impact parameter			206 ± 18	208 ± 23
Inverted isolation			210 ± 21	201 ± 24
$e\mu + \mu\mu$			—	201 ± 12
Same-sign dilepton			198 ± 20	196 ± 22

into three distinct sources: light-flavor jets (f), photon conversions (γ) and heavy-flavor semileptonic decays (q). These sources are identified exactly in simulated background events. In addition, corresponding data control regions are defined which are enriched in events associated with each of these sources, thus allowing data-driven classification of reconstructed events into matching categories. For the background estimation, two types of control regions are defined:

- (i) the first, denoted as $3\ell + X$, in which the identification requirements for the lower- p_T electron of the subleading pair are relaxed;

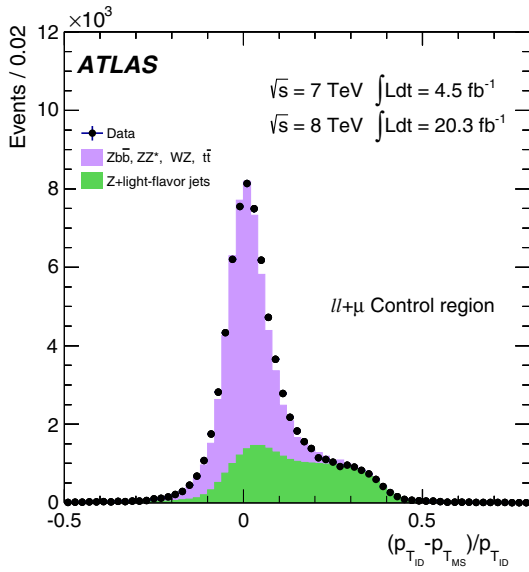


FIG. 5 (color online). The distribution of the difference between the transverse momentum measured in the ID and in the MS normalized to the ID measurement, $(p_{T_{ID}} - p_{T_{MS}})/p_{T_{ID}}$, for combined muons accompanying a $Z \rightarrow \ell\ell$ candidate. The data (filled circles) are compared to the background simulation (filled histograms) which has the $Z +$ light-flavor background shown separately to distinguish the contribution from π/K in-flight decays. The additional muon is selected to be a combined muon with $p_T > 6$ GeV, which fulfills the ΔR requirement for the lepton separation of the analysis and in the case of $Z(\rightarrow \mu^+\mu^-) + \mu$ final state, the opposite sign pairs are required to have $m_{\mu^+\mu^-} > 5$ GeV to remove J/ψ decays.

- (ii) the second, denoted as $\ell\ell + XX$, which comes in two variants: one in which the identification requirements for both electrons of the subleading pair are relaxed, and another in which an inverted selection is applied to the subleading pair.

In both cases, the leading pair satisfies the complete event selection. The final background estimate is obtained from the $3\ell + X$ region, while the estimates from the $\ell\ell + XX$ region are used as cross-checks.

The efficiencies needed to extrapolate the different background sources from the control regions into the signal region are obtained separately for each of the f , γ , q background sources, in p_T and η bins, from simulation. These simulation-based efficiencies are corrected to correspond to the efficiency measured in data using a third type of control region, denoted as $Z + X$, enhanced for each X component. The $Z + X$ control region has a leading lepton pair, compatible with the decay of a Z boson, passing the full event selection and an additional object (X) that satisfies the relaxed identification for the specific control region to be extrapolated. The $Z + X$ data sample is significantly larger than the background control data samples. For all of the methods, the extrapolation from the background control region, $3\ell + X$ or $\ell\ell + XX$, to the signal region cannot be done directly with the efficiencies from the $Z + X$ data control region due to differences in the fractions of f , γ , q for the X of the two control regions. In the following, the q contribution in the simulation is increased by a factor of 1.4 to match the data.

1. Background estimation from $3\ell + X$

This method uses the $3\ell + X$ data control region with one loosely identified lepton for normalization. The control region is then fit using templates derived from simulation to determine the composition in terms of the three background sources f , γ , q , and these components are extrapolated individually to the signal region using the efficiency from the $Z + X$ control region.

The background estimation from the $3\ell + X$ region uses data that has quadruplets built as for the full analysis, with the exception that the full selection is applied to only the three highest- p_T leptons. Relaxed requirements are applied

TABLE V. Estimates for the $\ell\ell + \mu\mu$ background in the signal region for the full $m_{4\ell}$ mass range for the $\sqrt{s} = 7$ TeV and $\sqrt{s} = 8$ TeV data. The $Z + \text{jets}$ and $t\bar{t}$ background estimates are data-driven and the WZ contribution is from simulation. The decomposition of the $Z + \text{jets}$ background in terms of the $Zb\bar{b}$ and the $Z + \text{light-flavor-jets}$ contributions is also provided.

Background	4μ	$2e2\mu$
$\sqrt{s} = 7$ TeV		
$Z + \text{jets}$	$0.42 \pm 0.21(\text{stat}) \pm 0.08(\text{syst})$	$0.29 \pm 0.14(\text{stat}) \pm 0.05(\text{syst})$
$t\bar{t}$	$0.081 \pm 0.016(\text{stat}) \pm 0.021(\text{syst})$	$0.056 \pm 0.011(\text{stat}) \pm 0.015(\text{syst})$
WZ expectation	0.08 ± 0.05	0.19 ± 0.10
$Z + \text{jets}$ decomposition		
$Zb\bar{b}$	$0.36 \pm 0.19(\text{stat}) \pm 0.07(\text{syst})$	$0.25 \pm 0.13(\text{stat}) \pm 0.05(\text{syst})$
$Z + \text{light-flavor jets}$	$0.06 \pm 0.08(\text{stat}) \pm 0.04(\text{syst})$	$0.04 \pm 0.06(\text{stat}) \pm 0.02(\text{syst})$
$\sqrt{s} = 8$ TeV		
$Z + \text{jets}$	$3.11 \pm 0.46(\text{stat}) \pm 0.43(\text{syst})$	$2.58 \pm 0.39(\text{stat}) \pm 0.43(\text{syst})$
$t\bar{t}$	$0.51 \pm 0.03(\text{stat}) \pm 0.09(\text{syst})$	$0.48 \pm 0.03(\text{stat}) \pm 0.08(\text{syst})$
WZ expectation	0.42 ± 0.07	0.44 ± 0.06
$Z + \text{jets}$ decomposition		
$Zb\bar{b}$	$2.30 \pm 0.26(\text{stat}) \pm 0.14(\text{syst})$	$2.01 \pm 0.23(\text{stat}) \pm 0.13(\text{syst})$
$Z + \text{light-flavor jets}$	$0.81 \pm 0.38(\text{stat}) \pm 0.41(\text{syst})$	$0.57 \pm 0.31(\text{stat}) \pm 0.41(\text{syst})$

to the lowest- p_T electron: only a track with a minimum number of silicon hits which matches a cluster is required and the electron identification and isolation/impact parameter significance selection criteria are not applied. In addition, the subleading electron pair is required to have the same sign for both charges (SS) to minimize the contribution from the ZZ^* background. A residual ZZ^* component with a magnitude of 5% of the background estimate survives the SS selection, and is subtracted to get the final estimate.

By requiring only a single electron with relaxed selection, the composition of the control region is simplified when compared with the other $\ell\ell + XX$ control regions, and the yields of the different background components can be extracted with a two-dimensional fit. Two variables, the number of hits in the innermost layer of the pixel detector ($n_{\text{hits}}^{\text{B-layer}}$) and the ratio of the number of high-threshold to low-threshold TRT hits (r_{TRT}),³ allow the separation of the f, γ and q components, since most photons convert after the innermost pixel layer, and hadrons faking electrons have a lower r_{TRT} compared to conversions and heavy-flavor electrons. Templates for the fit are taken from the $Z + X$ simulation after applying corrections from data.

The results of the fit are shown in Fig. 6, for the $2\mu 2e$ and $4e$ channels combined. The *sPlot* method [93] is used to unfold the contributions from the different background sources as a function of electron p_T . The background

estimates for the f, γ and q components in the control region, averaged over the $2\mu 2e$ and $4e$ channels, are summarized in Table VI.

To extrapolate the f, γ and q components from the $3\ell + X$ control region to the signal region, the efficiency for the different components to satisfy all selection criteria is obtained from the $Z + X$ simulation. As previously mentioned, the simulation efficiency for each component is corrected by comparing with data using the $Z + X$ control region with an adjusted selection to enrich it for each specific component. For the f component, the simulation efficiency is corrected by a factor between 1.6 and 2.5, rising with increasing p_T . The simulation is found to model well the efficiency of the γ component, to within approximately 10%. For the q component, the efficiency is found to be modeled well by simulation, but there is an additional correction, obtained from simulation, to estimate the number of background opposite-sign (OS) events from the number of SS events, which is $\text{OS}/\text{SS} \approx 1.7$. The systematic uncertainty is dominated by these simulation efficiency corrections, corresponding to 30%, 20%, 25% uncertainties for f, γ, q , respectively. The extrapolation efficiency and signal yields are also given in Table VI. After removing the residual ZZ^* background ($\approx 5\%$), the final results for the $2\mu 2e$ and $4e$ reducible backgrounds are given in Table VII.

2. Background estimation from the $\ell\ell + XX$ region using the transfer-factor method

The transfer-factor method starts from the $\ell\ell + XX$ control region in data with two leptons with inverted

³A large number of hits above a high signal pulse-height threshold is an indication of the presence of transition radiation, which is more probable for electrons than for pions.

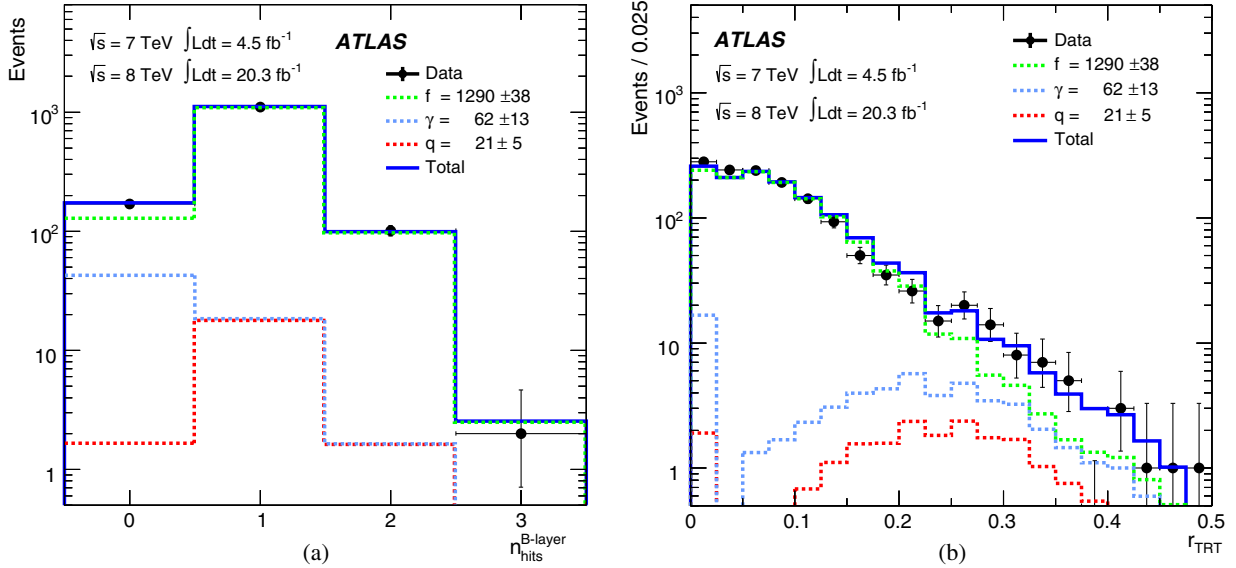


FIG. 6 (color online). The results of a simultaneous fit to (a) $n_{\text{B-layer}}^{\text{hits}}$, the number of hits in the innermost pixel layer, and (b) r_{TRT} , the ratio of the number of high-threshold to low-threshold TRT hits, for the background components in the $3\ell + X$ control region. The fit is performed separately for the $2\mu 2e$ and $4e$ channels and summed together in the present plots. The data are represented by the filled circles. The sources of background electrons are denoted as light-flavor jets faking an electron (f , green dashed histogram), photon conversions (γ , blue dashed histogram) and electrons from heavy-flavor quark semileptonic decays (q , red dashed histogram). The total background is given by the solid blue histogram.

selection requirements. Using the predicted sample composition from simulation, two approaches are taken to obtain transfer factors: one using the $Z + X$ simulation corrected by data, and the other using the $Z + X$ data control region that is enriched to obtain a q component matching that of the $\ell\ell + XX$ control region.

The $\ell\ell + XX$ data control region has relaxed electron likelihood identification on the X pair and requires each X to fail one selection among the full electron identification, isolation and impact parameter significance selections, leading to a sample of around 700 events for each of the $2\mu + XX$ and $2e + XX$ channels. The inverted selection

removes most of the ZZ^* background from the control region as well as the Higgs signal. The main challenge is to correctly estimate the extrapolation efficiency, or transfer factor, from the $\ell\ell + XX$ control region to the signal region using the $Z + X$ sample, since the background composition of f, γ and q is different for the $Z + X$ and $\ell\ell + XX$ control regions and each of their extrapolation efficiencies is significantly different.

In order to aid in the understanding of the control region composition and to improve the uncertainty on the estimate of the extrapolation to the signal region, each X is assigned to one of two reconstruction categories: electron-like (E) or

TABLE VI. The fit results for the $3\ell + X$ control region, the extrapolation factors and the signal region yields for the reducible $\ell\ell + ee$ background. The second column gives the fit yield of each component in the $3\ell + X$ control region. The corresponding extrapolation efficiency and signal region yield are in the next two columns. The background values represent the sum of the $2\mu 2e$ and $4e$ channels. The uncertainties are the combination of the statistical and systematic uncertainties.

$2\mu 2e$ and $4e$ Type	Fit yield in control region	Extrapolation factor	Yield in signal region
f	391 ± 29	$\sqrt{s} = 7 \text{ TeV}$ data	3.9 ± 0.9
		0.010 ± 0.001	2.0 ± 1.0
		0.10 ± 0.02	0.51 ± 0.15
γ	19 ± 9	$\sqrt{s} = 8 \text{ TeV}$ data	3.1 ± 1.0
		0.024 ± 0.004	1.1 ± 0.6
		0.10 ± 0.02	1.8 ± 0.5
q	5.1 ± 1.0		
f	894 ± 44		
γ	48 ± 15		
q	18.3 ± 3.6		

TABLE VII. Summary of the $\ell\ell + ee$ data-driven background estimates for the $\sqrt{s} = 7$ TeV and $\sqrt{s} = 8$ TeV data for the full $m_{4\ell}$ mass range. OS (SS) stands for opposite-sign (same-sign) lepton pairs. The “ \dagger ” symbol indicates the estimates used for the background normalization; the other estimates are used as cross-checks. The first uncertainty is statistical, while the second is systematic. The SS data full analysis is limited to the region with $m_{4\ell}$ below 160 GeV to avoid a ZZ contribution; this region contains 70% of the expected background.

Method	$\sqrt{s} = 7$ TeV data	$\sqrt{s} = 8$ TeV data
$2\mu 2e$		
$3\ell + X^\dagger$	$2.9 \pm 0.5 \pm 0.5$	$2.9 \pm 0.3 \pm 0.6$
$\ell\ell + XX$ transfer factor	$2.2 \pm 0.3 \pm 1.1$	$2.5 \pm 0.1 \pm 0.9$
$\ell\ell + XX$ transfer factor b -enriched	$2.8 \pm 0.5 \pm 0.8$	$3.2 \pm 0.2 \pm 0.9$
$\ell\ell + XX$ reco-truth	$2.8 \pm 0.4 \pm 1.0$	$2.9 \pm 0.3 \pm 0.3$
$2\mu 2e$ SS data full analysis	1	2
$4e$		
$3\ell + X^\dagger$	$3.3 \pm 0.5 \pm 0.5$	$2.9 \pm 0.3 \pm 0.5$
$\ell\ell + XX$ transfer factor	$2.0 \pm 0.3 \pm 0.9$	$2.4 \pm 0.1 \pm 0.9$
$\ell\ell + XX$ transfer factor b -enriched	$3.4 \pm 0.9 \pm 0.8$	$2.9 \pm 0.2 \pm 0.8$
$\ell\ell + XX$ reco-truth	$2.6 \pm 0.4 \pm 0.9$	$2.8 \pm 0.3 \pm 0.3$
$4e$ SS data full analysis	2	2

fake-like (F), for both data and simulation. For the E category, a selection is applied to enhance the electron content, and the remaining X 's fall into the F category. For the $\ell\ell + XX$ control region, the composition of X in terms of the background source is balanced between fakes (f) and electrons (γ, q) for the E category corresponding to component fractions of 50% f , 20% γ , and 30% q , and is dominated by fakes for the F category with 92% f , 5% γ and 3% q .

The two approaches taken to estimate the background from the $\ell\ell + XX$ data control region differ in the way they estimate the extrapolation to the signal region with $Z + X$ events. Both approaches separate XX into the four reconstruction categories: EE, EF, FE and FF. The first approach uses the $Z + X$ simulation to determine the transfer factors for X in bins of p_T and η , where the extrapolation efficiency of each background component of the $\ell\ell + XX$ simulation is combined according to the composition seen in the $\ell\ell + XX$ simulation. In addition, the simulation extrapolation efficiency is corrected to agree with data as previously described in Sec. VIB 1. For the background estimate, the transfer factors are applied to the $\ell\ell + XX$ data control region, accounting for the inverted selection. The result is corrected by subtracting a small residual ZZ^* contribution, and including a WZ contribution that is removed by the inverted selection on the XX ; both are estimated with simulation. The background estimate with the transfer-factor method is given in Table VII.

The second approach differs in the manner in which the background composition of the $Z + X$ control region is brought into agreement with the $\ell\ell + XX$ control region. The most important difference lies in the heavy-flavor component fraction, which is three times larger in the $\ell\ell + XX$ control region and has a significantly larger transfer factor than either the f or γ backgrounds. This approach modifies the composition of the $Z + X$ data control region

by requiring a b -jet in each event. By tuning the selection of a multivariate b -tagger [94], the q and f composition of the $Z + X$ control region can be brought into agreement with that of the $\ell\ell + XX$ control region to the level of 5%–10%, as seen with simulation. The transfer factors are extracted from the $Z + X$ data control region and applied in bins of p_T and η as for the other approach, and the systematic uncertainty is estimated in part by varying the operating point used for the multivariate b -tagger. Finally, the WZ contribution is accounted for with simulation, as previously. The background estimate from the transfer factors based on b -enriched samples is given in Table VII.

3. Reco-truth unfolding method

A third method uses the $\ell\ell + XX$ data control region; however, the two subleading electrons have only the electron identification relaxed and do not have an inverted selection applied as for the transfer-factor method. This control region thus contains all backgrounds, including the ZZ^* background, and the $H \rightarrow ZZ^* \rightarrow 4\ell$ signal. The extrapolation to the signal region is performed with the $Z + X$ simulation. This method was used as the baseline for previous publications [4,6], but is now superseded by the $3\ell + X$ method, which provides the smallest uncertainties of the data-driven methods. Using the simulation, each of the paired reconstruction categories (EE, EF, FE and FF) of the $\ell\ell + XX$ sample is decomposed into its background origin components (ee , ff , $\gamma\gamma$, qq and the 12 cross combinations), where the e background category is introduced to contain the isolated electrons from ZZ^* and $H \rightarrow ZZ^* \rightarrow 4\ell$. This 4×16 composition table is summed with efficiency weights, in bins of p_T and η , obtained from the $Z + X$ simulation, which is corrected from comparison with data as previously mentioned. To remove the ZZ^* and $H \rightarrow ZZ^* \rightarrow 4\ell$ contributions from this estimate, the

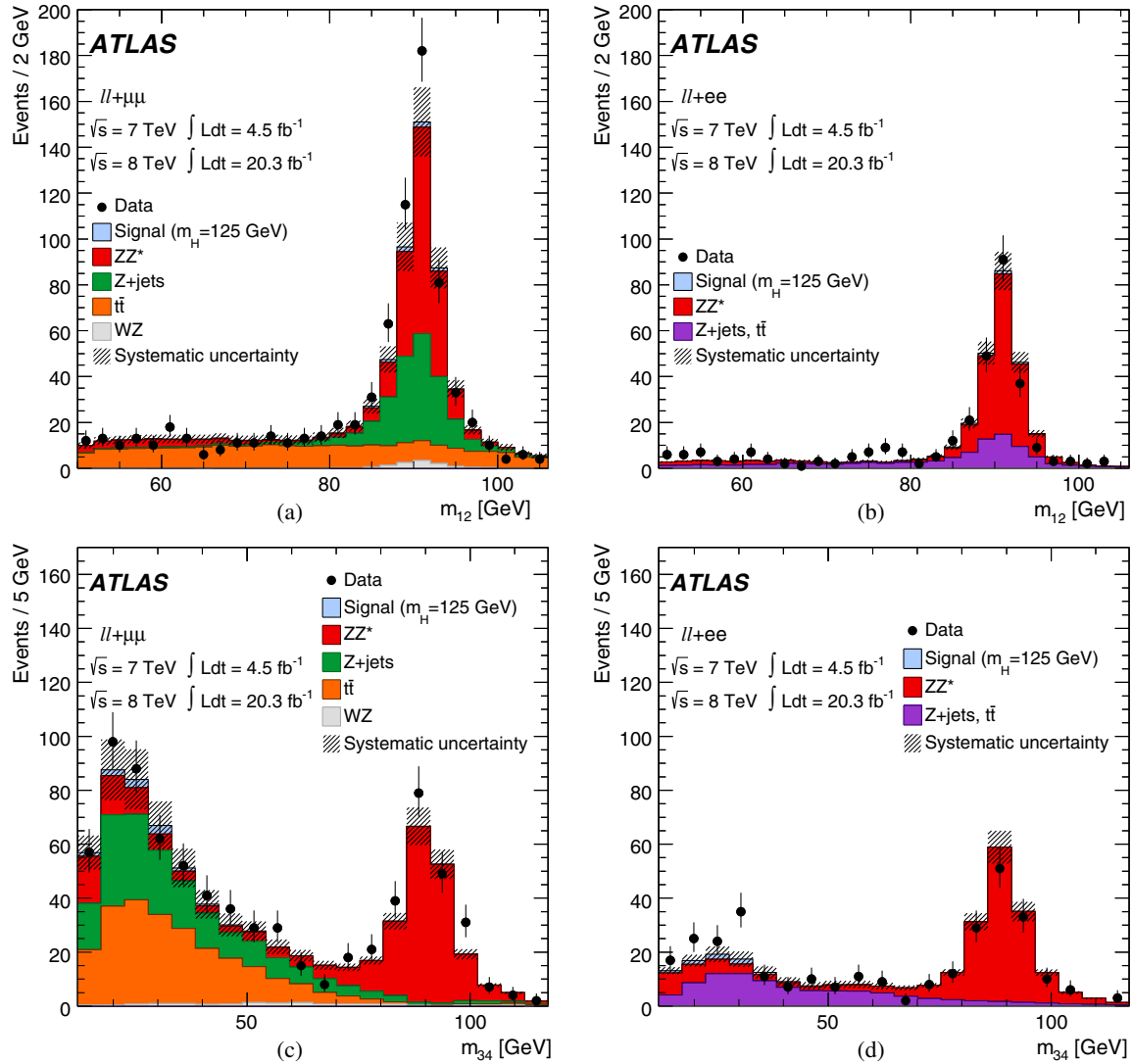


FIG. 7 (color online). Invariant mass distributions of the lepton pairs in the control sample defined by a Z boson candidate and an additional same-flavor lepton pair, including all signal and background contributions, for the $\sqrt{s} = 7$ TeV and $\sqrt{s} = 8$ TeV data sets. The sample is divided according to the flavor of the additional lepton pair. In (a) and (c) the m_{12} and m_{34} distributions are presented for $\ell\ell + \mu^+\mu^-$ events, where $\ell\ell$ is $\mu^+\mu^-$ or e^+e^- . In (b) and (d) the m_{12} and m_{34} distributions are presented for $\ell\ell + e^+e^-$ events. The data are shown as filled circles and the different backgrounds as filled histograms with the total background systematic uncertainty represented by the hatched areas. The kinematic selection of the analysis is applied. Isolation and impact parameter significance requirements are applied to the first lepton pair only. The simulation is normalized to the data-driven background estimates.

background origin category ee is removed from the sum, and an estimated residual of 1.2 ± 0.4 ZZ^* events is subtracted to obtain the final result, which is also given in Table VII.

4. Summary of reducible background estimates for $\ell\ell + ee$

The summary of the reducible backgrounds for the $\ell\ell + ee$ final states is given for the full mass region in Table VII. In addition to the previously discussed methods, the results are presented for the full analysis applied to $\ell\ell + ee$ events in data where the subleading ee pair is required to have the

same-sign charge, and $m_{4\ell}$ is required to be below 160 GeV to avoid a ZZ contribution; the region with $m_{4\ell} < 160$ GeV contains 70% of the expected reducible backgrounds. Although limited in statistical precision, this agrees well with the other estimates.

C. Shape of the reducible background contributions

The $m_{4\ell}$ distributions of the reducible backgrounds are required for the normalization and shape of these backgrounds in the mass fit region, discussed below. The shape of the distribution for the $\ell\ell + \mu\mu$ background is taken from simulation and the uncertainty comes from varying

TABLE VIII. Summary of the background estimates for the data recorded at $\sqrt{s} = 7$ TeV and $\sqrt{s} = 8$ TeV for the full $m_{4\ell}$ mass range. The quoted uncertainties include the combined statistical and systematic components.

Channel	ggF enriched	VBF enriched	VH-hadronic enriched	VH-leptonic enriched
$\sqrt{s} = 7$ TeV				
$\ell\ell + \mu\mu$	0.98 ± 0.32	0.12 ± 0.08	0.04 ± 0.02	0.004 ± 0.004
$\ell\ell + ee$	5.5 ± 1.2	0.51 ± 0.6	0.20 ± 0.16	0.06 ± 0.11
$\sqrt{s} = 8$ TeV				
$\ell\ell + \mu\mu$	6.7 ± 1.4	0.6 ± 0.6	0.21 ± 0.13	0.003 ± 0.003
$\ell\ell + ee$	5.1 ± 1.4	0.5 ± 0.6	0.19 ± 0.15	0.06 ± 0.11

the track isolation and impact parameter significance selections. The corresponding distribution for the $\ell\ell + ee$ background comes from the $3\ell + X$ sample, after reweighting with the transfer factor to match the kinematics of the signal region. The uncertainty in the $\ell\ell + ee$ background shape is taken as the difference between the shapes obtained from the control regions of the two other methods: transfer factor and reco-truth. The estimates in the $120 < m_{4\ell} < 130$ GeV mass window are provided in Table XI. Figure 7 presents the m_{12} and m_{34} distributions for the $\ell\ell + \mu\mu$ and $\ell\ell + ee$ control regions where the full selection has been applied except for subleading lepton impact parameter significance and isolation requirements, which are not applied. Good agreement is seen between the data and the sum of the various background estimates. The shape of the background in the $m_{4\ell}$ distribution extrapolated to the signal region can be seen in Fig. 13.

D. Background for categories

For the reducible background, the fraction of background in each category is evaluated using simulation. Applying these fractions to the background estimates from Tables V and VII gives the reducible background estimates per category shown in Table VIII. The systematic uncertainties include the differences observed between the fractions obtained from simulation and those from the reducible background data control regions. The expected ZZ^* background evaluated from simulation for each category is given in Table XII. To obtain the reducible background in the signal region, the shapes of the $m_{4\ell}$ distributions for the reducible backgrounds discussed in Sec. VIC are used.

VII. MULTIVARIATE DISCRIMINANTS

The analysis sensitivity is improved by employing three multivariate discriminants to distinguish between the different classes of four-lepton events: one to separate the Higgs boson signal from the ZZ^* background in the inclusive analysis, and two to separate the VBF- and VH-produced Higgs boson signal from the ggF-produced Higgs boson signal in the VBF enriched and VH-hadronic enriched categories. These discriminants are based on boosted decision trees (BDT) [95].

A. BDT for ZZ^* background rejection

The differences in the kinematics of the $H \rightarrow ZZ^* \rightarrow 4\ell$ decay and the ZZ^* background are incorporated into a BDT discriminant (BDT_{ZZ^*}). The training is done using fully simulated $H \rightarrow ZZ^* \rightarrow 4\ell$ signal events, generated with $m_H = 125$ GeV for ggF production, and $qq \rightarrow ZZ^*$ background events. Only events satisfying the inclusive event selection requirements and with $115 < m_{4\ell} < 130$ GeV are considered. This range contains 95% of the signal and is asymmetric around 125 GeV to include the residual effects of FSR and bremsstrahlung. The discriminating variables used in the training are the transverse momentum of the four-lepton system ($p_T^{4\ell}$); the pseudorapidity of the four-lepton system ($\eta^{4\ell}$), correlated to the $p_T^{4\ell}$; and a matrix-element-based kinematic discriminant (D_{ZZ^*}). The discriminant D_{ZZ^*} is defined as

$$D_{ZZ^*} = \ln\left(\frac{|\mathcal{M}_{\text{sig}}|^2}{|\mathcal{M}_{ZZ}|^2}\right), \quad (1)$$

where \mathcal{M}_{sig} corresponds to the matrix element for the signal process, while \mathcal{M}_{ZZ} is the matrix element for the ZZ^* background process. The matrix elements for both signal and background are computed at leading order using MADGRAPH5 [96]. The matrix element for the signal is evaluated according to the SM hypothesis of a scalar boson with spin-parity $J^P = 0^+$ [7] and under the assumption that $m_H = m_{4\ell}$. Figures 8(a)–8(c) show the distributions of the variables used to train the BDT_{ZZ^*} classifier for the signal and the ZZ^* background. The separation between a SM Higgs signal and the ZZ^* background can be seen in Fig. 8(d).

As discussed in Sec. VIII, the BDT_{ZZ^*} output is exploited in the two-dimensional model built to measure the Higgs boson mass, the inclusive signal strength and the signal strength in the ggF enriched category.

B. BDT for categorization

For event categorization, two separate BDT classifiers were developed to discriminate against ggF production: one for VBF production (BDT_{VBF}) and another for the vector boson hadronic decays of VH production (BDT_{VH}). In the first case the BDT output is used as an observable together with $m_{4\ell}$ in a maximum likelihood fit for the VBF category, while in the latter case the BDT output value is used as a

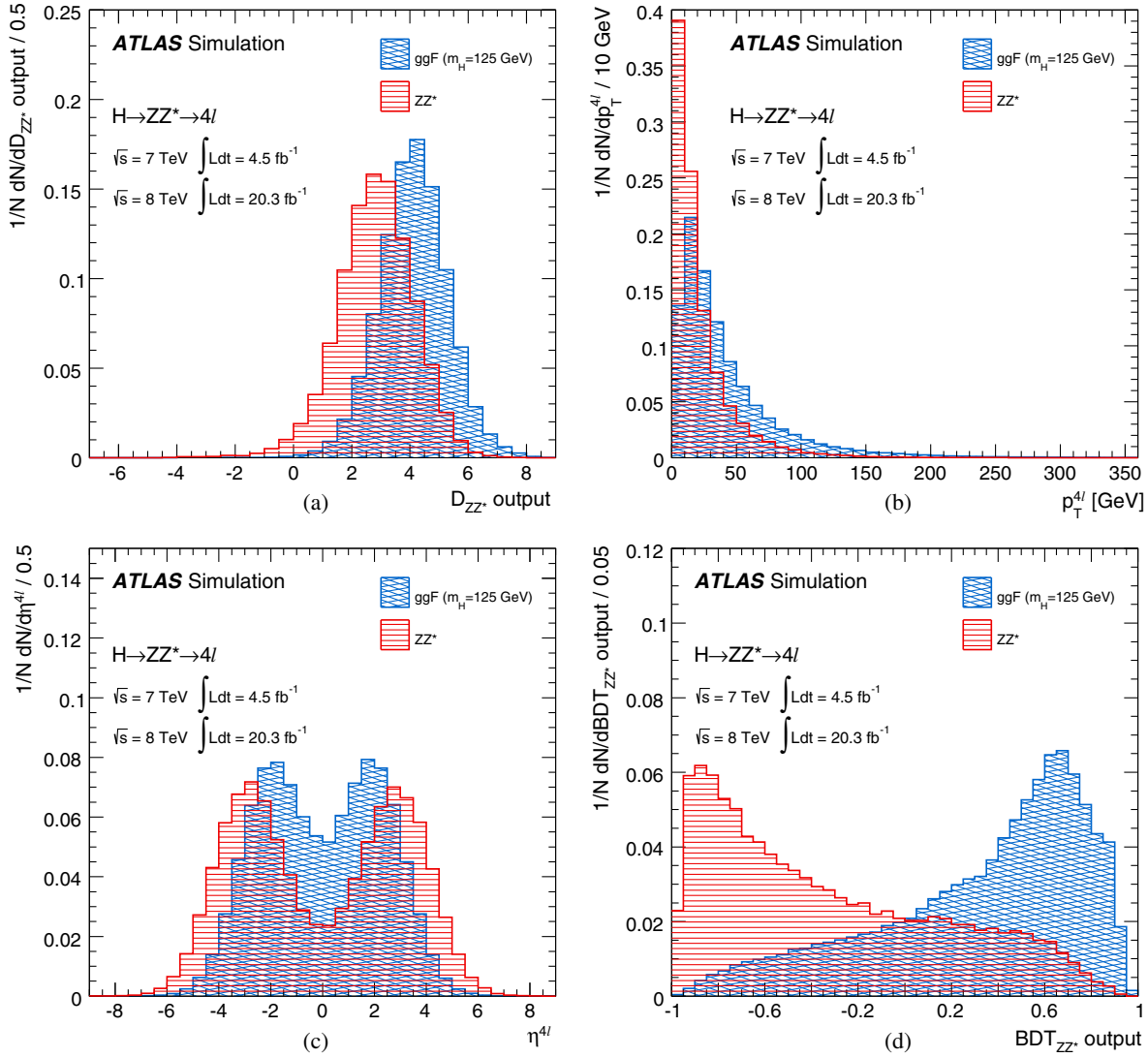


FIG. 8 (color online). Distributions for signal (blue) and ZZ* background (red) events, showing (a) D_{ZZ^*} output, (b) p_T^{4l} and (c) η^{4l} after the inclusive analysis selection in the mass range $115 < m_{4\ell} < 130$ GeV used for the training of the BDT_{ZZ^*} classifier. (d) BDT_{ZZ^*} output distribution for the signal (blue) and ZZ* background (red) in the mass range $115 < m_{4\ell} < 130$ GeV. All histograms are normalized to the same area.

selection requirement for the event to be classified in the VH-hadronic enriched category, as discussed in Sec. V B. In both cases the same five discriminating variables are used. In order of decreasing separation power between the two production modes, the variables are (a) invariant mass of the dijet system, (b) pseudorapidity separation between the two jets ($|\Delta\eta_{jj}|$), (c) transverse momentum of each jet, and (d) pseudorapidity of the leading jet.

For the training of the BDT discriminant, fully simulated four-lepton Higgs boson signal events produced through ggF and VBF production and hadronically decaying vector boson events for VH production are used. The distributions of these variables for BDT_{VBF} are presented in Figs. 9(a)–9(e), where all the expected features of the VBF production of a Higgs boson can be seen: the dijet system has a high invariant mass and the two jets are emitted in opposite

high- $|\eta|$ regions with a considerable $\Delta\eta$ separation between them. The jets of ggF events, on the other hand, are more centrally produced and have a smaller invariant mass and $\Delta\eta$ separation. The separation between VBF and ggF can be seen in the output of BDT_{VBF} in Fig. 9(f), where the separation between VBF and ZZ* is found to be similar. The output of BDT_{VBF} is unchanged for various mass points around the main training mass of $m_H = 125$ GeV. For variables entering the BDT_{VH} discriminant, the invariant mass of the dijet system, which peaks at the Z mass, exhibits the most important difference between ggF and VH production modes. The other variables have less separation power. The corresponding separation for BDT_{VH} is shown in Fig. 10. As described in Sec. V B, the VH-hadronic enriched category applies a selection on the BDT_{VH} discriminant (< -0.4) which optimizes the signal significance.

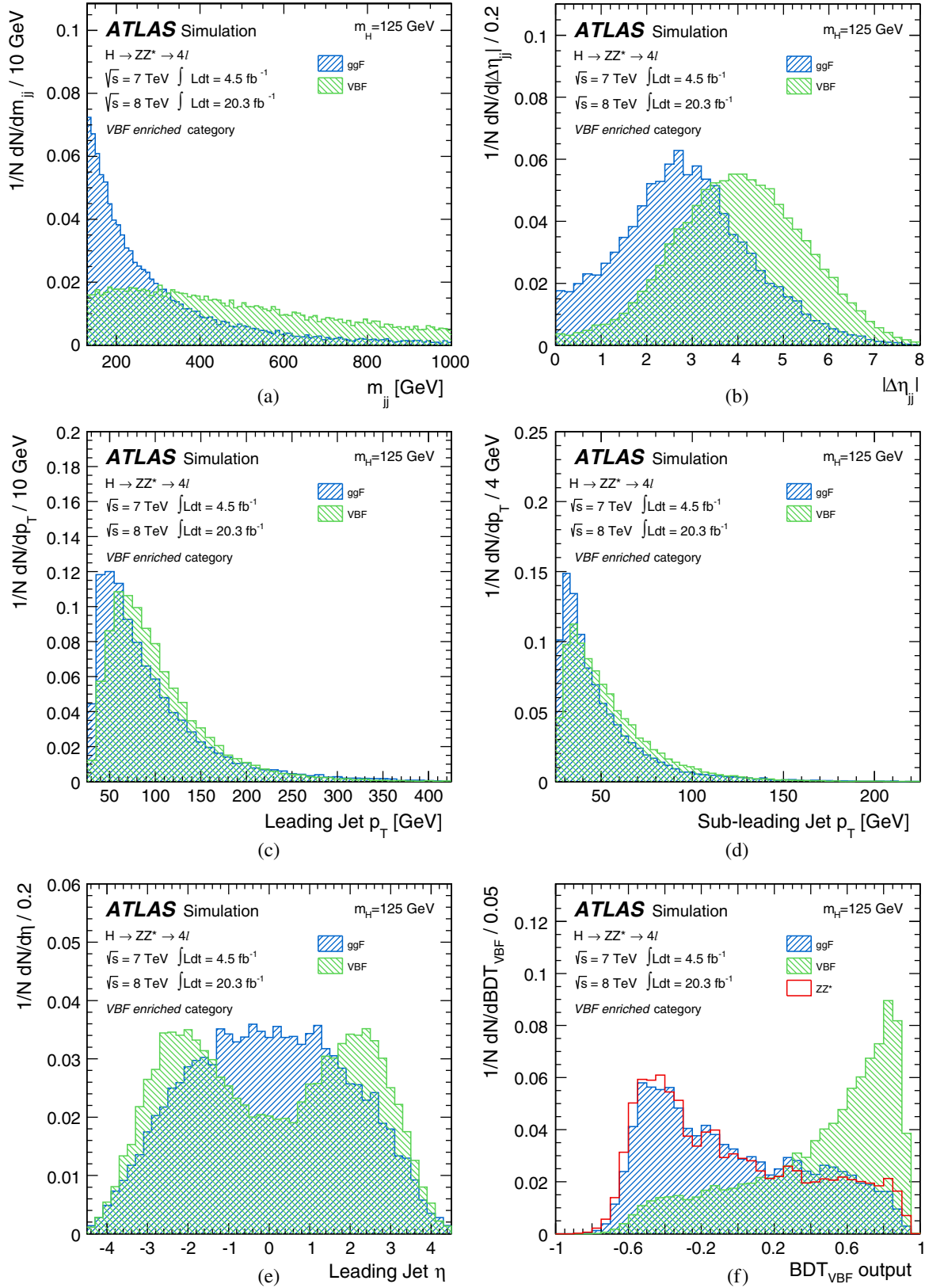


FIG. 9 (color online). Distribution of kinematic variables for signal (VBF events, green) and background (ggF events, blue) events used in the training of the VBF boosted decision tree: 9(a) dijet invariant mass, 9(b) dijet η separation, 9(c) leading jet p_T , 9(d) subleading jet p_T and 9(e) leading jet η . 9(f) Output distributions of BDT_{VBF} for VBF and ggF events as well as for the ZZ^* background (red). All histograms are normalized to the same area.

VIII. SIGNAL AND BACKGROUND MODELING

A. Signal and background modeling for the inclusive analysis

For the measurements of the Higgs boson mass, of its natural width and of the inclusive production rate relative to the SM expectation (the signal strength denoted as μ) in the $H \rightarrow ZZ^* \rightarrow 4\ell$ channel, three different parameterizations of the signal and background were developed as described in Ref. [9], where the Higgs boson mass measurement is reported. The baseline method is a two-dimensional (2D) fit to $m_{4\ell}$ and the BDT _{ZZ^*} output ($O_{\text{BDT}_{ZZ^*}}$). This method provides the smallest expected uncertainties for both the mass and inclusive signal strength measurements. The one-dimensional (1D) fit to the $m_{4\ell}$ distribution that was used in

the previous measurements [4,6] is used as a cross-check. A third method, using per-event resolution, is discussed after a description of the 1D and 2D models. The $m_{4\ell}$ range used in the fit for all of the methods is 110–140 GeV. A kernel density estimation method [97] uses fully simulated events to obtain smooth distributions for both the 1D and 2D signal models. These templates are produced using samples generated at 15 different m_H values in the range 115–130 GeV and parametrized as functions of m_H using B-spline interpolation [98]. These simulation samples at different masses are normalized to the expected SM $\sigma \times B$ [24] to derive the expected signal yields after acceptance and selection. The probability density function for the signal in the 2D fit is

$$\begin{aligned} \mathcal{P}(m_{4\ell}, O_{\text{BDT}_{ZZ^*}} | m_H) &= \mathcal{P}(m_{4\ell} | O_{\text{BDT}_{ZZ^*}}, m_H) \mathcal{P}(O_{\text{BDT}_{ZZ^*}} | m_H) \\ &\simeq \left(\sum_{n=1}^4 \mathcal{P}_n(m_{4\ell} | m_H) \theta_n(O_{\text{BDT}_{ZZ^*}}) \right) \mathcal{P}(O_{\text{BDT}_{ZZ^*}} | m_H) \end{aligned} \quad (2)$$

where θ_n defines four equal-sized bins for the value of the BDT _{ZZ^*} output, and \mathcal{P}_n represents the 1D probability density function of the signal in the corresponding BDT _{ZZ^*} bin. The variation of the $m_{4\ell}$ shape is negligible within a single BDT _{ZZ^*} bin, so no bias is introduced in the mass measurement. The background model, $\mathcal{P}_{\text{bkg}}(m_{4\ell}, O_{\text{BDT}_{ZZ^*}})$, is described using a two-dimensional probability density. For the ZZ^* and reducible $\ell\ell + \mu\mu$ backgrounds, the two-dimensional probability density distributions are derived from simulation, where the $\ell\ell + \mu\mu$ simulation was shown to agree well with data in the control region. For the $\ell\ell + ee$ background model, the two-dimensional probability density can only be obtained from data, which is done using the

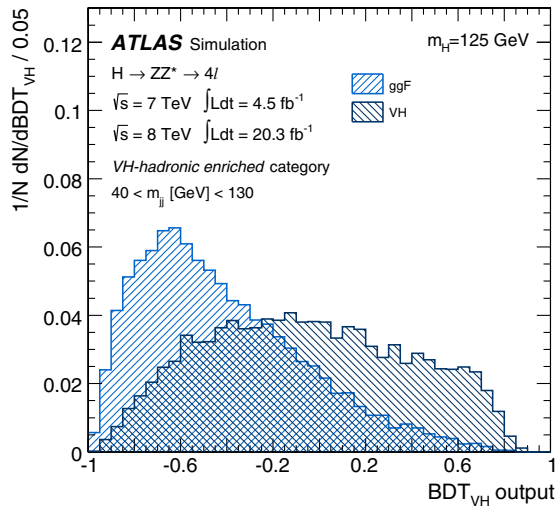


FIG. 10 (color online). Final BDT_{VH} discriminant output for the VH-hadronic enriched category for signal (VH events, dark blue) and background (ggF events, blue) events.

$3\ell + X$ data control region weighted with the transfer factor to match the kinematics of the signal region. Figure 11 shows the probability density in the BDT _{ZZ^*} - $m_{4\ell}$ plane, for the signal with $m_H = 125$ GeV, the ZZ^* background from simulation and the reducible background from the data control region. The visible separation between the signal and the background using the BDT _{ZZ^*} discriminant is exploited in the fit. With respect to the 1D approach, there is an expected reduction of the statistical uncertainty for the mass and inclusive signal strength measurements, which is estimated from simulation to be approximately 8% for both measurements. Both the 1D and the 2D models are built using $m_{4\ell}$ after applying a Z-mass constraint to m_{12} during the fit, as described in Sec. VA. Figure 12 shows the $m_{4\ell}$ distribution for a simulated signal sample with $m_H = 125$ GeV, after applying the correction for final-state radiation and the Z-mass constraint for the 4μ , $4e$ and $2e2\mu/2\mu2e$ final states. The width of the reconstructed Higgs boson mass for $m_H = 125$ GeV ranges between 1.6 GeV (4 μ final state) and 2.2 GeV (4 e final state) and is expected to be dominated by the experimental resolution since, for m_H of about 125 GeV, the natural width in the Standard Model is approximately 4 MeV.

In addition to the 1D and 2D fit methods described above, the signal probability density for $m_{4\ell}$ is also modeled on a per-event basis using both the BDT _{ZZ^*} information and the energy resolution of the individual leptons. This method is referred to as the per-event-resolution model and is used both as a cross-check for the mass measurement and as the baseline method to set an upper limit on the Higgs boson total width Γ_H , which is discussed elsewhere [9]. The detector-level $m_{4\ell}$ distribution for the signal is obtained for each event through the

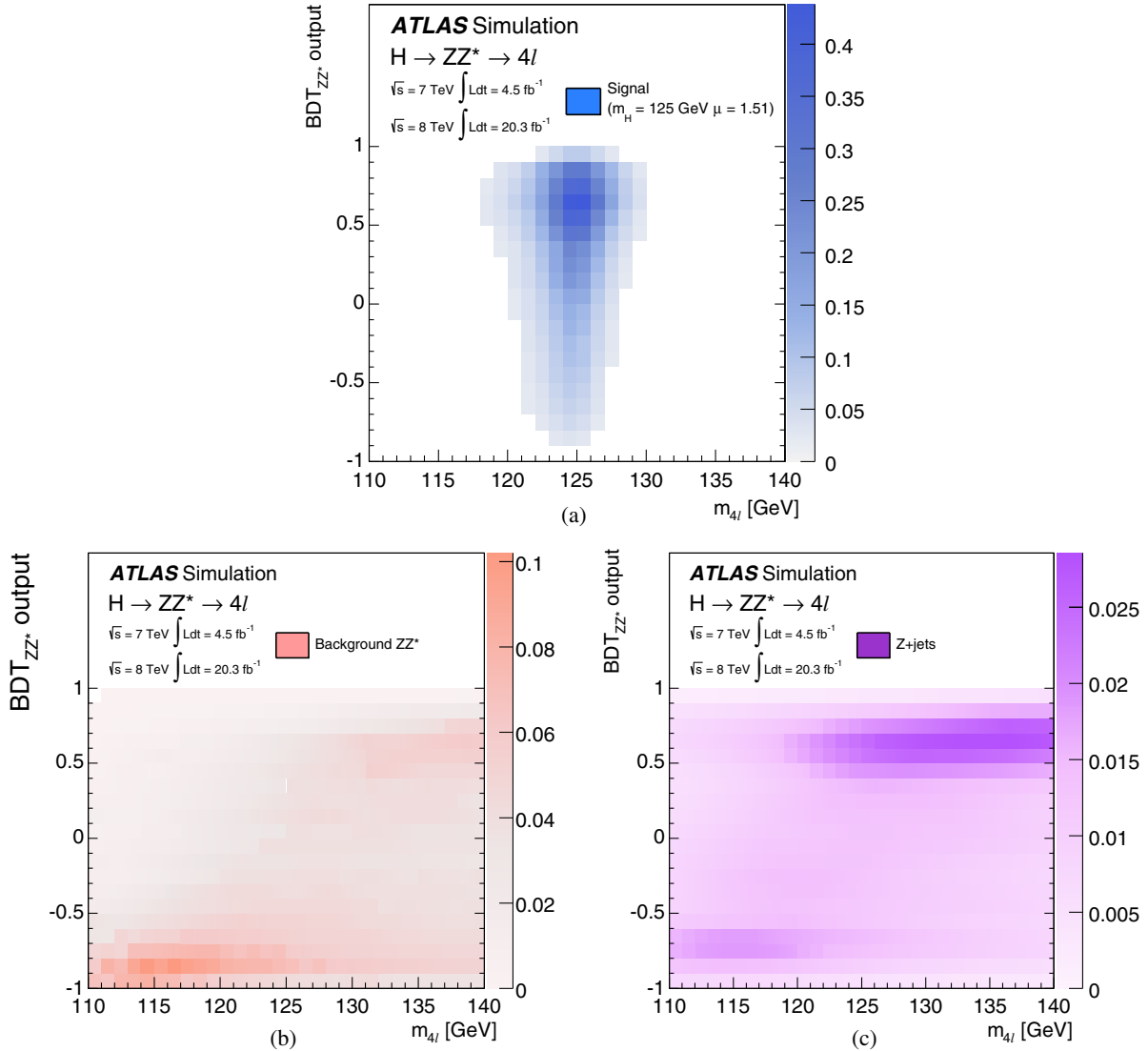


FIG. 11 (color online). Probability density for the signal and the different backgrounds normalized to the expected number of events for the 2011 and 2012 data sets, summing over all the final states: (a) $\mathcal{P}(m_{4\ell}, \text{BDT}_{ZZ^*} | m_H)$ for the signal assuming $m_H = 125 \text{ GeV}$, (b) probability density $\mathcal{P}(m_{4\ell}, \text{BDT}_{ZZ^*})$ for the ZZ^* background and (c) $\mathcal{P}(m_{4\ell}, \text{BDT}_{ZZ^*})$ for the reducible background.

convolution of an analytic description of the single-lepton detector response with a Breit-Wigner function that describes the Higgs boson mass line shape. The Z -mass constraint is not applied in this fit because this introduces a correlation between the two leptons of the leading Z which must be included in their detector response functions. The parametrization of the muon and electron response function is performed in bins of η and p_T of the leptons and consists of the sum of two or three normal distributions. This parametrization takes into account the tails of the single-lepton responses. A broad range of cross-checks were performed to validate all the models described above [9].

A likelihood function \mathcal{L} that depends on m_H and μ is constructed using the signal and background models defined above and is defined as

$$\mathcal{L}(m_H, \mu, \boldsymbol{\theta}) = \prod_i^{\text{year}} \prod_j^{\text{final state}} \text{Poisson}(N_{ij} | \mu \cdot S_{ij}(m_H, \boldsymbol{\theta}) + B_{ij}(\boldsymbol{\theta})) \cdot \prod_{k=1}^{N_{ij}} \mathcal{F}_{ij}((m_{4\ell}, O_{\text{BDT}_{ZZ^*}})_k, m_H, \mu, \boldsymbol{\theta}). \quad (3)$$

This likelihood function corresponds to the product of the Poisson probability of observing N_{ij} events in the 2011 and 2012 data sets and each of the four final states, given the expectation for the signal S_{ij} and background B_{ij} , and is multiplied with the product of the values of the probability density \mathcal{F}_{ij} , for $(m_{4\ell}, O_{\text{BDT}_{ZZ^*}})_k$ of all events. \mathcal{F}_{ij} is constructed by using both the signal and background probability density described above. The symbol $\boldsymbol{\theta}$ represents the set of nuisance parameters used to model the effect of the systematic uncertainties described in Sec. IX.

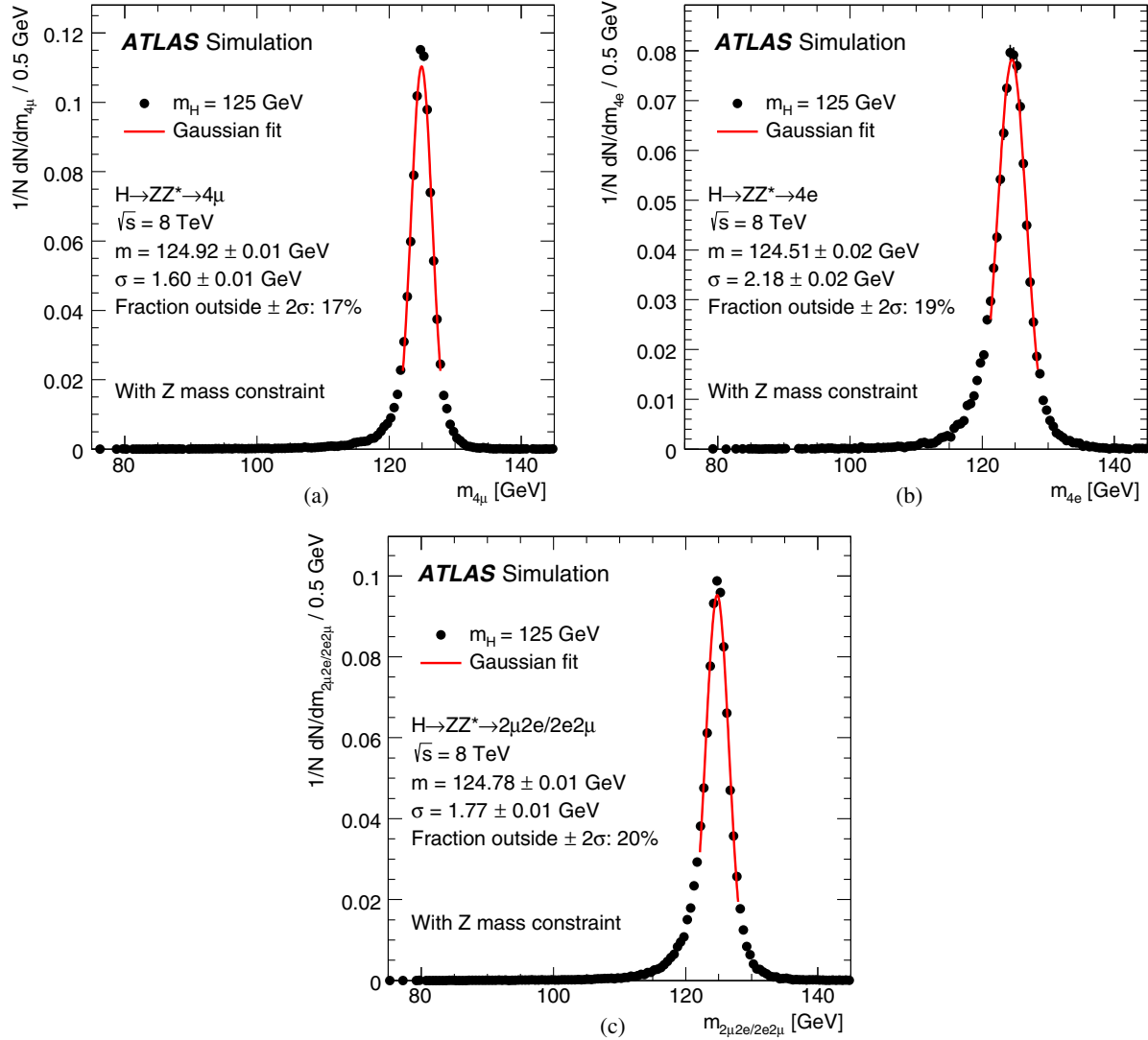


FIG. 12 (color online). Invariant mass distribution for a simulated signal sample with $m_H = 125$ GeV; superimposed is the Gaussian fit to the $m_{4\ell}$ peak after the correction for final-state radiation and the Z -mass constraint.

The statistical procedure used to interpret the data is described in Refs. [99,100]. The confidence intervals are based on the profile likelihood ratios $\Lambda(\boldsymbol{\alpha})$ that depend on one or more parameters of interest $\boldsymbol{\alpha}$ (i.e. the Higgs boson mass or the signal strength) and on the nuisance parameters $\boldsymbol{\theta}$:

$$\Lambda(\boldsymbol{\alpha}) = \frac{\mathcal{L}(\boldsymbol{\alpha}, \hat{\boldsymbol{\theta}}(\boldsymbol{\alpha}))}{\mathcal{L}(\hat{\boldsymbol{\alpha}}, \hat{\boldsymbol{\theta}})}. \quad (4)$$

The likelihood fit to the data is then performed for the parameters of interest; $\hat{\boldsymbol{\theta}}$ corresponds to the value of $\boldsymbol{\theta}$ which maximizes \mathcal{L} for the specified $\boldsymbol{\alpha}$, and $\hat{\boldsymbol{\theta}}$ denotes the unconditional maximum likelihood estimate of the nuisance parameters, i.e. where the likelihood is maximized for both $\boldsymbol{\theta}$ and $\boldsymbol{\alpha}$. In particular, the profile likelihood ratios $\Lambda(m_H)$ and $\Lambda(\mu)$, used for the Higgs boson mass

and the inclusive signal strength measurements, respectively, are

$$\begin{aligned} \Lambda(m_H) &= \frac{\mathcal{L}(m_H, \hat{\mu}(m_H), \hat{\boldsymbol{\theta}}(m_H))}{\mathcal{L}(\hat{m}_H, \hat{\mu}, \hat{\boldsymbol{\theta}})} \quad \text{and} \\ \Lambda(\mu) &= \frac{\mathcal{L}(\mu, \hat{\boldsymbol{\theta}}(\mu))}{\mathcal{L}(\hat{\mu}, \hat{\boldsymbol{\theta}})}, \end{aligned} \quad (5)$$

where the profile likelihood ratio for m_H has the signal strength treated as a parameter of interest in the fit, while that for μ is evaluated for a fixed value of m_H .

B. Signal and background modeling for the categorized analysis

The model developed for the categorized analysis allows the measurement of the signal strength for the different

production modes. Since no direct $t\bar{t}H$ and $b\bar{b}H$ production is observed, a common signal strength $\mu_{\text{ggF+}t\bar{t}H+b\bar{b}H}$ is assigned to gluon fusion, $t\bar{t}H$ and $b\bar{b}H$ production. This simplification is also justified by the fact that in the SM the two production modes scale with the $q\bar{q}H$ ($q = b, t$) coupling. Similarly, a common signal strength $\mu_{\text{VBF+VH}}$ is assigned to the VBF and VH production modes since in the SM they scale with the WH/ZH gauge couplings.

For the categorized analysis, all of the candidates are grouped into four separate categories to have better sensitivity to the different production mechanisms, as described in Sec. V. In the VBF enriched category, where the BDT_{VBF} discriminant is introduced to separate the ggF-like events from VBF-like events, the two-dimensional probability density $\mathcal{P}(m_{4\ell}, \text{BDT}_{\text{VBF}})$ is constructed by factorizing the BDT_{VBF} and $m_{4\ell}$ distributions. This factorization is justified by the negligible dependence of the BDT_{VBF} on $m_{4\ell}$ for both signal and background. The BDT_{VBF} dependence on the Higgs boson mass is negligible and is neglected in the probability density. Adding the BDT_{VBF} in the VBF enriched category reduces the expected uncertainty on the signal strength of the VBF and VH production mechanisms $\mu_{\text{VBF+VH}}$ by about 25%. The improvement in the expected uncertainty on $\mu_{\text{VBF+VBF+VH}}$ reaches approximately 35% after adding the leptonic and hadronic VH categories to the model. In these two VH categories, a simple one-dimensional fit to the $m_{4\ell}$ observable is performed, since for the VH-hadronic enriched category, a selection on the BDT_{VH} output is included in the event selection, while for the VH-leptonic enriched category, no BDT is used. Finally, in the ggF enriched category, the 2D model defined in Eq. (2), including the BDT_{ZZ^*} trained as specified in Sec. VIIA, is used. These procedures allow a further reduction of the expected uncertainty on $\mu_{\text{VBF+VH}}$ ($\mu_{\text{ggF+}t\bar{t}H+b\bar{b}H}$) by 6% (8%).

IX. SYSTEMATIC UNCERTAINTIES

The uncertainties on the lepton reconstruction and identification efficiency, and on the lepton energy or momentum resolution and scale, are determined using samples of W , Z and J/ψ decays. The description of these systematic uncertainties, as well as of the uncertainties associated with the event categorizations, is separated into three parts. A brief overview of the systematic uncertainties that affect the mass measurement is given in Sec. IXA. The description of the systematic uncertainties related to the measurement of the signal rate and event categorizations is provided in Secs. IXB and IXC, respectively.

A. Systematic uncertainties in the mass measurement

For the $H \rightarrow ZZ^* \rightarrow 4\ell$ decay modes involving electrons, the electron energy scale uncertainty, determined from $Z \rightarrow ee$ and $J/\psi \rightarrow ee$ decays, is propagated as a function of the pseudorapidity and the transverse energy of

the electrons. The precision of the energy scale is better than 0.1% for $|\eta| < 1.2$ and $1.8 < |\eta| < 2.47$, and a few per mille for $1.2 < |\eta| < 1.8$ [76]. The uncertainties on the measured Higgs boson mass due to the electron energy scale uncertainties are $\pm 0.04\%$, $\pm 0.025\%$ and $\pm 0.04\%$ for the $4e$, $2e2\mu$ and $2\mu2e$ final states, respectively.

Similarly, for the $H \rightarrow ZZ^* \rightarrow 4\ell$ decay modes involving muons, the various components of the systematic uncertainty on the muon momentum scale are determined using large samples of $J/\psi \rightarrow \mu\mu$ and $Z \rightarrow \mu\mu$ decays and validated using $Y \rightarrow \mu\mu$, $J/\psi \rightarrow \mu\mu$ and $Z \rightarrow \mu\mu$ decays. In the muon transverse momentum range of 6–100 GeV, the systematic uncertainties on the scales are about $\pm 0.04\%$ in the barrel region and reach $\pm 0.2\%$ in the region $|\eta| > 2$ [81]. The uncertainties on the measured Higgs boson mass due to the muon energy scale uncertainties are estimated to be $\pm 0.04\%$, $\pm 0.015\%$ and $\pm 0.02\%$ for the 4μ , $2e2\mu$ and $2\mu2e$ final states, respectively.

Uncertainties on the measured Higgs boson mass related to the background contamination and final-state QED radiation modeling are negligible compared to the other sources described above.

The weighted contributions to the uncertainty in the mass measurement, when all the final states are combined, are $\pm 0.01\%$ for the electron energy scale uncertainty and $\pm 0.03\%$ for the muon momentum scale uncertainty. The larger impact of the muon momentum scale uncertainty is due to the fact that the muon final states have a greater weight in the combined mass fit.

B. Systematic uncertainties in the inclusive signal strength measurement

The efficiencies to trigger, reconstruct and identify electrons and muons are studied using $Z \rightarrow \ell\ell$ and $J/\psi \rightarrow \ell\ell$ decays [78–81]. The expected impact from simulation of the associated systematic uncertainties on the signal yield is presented in Table IX. The impact is presented for the individual final states and for all channels combined.

The level of agreement between data and simulation for the efficiency of the isolation and impact parameter requirements of the analysis is studied using a tag-and-probe method. As a result, a small additional uncertainty on the isolation and impact parameter selection efficiency is applied for electrons with E_T below 15 GeV. The effect of the isolation and impact parameter uncertainties on the signal strength is given in Table IX. The corresponding uncertainty for muons is found to be negligible.

The uncertainties on the data-driven estimates of the background yields are discussed in Sec. VI and are summarized in Tables V and VII, and their impact on the signal strength is given in Table IX.

The overall uncertainty on the integrated luminosity for the complete 2011 data set is $\pm 1.8\%$ [101]. The uncertainty on the integrated luminosity for the 2012 data set is $\pm 2.8\%$; this uncertainty is derived following the methodology used

TABLE IX. The expected impact of the systematic uncertainties on the signal yield, derived from simulation, for $m_H = 125$ GeV, are summarized for each of the four final states for the combined 4.5 fb^{-1} at $\sqrt{s} = 7$ TeV and 20.3 fb^{-1} at $\sqrt{s} = 8$ TeV. The symbol “–” signifies that the systematic uncertainty does not contribute to a particular final state. The last three systematic uncertainties apply equally to all final states. All uncertainties have been symmetrized.

Source of uncertainty	4μ	$2e2\mu$	$2\mu2e$	$4e$	combined
Electron reconstruction and identification efficiencies	–	1.7%	3.3%	4.4%	1.6%
Electron isolation and impact parameter selection	–	0.07%	1.1%	1.2%	0.5%
Electron trigger efficiency	–	0.21%	0.05%	0.21%	< 0.2%
$\ell\ell + ee$ backgrounds	–	–	3.4%	3.4%	1.3%
Muon reconstruction and identification efficiencies	1.9%	1.1%	0.8%	–	1.5%
Muon trigger efficiency	0.6%	0.03%	0.6%	–	0.2%
$\ell\ell + \mu\mu$ backgrounds	1.6%	1.6%	–	–	1.2%
QCD scale uncertainty					6.5%
PDF, α_s uncertainty					6.0%
$H \rightarrow ZZ^*$ branching ratio uncertainty					4.0%

for the 2011 data set, from a preliminary calibration of the luminosity scale with beam-separation scans performed in November 2012.

The theory-related systematic uncertainty for both the signal and the ZZ^* background is discussed in Sec. III. The three most important theoretical uncertainties, which dominate the signal strength uncertainty, are given in Table IX. Uncertainties on the predicted Higgs boson p_T spectrum due to those on the PDFs and higher-order corrections are estimated to affect the signal strength by less than $\pm 1\%$. The systematic uncertainty of the ZZ^*

background rate is around $\pm 4\%$ for $m_{4\ell} = 125$ GeV and increases for higher mass, averaging to around $\pm 6\%$ for the ZZ^* production above 110 GeV.

C. Systematic uncertainties in the event categorization

The systematic uncertainties on the expected yields (as in Table II) from different processes contributing to the VBF enriched, VH-leptonic enriched, VH-hadronic enriched and ggF enriched categories are reported in Table X, expressed as the fractional uncertainties on the yields. The uncertainties on the theoretical predictions for

TABLE X. Systematic uncertainties on the yields expected from various processes contributing to the VBF enriched, VH-leptonic enriched, VH-hadronic enriched and ggF enriched categories expressed as percentages of the yield. The various uncertainties are added in quadrature. Uncertainties that are negligible are denoted by a “–”. All uncertainties have been symmetrized.

Process	$gg \rightarrow H, q\bar{q}/gg \rightarrow b\bar{b}H/\bar{t}tH$	$qq' \rightarrow Hqq'$	$q\bar{q} \rightarrow W/ZH$	ZZ^*
VBF enriched category				
Theoretical cross section	20.4%	4%	4%	8%
Underlying event	6.6%	1.4%	–	–
Jet energy scale	9.6%	4.8%	7.8%	9.6%
Jet energy resolution	0.9%	0.2%	1.0%	1.4%
Total	23.5%	6.4%	8.8%	12.6%
VH-hadronic enriched category				
Theoretical cross section	20.4%	4%	4%	2%
Underlying event	7.5%	3.1%	–	–
Jet energy scale	9.4%	9.3%	3.7%	12.6%
Jet energy resolution	1.0%	1.7%	0.6%	1.8%
Total	23.7%	10.7%	5.5%	12.9%
VH-leptonic enriched category				
Theoretical cross section	12%	4%	4%	5%
Leptonic VH-specific cuts	1%	1%	5%	–
Jet energy scale	8.8%	9.9%	1.7%	3.2%
Total	14.9%	10.7%	6.6%	5.9%
ggF enriched category				
Theoretical cross section	12%	4%	4%	4%
Jet energy scale	2.2%	6.6%	4.0%	1.0%
Total	12.2%	7.7%	5.7%	4.1%

TABLE XI. The number of events expected and observed for a $m_H = 125$ GeV hypothesis for the four-lepton final states in a window of $120 < m_{4\ell} < 130$ GeV. The second column shows the number of expected signal events for the full mass range, without a selection on $m_{4\ell}$. The other columns show for the 120–130 GeV mass range the number of expected signal events, the number of expected ZZ^* and reducible background events, and the signal-to-background ratio (S/B), together with the number of observed events, for 4.5 fb^{-1} at $\sqrt{s} = 7 \text{ TeV}$ and 20.3 fb^{-1} at $\sqrt{s} = 8 \text{ TeV}$ as well as for the combined sample.

Final state	Signal full mass range	Signal	ZZ^*	$Z + \text{jets}, t\bar{t}$	S/B	Expected	Observed
$\sqrt{s} = 7 \text{ TeV}$							
4μ	1.00 ± 0.10	0.91 ± 0.09	0.46 ± 0.02	0.10 ± 0.04	1.7	1.47 ± 0.10	2
$2e2\mu$	0.66 ± 0.06	0.58 ± 0.06	0.32 ± 0.02	0.09 ± 0.03	1.5	0.99 ± 0.07	2
$2\mu2e$	0.50 ± 0.05	0.44 ± 0.04	0.21 ± 0.01	0.36 ± 0.08	0.8	1.01 ± 0.09	1
$4e$	0.46 ± 0.05	0.39 ± 0.04	0.19 ± 0.01	0.40 ± 0.09	0.7	0.98 ± 0.10	1
Total	2.62 ± 0.26	2.32 ± 0.23	1.17 ± 0.06	0.96 ± 0.18	1.1	4.45 ± 0.30	6
$\sqrt{s} = 8 \text{ TeV}$							
4μ	5.80 ± 0.57	5.28 ± 0.52	2.36 ± 0.12	0.69 ± 0.13	1.7	8.33 ± 0.6	12
$2e2\mu$	3.92 ± 0.39	3.45 ± 0.34	1.67 ± 0.08	0.60 ± 0.10	1.5	5.72 ± 0.37	7
$2\mu2e$	3.06 ± 0.31	2.71 ± 0.28	1.17 ± 0.07	0.36 ± 0.08	1.8	4.23 ± 0.30	5
$4e$	2.79 ± 0.29	2.38 ± 0.25	1.03 ± 0.07	0.35 ± 0.07	1.7	3.77 ± 0.27	7
Total	15.6 ± 1.6	13.8 ± 1.4	6.24 ± 0.34	2.00 ± 0.28	1.7	22.1 ± 1.5	31
$\sqrt{s} = 7 \text{ TeV}$ and $\sqrt{s} = 8 \text{ TeV}$							
4μ	6.80 ± 0.67	6.20 ± 0.61	2.82 ± 0.14	0.79 ± 0.13	1.7	9.81 ± 0.64	14
$2e2\mu$	4.58 ± 0.45	4.04 ± 0.40	1.99 ± 0.10	0.69 ± 0.11	1.5	6.72 ± 0.42	9
$2\mu2e$	3.56 ± 0.36	3.15 ± 0.32	1.38 ± 0.08	0.72 ± 0.12	1.5	5.24 ± 0.35	6
$4e$	3.25 ± 0.34	2.77 ± 0.29	1.22 ± 0.08	0.76 ± 0.11	1.4	4.75 ± 0.32	8
Total	18.2 ± 1.8	16.2 ± 1.6	7.41 ± 0.40	2.95 ± 0.33	1.6	26.5 ± 1.7	37

the cross sections for the different processes arise mainly from the requirement on the jet multiplicity used in the event categorization [102,103]. Because of event migrations, this also affects the VH-leptonic enriched and ggF

enriched categories, where no explicit requirement on jets is applied. The uncertainty accounting for a potential mismodeling of the underlying event is conservatively estimated with $Z \rightarrow \mu\mu$ simulated events by applying the

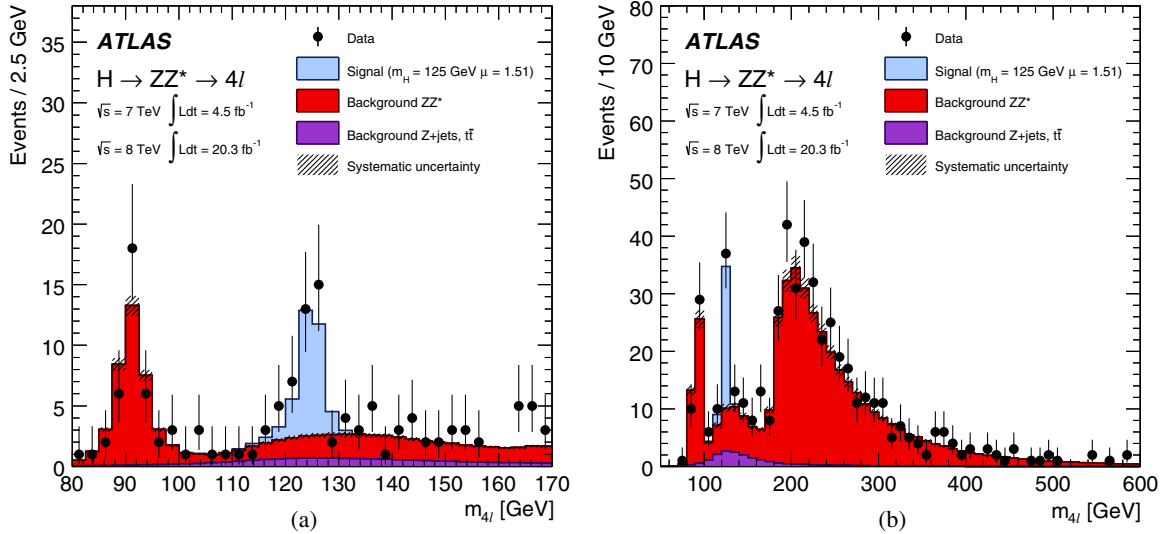


FIG. 13 (color online). The distribution of the four-lepton invariant mass, $m_{4\ell}$, for the selected candidates (filled circles) compared to the expected signal and background contributions (filled histograms) for the combined $\sqrt{s} = 7 \text{ TeV}$ and $\sqrt{s} = 8 \text{ TeV}$ data for the mass ranges: (a) 80–170 GeV, and (b) 80–600 GeV. The signal expectation shown is for a mass hypothesis of $m_H = 125$ GeV and normalized to $\mu = 1.51$ (see text). The expected backgrounds are shown separately for the ZZ^* (red histogram), and the reducible $Z + \text{jets}$ and $t\bar{t}$ backgrounds (violet histogram); the systematic uncertainty associated to the total background contribution is represented by the hatched areas.

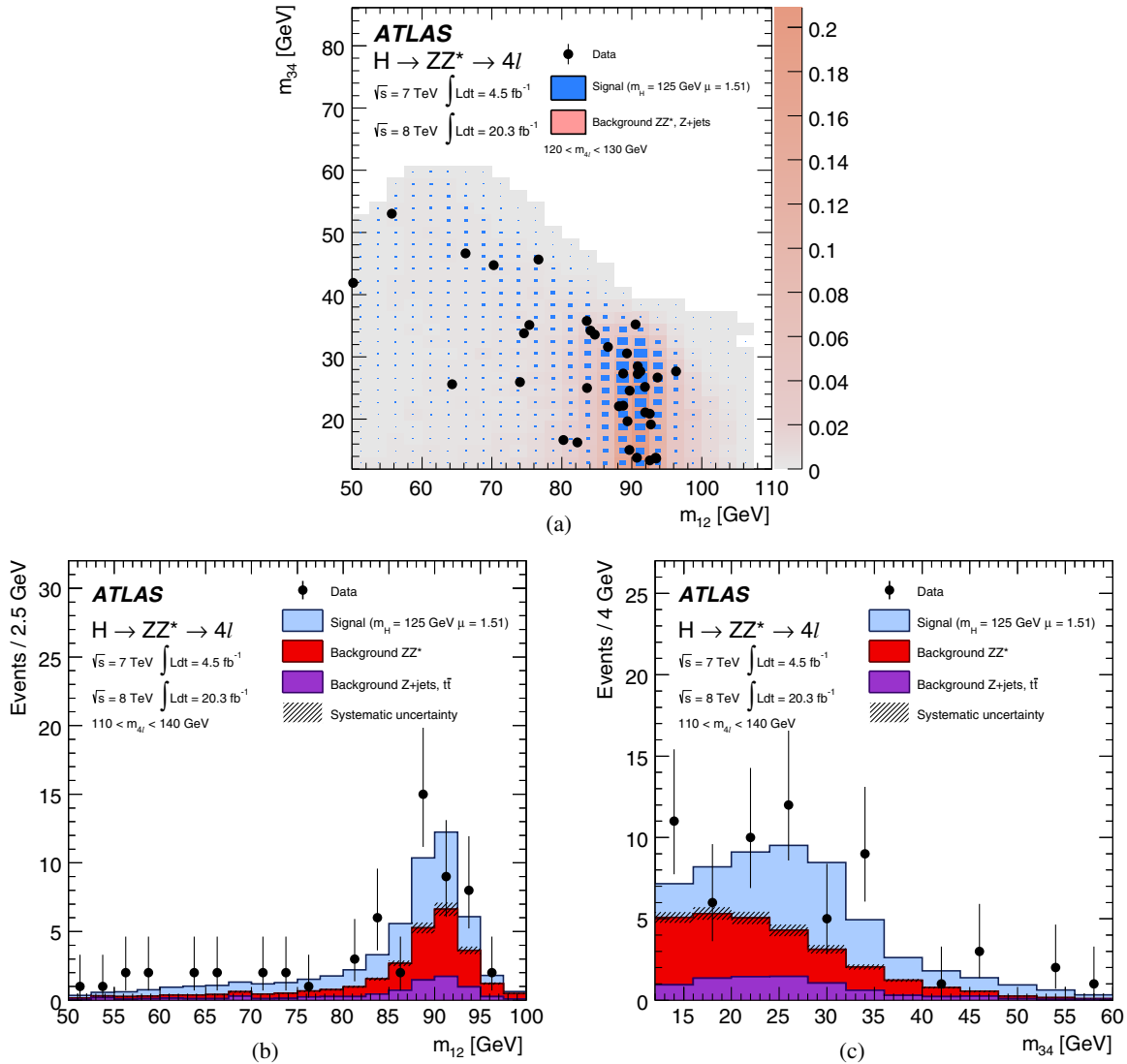


FIG. 14 (color online). Distributions of data (filled circles) and the expected signal and backgrounds events in (a) the m_{34} - m_{12} plane with the requirement of $m_{4\ell}$ in 120 – 130 GeV. The projected distributions for (b) m_{12} and (c) m_{34} are shown for m_H in 110 – 140 GeV, the fit range. The signal contribution is shown for $m_H = 125$ GeV and normalized to $\mu = 1.51$ (see text) as blue histograms in (b) and (c). The expected background contributions, ZZ^* (red histogram) and $Z + \text{jets}$ plus $t\bar{t}$ (violet histogram), are shown in (b) and (c); the systematic uncertainty associated to the total background contribution is represented by the hatched areas. The expected distributions of the Higgs signal (blue) and total background (red) are superimposed in (a), where the box size (signal) and color shading (background) represent the relative density. In every case, the combination of the 7 and 8 TeV results is shown.

selection for the VBF enriched (or VH-hadronic enriched) category and taking the difference of the efficiencies with and without multiparton interactions.

The main experimental uncertainty is related to the jet energy scale determination, including the uncertainties associated with the modeling of the absolute and relative *in situ* jet calibrations, as well as the flavor composition of the jet sample. The impact on the yields of the various categories is anticorrelated because a variation of the jet energy scale results primarily in the migration of events among the categories. The impact of the jet energy scale

uncertainty results in an uncertainty of about $\pm 10\%$ for the VBF enriched category, $\pm 8\%$ for the VH-hadronic enriched category, $\pm 1.5\%$ for the VH-leptonic enriched category and $\pm 1.5\%$ for the ggF enriched category.

The uncertainty on the jet energy resolution is also taken into account, even though its impact is small compared to that of the jet energy scale uncertainty, as reported in Table X. Finally, the uncertainties associated with the additional leptons in the VH-leptonic enriched category are the same as already described in Sec. IX B for the four leptons of the Higgs boson decay.

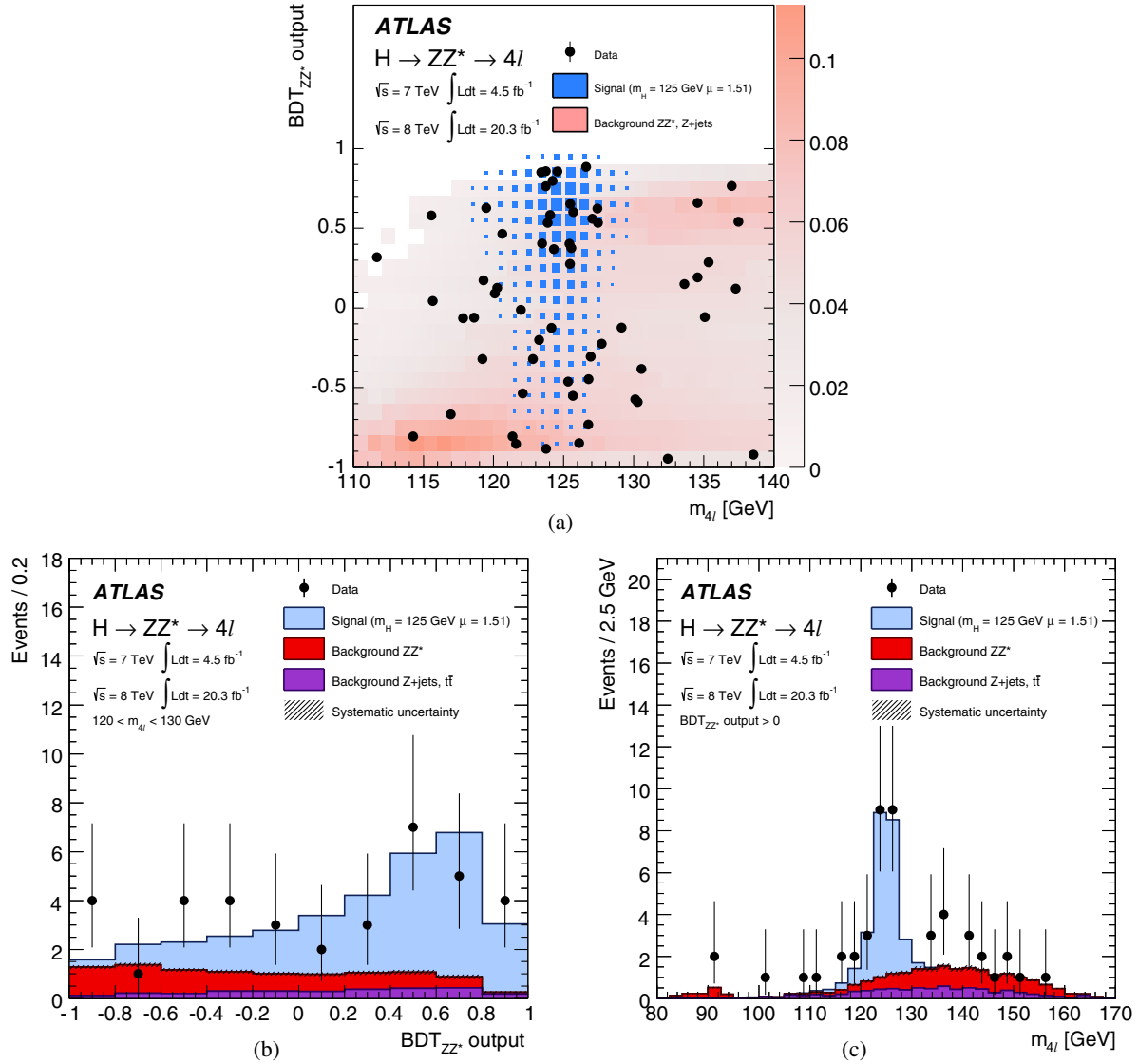


FIG. 15 (color online). Distributions of data (filled circles) and the expected signal and background events in (a) the BDT_{ZZ^*} - $m_{4\ell}$ plane, (b) BDT_{ZZ^*} with the restriction $120 < m_{4\ell} < 130 \text{ GeV}$, and (c) $m_{4\ell}$ with the additional requirement that the BDT_{ZZ^*} be positive. The expected Higgs signal contribution is shown for $m_H = 125 \text{ GeV}$ and normalized to $\mu = 1.51$ (see text) as blue histograms in (b) and (c). The expected background contributions, ZZ^* (red histogram) and $Z + \text{jets}$ plus $t\bar{t}$ (violet histogram), are shown in (b) and (c); the systematic uncertainty associated to the total background contribution is represented by the hatched areas. The expected distributions of the Higgs signal (blue) and total background (red) are superimposed in (a), where the box size (signal) and color shading (background) represent the relative density. In every case, the combination of the 7 and 8 TeV results is shown.

X. Results

A. Results of the inclusive analysis

As described in Sec. V A, the inclusive selection is used to measure the Higgs boson mass. In addition, the inclusive signal strength measurement, described below, allows a direct comparison with the predicted total production cross section times branching ratio of the Standard Model Higgs boson at the measured mass. This inclusive analysis is the same as that used for the combined mass measurement [9]; in the following more details and new comparisons of the data and expectations

are provided in view of the inclusive mass and signal strength measurements.

1. Signal and background yields

The number of observed candidate events for each of the four decay channels in a mass window of 120–130 GeV and the signal and background expectations are presented in Table XI. The signal and ZZ^* background expectations are normalized to the SM expectation while the reducible background is normalized to the data-driven estimate described in Sec. VI. Three events in the mass range

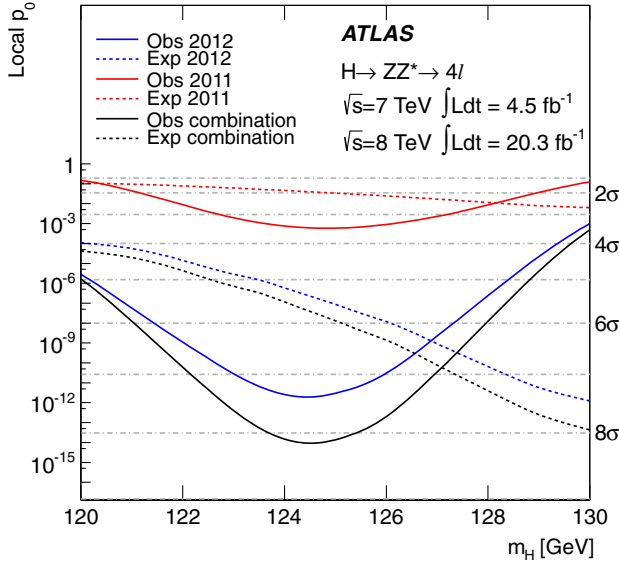


FIG. 16 (color online). The observed local p_0 -value for the combination of the 2011 and 2012 data sets (solid black line) as a function of m_H ; the individual results for $\sqrt{s} = 7$ TeV and 8 TeV are shown separately as red and blue solid lines, respectively. The dashed curves show the expected median of the local p_0 -value for the signal hypothesis with signal strength $\mu = 1$, when evaluated at the corresponding m_H . The horizontal dot-dashed lines indicate the p_0 -values corresponding to local significances of 1–8 σ .

$120 < m_{4\ell} < 130$ GeV are corrected for FSR: one 4μ event and one $2\mu 2e$ are corrected for noncollinear FSR, and one $2\mu 2e$ event is corrected for collinear FSR. In the full mass spectrum, there are 8 (2) events corrected for collinear (noncollinear) FSR, in good agreement with the expected number of 11 events.

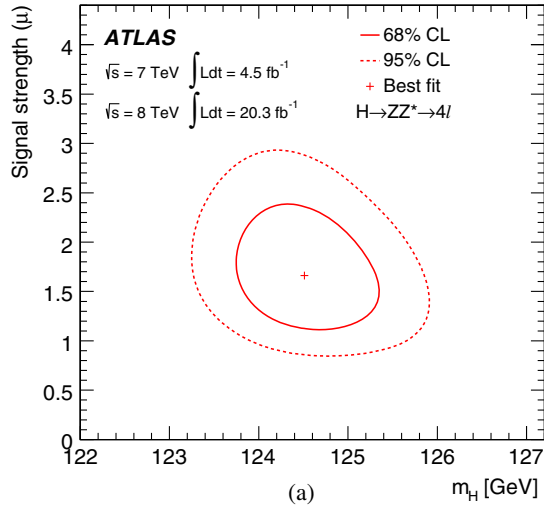
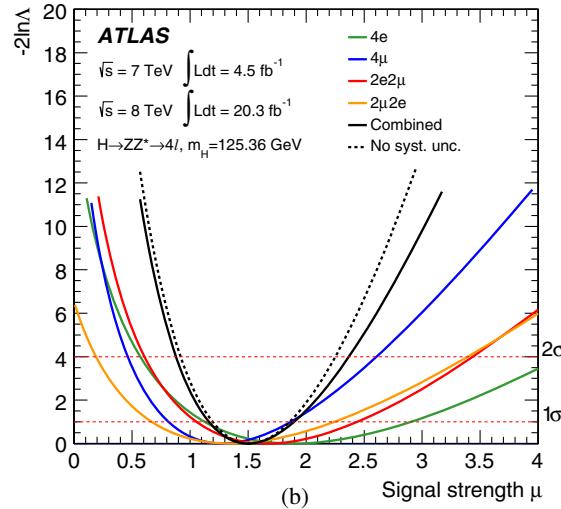


FIG. 17 (color online). (a) The 68% and 95% confidence level (CL) contours in the $\mu-m_H$ plane for the inclusive analysis. (b) The profile likelihood as a function of the inclusive signal strength μ for the individual channels ($4e$, green line; 4μ , blue line; $2e2\mu$, red line; $2\mu 2e$, yellow line) as well as for their combination (black lines); the scan for the combination of all channels is shown both with (solid line) and without (dashed line) systematic uncertainties. The value of m_H is fixed to 125.36 GeV while all the other nuisance parameters are profiled in the fit. In every case, the combination of the 7 and 8 TeV results is shown.

The expected $m_{4\ell}$ distribution for the backgrounds and the signal hypothesis are compared with the combined $\sqrt{s} = 7$ TeV and $\sqrt{s} = 8$ TeV data in Fig. 13 for the $m_{4\ell}$ range 80–170 GeV, and in Fig. 13(b) for the invariant mass range 80–600 GeV. In Fig. 13 one observes the single $Z \rightarrow 4\ell$ resonance [104,105], the threshold of the ZZ production above 180 GeV and a narrow peak around 125 GeV. Figure 14 shows the distribution of the m_{12} versus m_{34} invariant masses, as well as their projections, for the candidates with $m_{4\ell}$ within 120–130 GeV. The Z -mass constrained kinematic fit is not applied for these distributions. The Higgs signal is shown for $m_H = 125$ GeV with a value of $\mu = 1.51$, corresponding to the combined μ measurement for the $H \rightarrow ZZ^* \rightarrow 4\ell$ final state, discussed below in Sec. XB, scaled to this mass by the expected variation in the SM Higgs boson cross section times branching ratio.

The distribution of the BDT_{ZZ^*} output versus $m_{4\ell}$ is shown in Fig. 15(a) for the reconstructed candidates with $m_{4\ell}$ within the fitted mass range 110–140 GeV. An excess of events with high- BDT_{ZZ^*} output is present for values of $m_{4\ell}$ close to 125 GeV, compatible with the Higgs signal hypothesis at that mass. The compatibility of the data with the expectations shown in Fig. 15(a) is checked using pseudoexperiments generated according to the expected two-dimensional distribution and good agreement is found. Figure 15(b) shows the distribution of the BDT_{ZZ^*} output for the candidates in the $m_{4\ell}$ range 120–130 GeV compared with signal and background expectations. In Fig. 15(c) the distribution of the invariant mass of the four leptons is presented for candidates satisfying the requirement that the value of the BDT_{ZZ^*} output be greater than zero, which maximizes the expected significance for a SM Higgs boson with a mass of about 125 GeV.



The local p_0 -value of the observed signal, representing the significance of the excess relative to the background-only hypothesis, is obtained with the asymptotic approximation [100] using the 2D fit without any selection on BDT_{ZZ^*} and is shown as a function of m_H in Fig. 16. The local p_0 -value at the measured mass for this channel, 124.51 GeV (see below), is 8.2 standard deviations. At the value of the Higgs boson mass, $m_H = 125.36$ GeV, obtained from the combination of the $H \rightarrow ZZ^* \rightarrow 4\ell$ and $H \rightarrow \gamma\gamma$ mass measurements [9], the local p_0 -value decreases to 8.1 standard deviations. The expected significance at these two masses is 5.8 and 6.2 standard deviations, respectively.

2. Mass and inclusive signal strength

The models described in Sec. VIII A are used to perform the inclusive mass and signal strength measurements. The measured Higgs boson mass obtained with the baseline 2D method is $m_H = 124.51 \pm 0.52$ GeV. The signal strength at this value for m_H is $\mu = 1.66^{+0.39}_{-0.34}$ (stat) $^{+0.21}_{-0.14}$ (syst). The other methods of Sec. VIII A, 1D and per-event resolution, yield similar results for the Higgs boson mass [9]. Figure 17 shows the best fit values of μ and m_H as well as the profile likelihood ratio contours in the (m_H, μ) plane corresponding to the 68% and 95% confidence level intervals. Finally, the best fit value for m_H obtained using the model developed for the categorized analysis, described in Sec. VIII B, is within 90 MeV of the value found with the inclusive 2D method.

At the combined ATLAS measured value of the Higgs boson mass, $m_H = 125.36$ GeV, the signal strength is found to be $\mu = 1.50^{+0.35}_{-0.31}$ (stat) $^{+0.19}_{-0.13}$ (syst). The scan of the profile likelihood, $-2 \ln \Lambda(\mu)$, as a function of the inclusive signal strength μ for each one of the four channels

separately, as well as for their combination, is shown in Fig. 17(b).

B. Coupling studies

The numbers of expected and observed events in each of the categories described in Sec. V B are summarized in Table XII. The expected yield in each enriched category is given for each of the production modes, where the ggF, $b\bar{b}H$ and $t\bar{t}H$ yields are combined. The expected and observed numbers of events are given for two $m_{4\ell}$ mass ranges: 120–130 GeV and above 110 GeV. Three of the VBF candidates are found in the mass region 120–130 GeV with invariant masses of 123.2, 123.4 and 125.7 GeV. Only one VBF candidate has a BDT_{VBF} output above zero: $m_{4\ell} = 123.4$ GeV and a BDT_{VBF} output value of 0.7. In this mass window, the expected number of VBF candidates with BDT_{VBF} output above zero is 1.26 ± 0.15 , where half of this is expected to be from a true VBF signal, about 35% from ggF production and the rest is mostly from ZZ^* and reducible backgrounds. The distributions of $m_{4\ell}$ and the BDT_{VBF} output for the VBF enriched category in the full mass range and in the fit range of 110–140 GeV are shown in Fig. 18. The signal purity, defined as $S/(S+B)$, as a function of the BDT_{VBF} output is shown in Fig. 19 for Higgs events relative to the backgrounds and for VBF events relative to the other Higgs boson production mechanisms for $110 < m_{4\ell} < 140$ GeV. There is no VH candidate in the 120–130 GeV mass range for either the hadronic or leptonic categories. For the full mass range above 110 GeV all categories are dominated by ZZ^* background, and the observed number of events agrees well with the expectation as can be seen in Table XII.

In the following, measurements of the production strengths and couplings are discussed. They are all

TABLE XII. Expected and observed yields in the VBF enriched, VH-hadronic enriched, VH-leptonic enriched and ggF enriched categories. The yields are given for the different production modes and the ZZ^* and reducible background for 4.6 fb^{-1} at $\sqrt{s} = 7$ TeV and 20.3 fb^{-1} at $\sqrt{s} = 8$ TeV. The estimates are given for both the $m_{4\ell}$ mass range 120–130 GeV and the mass range above 110 GeV.

Enriched category	Signal				Background		Total	
	ggF + $b\bar{b}H + t\bar{t}H$	VBF	VH-hadronic	VH-leptonic	ZZ^*	Z + jets, $t\bar{t}$	expected	Observed
$120 < m_{4\ell} < 130 \text{ GeV}$								
VBF	1.18 ± 0.37	0.75 ± 0.04	0.083 ± 0.006	0.013 ± 0.001	0.17 ± 0.03	0.25 ± 0.14	2.4 ± 0.4	3
($\text{BDT}_{\text{VBF}} > 0$)	0.48 ± 0.15	0.62 ± 0.04	0.023 ± 0.002	0.004 ± 0.001	0.06 ± 0.01	0.10 ± 0.05	1.26 ± 0.15	1
VH-hadronic	0.40 ± 0.12	0.034 ± 0.004	0.20 ± 0.01	0.009 ± 0.001	0.09 ± 0.01	0.09 ± 0.04	0.80 ± 0.12	0
VH-leptonic	0.013 ± 0.002	< 0.001	< 0.001	0.069 ± 0.004	0.015 ± 0.002	0.016 ± 0.019	0.11 ± 0.02	0
ggF	12.8 ± 1.3	0.57 ± 0.02	0.24 ± 0.01	0.11 ± 0.01	7.1 ± 0.2	2.7 ± 0.4	23.5 ± 1.4	34
$m_{4\ell} > 110 \text{ GeV}$								
VBF	1.4 ± 0.4	0.82 ± 0.05	0.092 ± 0.007	0.022 ± 0.002	20 ± 4	1.6 ± 0.9	$24. \pm 4.$	32
($\text{BDT}_{\text{VBF}} > 0$)	0.54 ± 0.17	0.68 ± 0.04	0.025 ± 0.002	0.007 ± 0.001	8.2 ± 1.6	0.6 ± 0.3	10.0 ± 1.6	12
VH-hadronic	0.46 ± 0.14	0.038 ± 0.004	0.23 ± 0.01	0.015 ± 0.001	9.0 ± 1.2	0.6 ± 0.2	10.3 ± 1.2	13
VH-leptonic	0.026 ± 0.004	< 0.002	< 0.002	0.15 ± 0.01	0.63 ± 0.04	0.11 ± 0.14	0.92 ± 0.16	1
ggF	14.1 ± 1.5	0.63 ± 0.02	0.27 ± 0.01	0.17 ± 0.01	$351. \pm 20$	16.6 ± 2.2	$383. \pm 20$	420

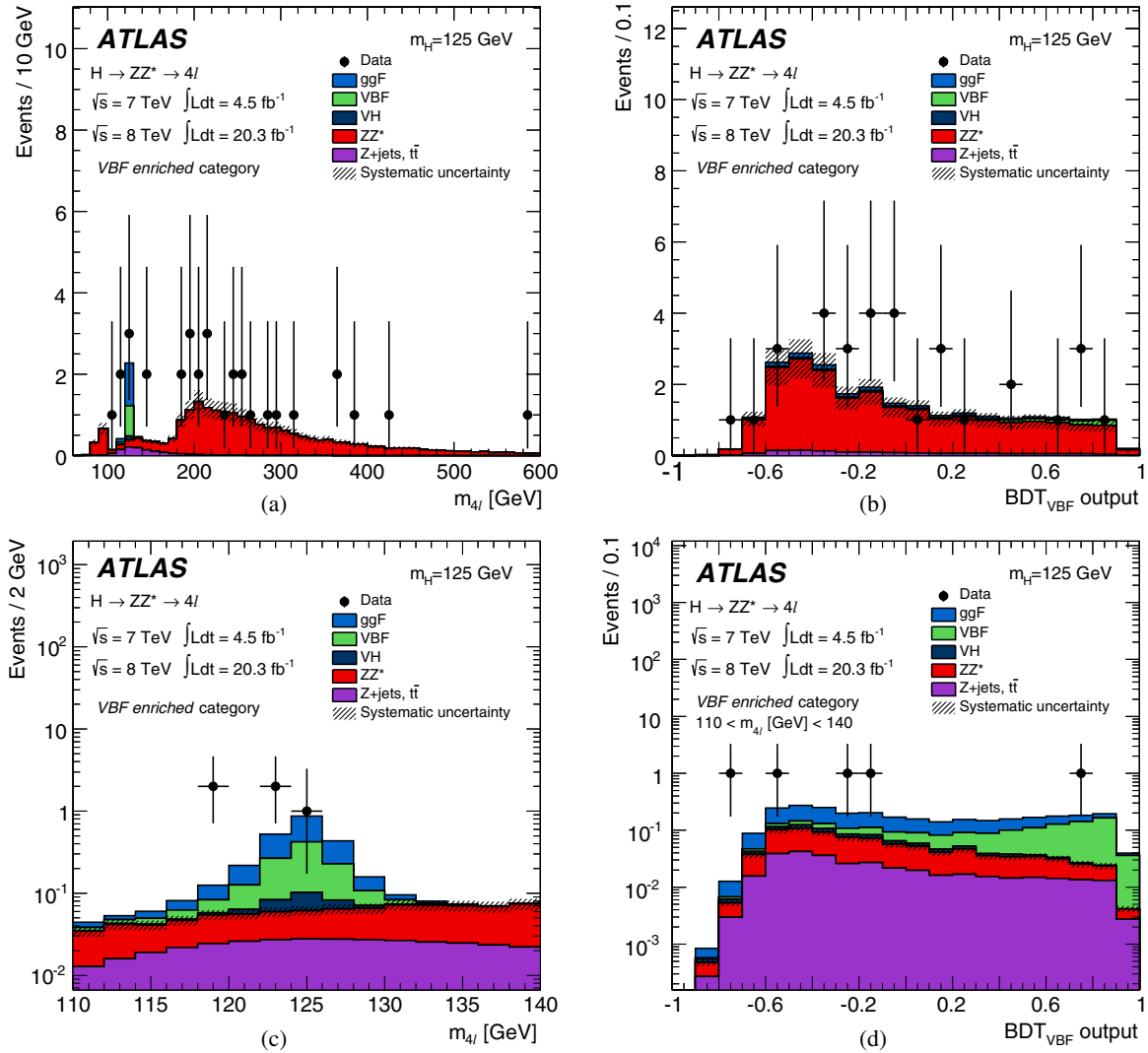


FIG. 18 (color online). Distributions of the selected events and expected signal and background yields for the VBF enriched category for (a) $m_{4\ell}$ and (b) the BDT_{VBF} output in the full mass range, and for (c) $m_{4\ell}$ and (d) the BDT_{VBF} output in the fit mass range $110 < m_{4\ell} < 140$ GeV. The expected Higgs signal contributions, assuming $m_H = 125$ GeV, from the ggF (blue histogram), VBF (green histogram) and VH (dark-blue histogram) production modes are included. The expected background contributions, ZZ^* (red histogram) and $Z + \text{jets} + t\bar{t}$ (violet histogram), are also shown; the systematic uncertainty associated to the total background contribution is represented by the hatched areas. In every case, the combination of the 7 and 8 TeV results is shown.

evaluated assuming the ATLAS combined mass $m_H = 125.36$ GeV. The measurement of a global signal strength factor, discussed in Sec. X A, can be extended to a measurement of the signal strength factors for specific production modes.

The production mechanisms are grouped into the “fermionic” and the “bosonic” ones. The former consists of ggF, $b\bar{b}H$ and $t\bar{t}H$, while the latter includes the VBF and VH modes. In Fig. 20 the best fit value for $\mu_{\text{ggF}+b\bar{b}H+t\bar{t}H} \times B/B_{\text{SM}}$ versus $\mu_{\text{VBF}+\text{VH}} \times B/B_{\text{SM}}$ is presented. The factor B/B_{SM} , the scale factor of the branching ratio with respect to the SM value, is included since with a single channel analysis the source of potential deviations from the SM expectation cannot be resolved between production and

decay. The profile likelihood ratio contours that correspond to the 68% and 95% confidence levels are also shown. The measured values for $\mu_{\text{ggF}+b\bar{b}H+t\bar{t}H} \times B/B_{\text{SM}}$ and $\mu_{\text{VBF}+\text{VH}} \times B/B_{\text{SM}}$ are respectively

$$\begin{aligned} \mu_{\text{ggF}+b\bar{b}H+t\bar{t}H} \times B/B_{\text{SM}} &= 1.66^{+0.45}_{-0.41} (\text{stat})^{+0.25}_{-0.15} (\text{syst}) \\ \mu_{\text{VBF}+\text{VH}} \times B/B_{\text{SM}} &= 0.26^{+1.60}_{-0.91} (\text{stat})^{+0.36}_{-0.23} (\text{syst}). \end{aligned} \quad (6)$$

The rounded results, with statistical and systematic uncertainties combined, are $\mu_{\text{ggF}+b\bar{b}H+t\bar{t}H} \times B/B_{\text{SM}} = 1.7^{+0.5}_{-0.4}$ and $\mu_{\text{VBF}+\text{VH}} \times B/B_{\text{SM}} = 0.3^{+1.6}_{-0.9}$.

The fit to the categories can be constrained to extract a single overall signal strength for the $H \rightarrow ZZ^* \rightarrow 4\ell$ final state.

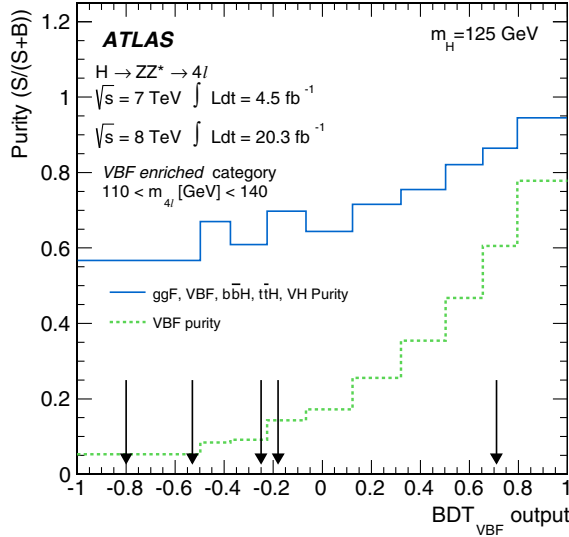


FIG. 19 (color online). Signal purity, defined as $S/(S+B)$, as a function of the BDT_{VBF} output. The solid blue line shows the purity for all Higgs signal production mechanisms relative to the ZZ^* and reducible backgrounds. The dashed green line shows the purity for VBF events relative to the other Higgs boson production mechanisms, for the fit region $110 < m_{4\ell} < 140$ GeV. The binning is chosen so that each bin contains 10% of the total expected signal events. The five VBF candidates observed in data in the signal region are indicated with the black arrows.

This combined $\mu \times B/B_{SM}$ is $1.44^{+0.34}_{-0.31}$ (stat) $^{+0.21}_{-0.11}$ (syst). The ambiguity between production and decay is removed in Fig. 20(b), where the ratio $\mu_{VBF+VH}/\mu_{ggF+b\bar{b}H+t\bar{t}H}$ is presented. The measured value of this ratio is $0.2^{+1.2}_{-0.5}$.

Following the approach and benchmarks recommended by the LHC Higgs Cross Section Working Group [103],

measurements of couplings are implemented using a leading-order tree-level-motivated framework. This framework is based on the following assumptions: (a) the central value of the ATLAS combined mass measurement of $m_H = 125.36$ GeV is assumed; (b) the width of the Higgs boson is narrow, justifying the use of the zero-width approximation; and (c) only modifications of coupling strengths are considered, while the SM tensor structure is assumed, implying that the observed state is a CP -even scalar. The zero-width approximation allows the signal cross section to be decomposed in the following way: $\sigma \cdot B(i \rightarrow H \rightarrow f) = \sigma_i \cdot \Gamma_f / \Gamma_H$ where σ_i is the production cross section through the initial state i ; B and Γ_f are the branching ratio and partial decay width into the final state f , respectively; and Γ_H the total width of the Higgs boson. This approach introduces scale factors applied to the Higgs boson coupling, κ_j , for particle j , which correspond to deviations from the SM Higgs coupling. For example, ggF production of the ZZ^* final state can be represented as $\sigma \cdot B(gg \rightarrow H \rightarrow ZZ^*) = \sigma_{SM}(gg \rightarrow H) \cdot B_{SM}(H \rightarrow ZZ^*) \cdot (\kappa_g^2 \cdot \kappa_Z^2) / \kappa_H^2$, where κ_g , κ_Z , and κ_H are the scale factors for the Higgs couplings to g and Z , and a scale factor for the total Higgs width, respectively. Results are extracted from fits to the data using the profile likelihood ratio $\Lambda(\vec{\kappa})$. In the fit, the κ_j are treated either as parameters of interest or as nuisance parameters, depending on the measurement.

One benchmark model, which simplifies the measurement of possible deviations, groups the κ_j for the electro-weak vector bosons into a single scale factor, κ_V , and defines another coupling scale factor for all fermions, κ_F . The photon- and gluon-loop couplings are derived from the tree-level couplings to the massive gauge bosons and

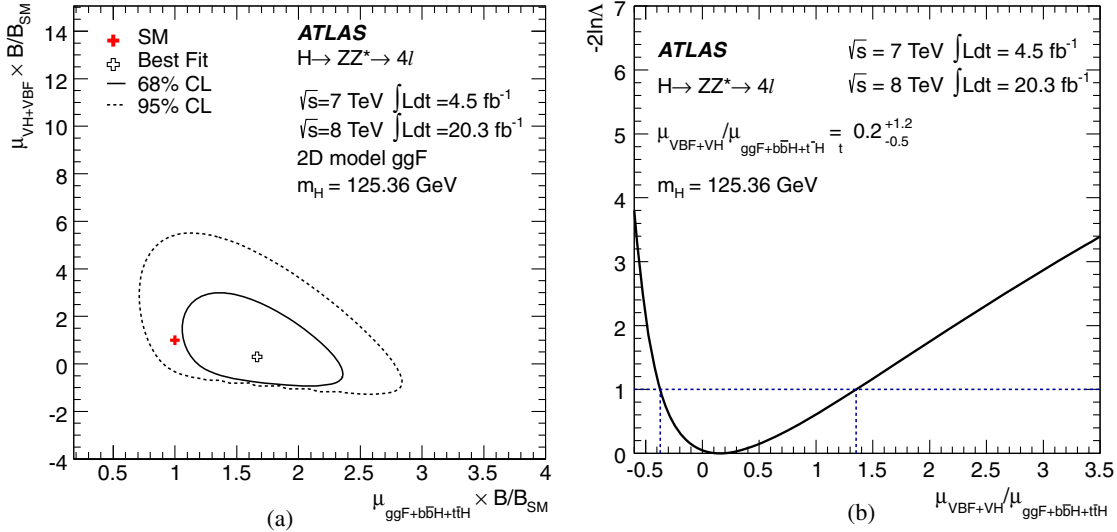


FIG. 20 (color online). (a) Likelihood contours in the $(\mu_{ggF+b\bar{b}H+t\bar{t}H}, \mu_{VBF+VH})$ plane including the branching ratio factor B/B_{SM} . Only the part of the plane where the expected number of signal events in each category is positive is considered. The best fit to the data (open cross) and the 68% CL (solid line) and 95% CL (dashed line) contours are also indicated, as well as the SM expectation (solid red +). (b) Results of a likelihood scan for $\mu_{VBF+VH}/\mu_{ggF+b\bar{b}H+t\bar{t}H}$.

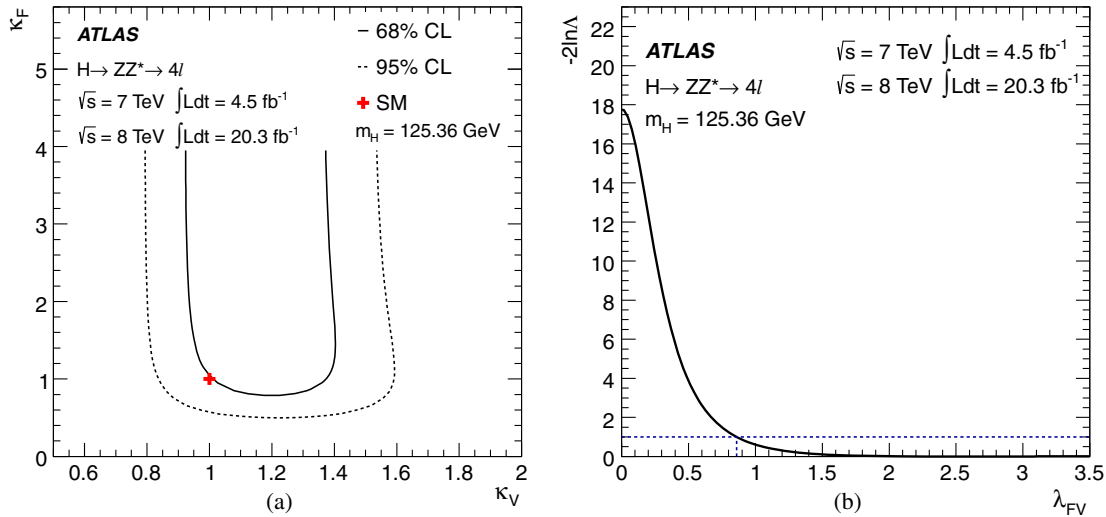


FIG. 21 (color online). (a) Likelihood contours at 68% CL (solid line) and 95% CL (dashed line) in the κ_V - κ_F plane; the SM expectation (solid red cross) is also indicated. (b) Likelihood scan as a function of the ratio $\lambda_{FV} = \kappa_F/\kappa_V$. The Higgs boson mass is assumed to be the ATLAS combined value of $m_H = 125.36 \text{ GeV}$.

fermions, and it is assumed there is no non-SM contribution to the total decay width. The likelihood contours in the κ_V - κ_F plane are shown in Fig. 21. Since κ_V and κ_F are related as $\kappa_F = \kappa_V \times \mu_{\text{ggF}+b\bar{b}H+\bar{t}tH}/\mu_{\text{VBF}+\text{VH}}$, κ_F remains unbounded in Fig. 21 because the present measurement of $\mu_{\text{VBF}+\text{VH}}/\mu_{\text{ggF}+b\bar{b}H+\bar{t}tH}$ cannot exclude the value of zero, as can be seen in Fig. 20(b). The compatibility with the SM expectation is 30%. In Fig. 21(b) the likelihood scan as a function of the ratio of fermion to vector-boson coupling scale factors, $\lambda_{FV} = \kappa_F/\kappa_V$, is presented in the same benchmark model but where no assumption on the total decay width is made; the branching ratio of the Higgs boson to a pair of Z bosons cancels in the ratio. The value $\lambda_{FV} = 0$ is disfavored at the 4σ level.

XI. SUMMARY

The final Run I measurements of the Higgs boson production and couplings in the decay channel $H \rightarrow ZZ^* \rightarrow \ell^+\ell^-\ell^+\ell^-$ are presented. These measurements were performed using pp collision data corresponding to integrated luminosities of 4.5 fb^{-1} and 20.3 fb^{-1} at $\sqrt{s} = 7 \text{ TeV}$ and $\sqrt{s} = 8 \text{ TeV}$, respectively, recorded with the ATLAS detector at the LHC. The signal and background simulation, the electron and muon reconstruction and identification, the event selection and the reducible background estimations are discussed in detail. The analysis was performed both inclusively and with events separated into categories for VBF, VH and ggF production modes. Three multivariate discriminants are employed to improve the separation of the Higgs signal from the ZZ^* background, to separate VBF from ggF Higgs boson production using jet kinematics, and to distinguish hadronic decays of W and Z produced in association with a Higgs from ggF production.

For the inclusive analysis, in the m_H range 120–130 GeV, 37 events are observed while 26.5 ± 1.7 events are expected, decomposed as 16.2 ± 1.6 events for a SM Higgs signal with $m_H = 125 \text{ GeV}$, 7.4 ± 0.4 ZZ^* background events and 2.9 ± 0.3 reducible background events. This excess corresponds to a $H \rightarrow ZZ^* \rightarrow 4\ell$ signal observed (expected) with a significance of 8.1 (6.2) standard deviations at the combined ATLAS measurement of the Higgs boson mass, $m_H = 125.36 \text{ GeV}$ [9].

For the VBF category, one event is seen with a high multivariate discriminant value and a mass of 123.4 GeV. No VH candidate is found in the m_H range 120–130 GeV with the W or Z decaying either hadronically or leptonically. The gluon fusion signal strength is found to be $1.66^{+0.45}_{-0.41}$ (stat) $^{+0.25}_{-0.15}$ (syst) and the signal strength for vector-boson fusion is found to be $0.26^{+1.60}_{-0.91}$ (stat) $^{+0.36}_{-0.23}$ (syst). At the combined ATLAS measurement of the Higgs boson mass, $m_H = 125.36 \text{ GeV}$, the measured combined production rate relative to the SM expectation is $\mu = 1.44^{+0.34}_{-0.31}$ (stat) $^{+0.21}_{-0.11}$ (syst). This measurement is based on a fit to the categories assuming a single overall signal strength. The ratio $\mu_{\text{VBF}+\text{VH}}/\mu_{\text{ggF}+b\bar{b}H+\bar{t}tH}$, which is independent of the $H \rightarrow ZZ^* \rightarrow 4\ell$ branching ratio, is found to be $0.2^{+1.2}_{-0.5}$. Finally, the observed event yields in the categories are used to quantify the compatibility with the SM predictions in terms of the Higgs coupling scale factor for weak vector bosons (κ_V) and fermions (κ_F); they are found to agree with the SM expectations.

The coupling measurements presented here for the Higgs boson decay to four leptons supersede those of the previous ATLAS study [6] and are improved with respect to the earlier results.

ACKNOWLEDGMENTS

We thank CERN for the very successful operation of the LHC, as well as the support staff from our institutions without whom ATLAS could not be operated efficiently. We acknowledge the support of ANPCyT, Argentina; YerPhI, Armenia; ARC, Australia; BMWFW and FWF, Austria; ANAS, Azerbaijan; SSTC, Belarus; CNPq and FAPESP, Brazil; NSERC, NRC and CFI, Canada; CERN; CONICYT, Chile; CAS, MOST and NSFC, China; COLCIENCIAS, Colombia; MSMT CR, MPO CR and VSC CR, Czech Republic; DNRF, DNSRC and Lundbeck Foundation, Denmark; EPLANET, ERC and NSRF, European Union; IN2P3-CNRS, CEA-DSM/IRFU, France; GNSF, Georgia; BMBF, DFG, HGF, MPG and AvH Foundation, Germany; GSRT and NSRF, Greece; ISF, MINERVA, GIF, I-CORE and Benoziyo Center, Israel; INFN, Italy; MEXT and JSPS, Japan; CNRST, Morocco;

FOM and NWO, Netherlands; BRF and RCN, Norway; MNiSW and NCN, Poland; GRICES and FCT, Portugal; MNE/IFA, Romania; MES of Russia and ROSATOM, Russian Federation; JINR; MSTD, Serbia; MSSR, Slovakia; ARRS and MIZŠ, Slovenia; DST/NRF, South Africa; MINECO, Spain; SRC and Wallenberg Foundation, Sweden; SER, SNSF and Cantons of Bern and Geneva, Switzerland; NSC, Taiwan; TAEK, Turkey; STFC, the Royal Society and Leverhulme Trust, United Kingdom; DOE and NSF, United States of America. The crucial computing support from all WLCG partners is acknowledged gratefully, in particular from CERN and the ATLAS Tier-1 facilities at TRIUMF (Canada), NDGF (Denmark, Norway, Sweden), CC-IN2P3 (France), KIT/GridKA (Germany), INFN-CNAF (Italy), NL-T1 (Netherlands), PIC (Spain), ASGC (Taiwan), RAL (UK) and BNL (USA) and in the Tier-2 facilities worldwide.

-
- [1] F. Englert and R. Brout, *Phys. Rev. Lett.* **13**, 321 (1964).
 - [2] P. W. Higgs, *Phys. Rev. Lett.* **13**, 508 (1964).
 - [3] G. S. Guralnik, C. R. Hagen, and T. W. B. Kibble, *Phys. Rev. Lett.* **13**, 585 (1964).
 - [4] ATLAS Collaboration, *Phys. Lett. B* **716**, 1 (2012).
 - [5] CMS Collaboration, *Phys. Lett. B* **716**, 30 (2012).
 - [6] ATLAS Collaboration, *Phys. Lett. B* **726**, 88 (2013).
 - [7] ATLAS Collaboration, *Phys. Lett. B* **726**, 120 (2013).
 - [8] N. Kauer and G. Passarino, *J. High Energy Phys.* 08 (2012) 116.
 - [9] ATLAS Collaboration, *Phys. Rev. D* **90**, 052004 (2014).
 - [10] CMS Collaboration, *Phys. Rev. D* **89**, 092007 (2014).
 - [11] ATLAS Collaboration, *JINST* **3**, S08003 (2008).
 - [12] P. Nason, *J. High Energy Phys.* 11 (2004) 040.
 - [13] S. Frixione, P. Nason, and C. Oleari, *J. High Energy Phys.* **11** (2007) 070.
 - [14] S. Alioli, P. Nason, C. Oleari, and E. Re, *J. High Energy Phys.* **06** (2010) 043.
 - [15] S. Alioli, P. Nason, C. Oleari, and E. Re, *J. High Energy Phys.* **04** (2009) 002.
 - [16] P. Nason and C. Oleari, *J. High Energy Phys.* **02** (2010) 037.
 - [17] D. de Florian, G. Ferrera, M. Grazzini, and D. Tommasini, *J. High Energy Phys.* **06** (2012) 132.
 - [18] M. Grazzini and H. Sargsyan, *J. High Energy Phys.* **09** (2013) 129.
 - [19] E. Bagnaschi, G. Degrassi, P. Slavich, and A. Vicini, *J. High Energy Phys.* **02** (2012) 088.
 - [20] T. Sjostrand, S. Mrenna, and P. Z. Skands, *J. High Energy Phys.* **05** (2006) 026.
 - [21] T. Sjostrand, S. Mrenna, and P. Z. Skands, *Comput. Phys. Commun.* **178**, 852 (2008).
 - [22] P. Golonka and Z. Was, *Eur. Phys. J. C* **45**, 97 (2006).
 - [23] N. Davidson, T. Przedzinski, and Z. Was, arXiv: 1011.0937.
 - [24] LHC Higgs Cross Section Working Group, Report No. CERN-2011-002, edited by S. Dittmaier, C. Mariotti, G. Passarino, and R. Tanaka, 2011.
 - [25] LHC Higgs Cross Section Working Group, Report No. CERN-2012-002, edited by S. Dittmaier, C. Mariotti, G. Passarino, and R. Tanaka, 2012.
 - [26] A. Djouadi, M. Spira, and P. M. Zerwas, *Phys. Lett. B* **264**, 440 (1991).
 - [27] S. Dawson, *Nucl. Phys.* **B359**, 283 (1991).
 - [28] M. Spira, A. Djouadi, D. Graudenz, and P. M. Zerwas, *Nucl. Phys.* **B453**, 17 (1995).
 - [29] R. V. Harlander and W. B. Kilgore, *Phys. Rev. Lett.* **88**, 201801 (2002).
 - [30] C. Anastasiou and K. Melnikov, *Nucl. Phys.* **B646**, 220 (2002).
 - [31] V. Ravindran, J. Smith, and W. L. van Neerven, *Nucl. Phys.* **B665**, 325 (2003).
 - [32] S. Catani, D. de Florian, M. Grazzini, and P. Nason, *J. High Energy Phys.* **07** (2003) 028.
 - [33] U. Aglietti, R. Bonciani, G. Degrassi, and A. Vicini, *Phys. Lett. B* **595**, 432 (2004).
 - [34] S. Actis, G. Passarino, C. Sturm, and S. Uccirati, *Phys. Lett. B* **670**, 12 (2008).
 - [35] D. de Florian and M. Grazzini, *Phys. Lett. B* **718**, 117 (2012).
 - [36] C. Anastasiou, S. Buehler, F. Herzog, and A. Lazopoulos, *J. High Energy Phys.* **04** (2012) 004.
 - [37] J. Baglio and A. Djouadi, *J. High Energy Phys.* **03** (2011) 055.
 - [38] M. Ciccolini, A. Denner, and S. Dittmaier, *Phys. Rev. Lett.* **99**, 161803 (2007).
 - [39] M. Ciccolini, A. Denner, and S. Dittmaier, *Phys. Rev. D* **77**, 013002 (2008).
 - [40] K. Arnold *et al.*, *Comput. Phys. Commun.* **180**, 1661 (2009).

- [41] P. Bolzoni, F. Maltoni, S.-O. Moch, and M. Zaro, *Phys. Rev. Lett.* **105**, 011801 (2010).
- [42] T. Han and S. Willenbrock, *Phys. Lett. B* **273**, 167 (1991).
- [43] O. Brein, A. Djouadi, and R. Harlander, *Phys. Lett. B* **579**, 149 (2004).
- [44] M. L. Ciccolini, S. Dittmaier, and M. Kramer, *Phys. Rev. D* **68**, 073003 (2003).
- [45] W. Beenakker, S. Dittmaier, M. Krämer, B. Plümper, M. Spira, and P. Zerwas, *Phys. Rev. Lett.* **87**, 201805 (2001).
- [46] W. Beenakker, S. Dittmaier, M. Krämer, B. Plümper, M. Spira, and P. Zerwas, *Nucl. Phys.* **B653**, 151 (2003).
- [47] S. Dawson, L. Orr, L. Reina, and D. Wackerth, *Phys. Rev. D* **67**, 071503 (2003).
- [48] S. Dawson, C. Jackson, L. H. Orr, L. Reina, and D. Wackerth, *Phys. Rev. D* **68**, 034022 (2003).
- [49] S. Dawson, C. Jackson, L. Reina, and D. Wackerth, *Phys. Rev. D* **69**, 074027 (2004).
- [50] S. Dittmaier, M. Kramer, and M. Spira, *Phys. Rev. D* **70**, 074010 (2004).
- [51] S. Dawson, C. Jackson, L. Reina, and D. Wackerth, *Mod. Phys. Lett. A* **21**, 89 (2006).
- [52] R. V. Harlander and W. B. Kilgore, *Phys. Rev. D* **68**, 013001 (2003).
- [53] R. Harlander, M. Kramer, and M. Schumacher, [arXiv: 1112.3478](https://arxiv.org/abs/1112.3478).
- [54] A. Bredenstein, A. Denner, S. Dittmaier, and M. M. Weber, *Phys. Rev. D* **74**, 013004 (2006).
- [55] A. Bredenstein, A. Denner, S. Dittmaier, and M. M. Weber, *J. High Energy Phys.* 02 (2007) 080.
- [56] A. Djouadi, J. Kalinowski, and M. Spira, *Comput. Phys. Commun.* **108**, 56 (1998).
- [57] M. Botje *et al.*, [arXiv:1101.0538](https://arxiv.org/abs/1101.0538).
- [58] H.-L. Lai, M. Guzzi, J. Huston, Z. Li, P. M. Nadolsky, J. Pumplin, and C.-P. Yuan, *Phys. Rev. D* **82**, 074024 (2010).
- [59] A. D. Martin, W. J. Stirling, R. S. Thorne, and G. Watt, *Eur. Phys. J. C* **63**, 189 (2009).
- [60] R. D. Ball, V. Bertone, F. Cerutti, L. D. Debbio, S. Forte, A. Guffanti, J. I. Latorre, J. Rojo, and M. Ubiali, *Nucl. Phys.* **B849**, 296 (2011).
- [61] ATLAS and CMS Collaborations, Reports No. ATL-PHYS-PUB-2011-11 and CMS-NOTE-2011-005, 2011.
- [62] T. Melia, P. Nason, R. Rontsch, and G. Zanderighi, *J. High Energy Phys.* **11** (2011) 078.
- [63] T. Binoth, N. Kauer, and P. Mertsch, [arXiv:0807.0024](https://arxiv.org/abs/0807.0024).
- [64] M. L. Mangano, M. Moretti, F. Piccinini, R. Pittau, and A. D. Polosa, *J. High Energy Phys.* 07 (2003) 001.
- [65] M. L. Mangano, M. Moretti, F. Piccinini, and M. Treccani, *J. High Energy Phys.* 01 (2007) 013.
- [66] K. Melnikov and F. Petriello, *Phys. Rev. D* **74**, 114017 (2006).
- [67] C. Anastasiou, L. J. Dixon, K. Melnikov, and F. Petriello, *Phys. Rev. D* **69**, 094008 (2004).
- [68] J. M. Campbell and R. Ellis, *Nucl. Phys. B, Proc. Suppl.* **205–206**, 10 (2010).
- [69] J. M. Campbell and R. K. Ellis, *Phys. Rev. D* **62**, 114012 (2000).
- [70] S. Jadach, Z. Was, R. Decker, and J. H. Kuhn, *Comput. Phys. Commun.* **76**, 361 (1993).
- [71] P. Golonka, B. Kersevan, T. Pierzchała, E. Richter-Wąs, Z. Wąs, and M. Worek, *Comput. Phys. Commun.* **174**, 818 (2006).
- [72] T. Gleisberg, S. Höche, F. Krauss, M. Schönher, S. Schumann, F. Siegert, and J. Winter, *J. High Energy Phys.* 02 (2009) 007.
- [73] ATLAS Collaboration, *Eur. Phys. J. C* **70**, 823 (2010).
- [74] S. Agostinelli *et al.*, *Nucl. Instrum. Methods Phys. Res., Sect. A* **506**, 250 (2003).
- [75] ATLAS Collaboration, *Eur. Phys. J. C* **72**, 1909 (2012).
- [76] ATLAS Collaboration, *Eur. Phys. J. C* **74**, 3071 (2014).
- [77] ATLAS Collaboration, Report No. ATLAS-CONF-2012-047, 2012.
- [78] ATLAS Collaboration, Report No. ATLAS-CONF-2014-032, 2014.
- [79] ATLAS Collaboration, *Eur. Phys. J. C* **74**, 2941 (2014).
- [80] ATLAS Collaboration, Report No. ATLAS-CONF-2013-088, 2013.
- [81] ATLAS Collaboration, *Eur. Phys. J. C* **74**, 3130 (2014).
- [82] ATLAS Collaboration, Report No. ATLAS-CONF-2012-143, 2012.
- [83] ATLAS Collaboration, Report No. ATLAS-CONF-2012-123, 2012.
- [84] M. Cacciari and G. P. Salam, *Phys. Lett. B* **641**, 57 (2006).
- [85] M. Cacciari, G. P. Salam, and G. Soyez, *J. High Energy Phys.* **04** (2008) 063.
- [86] W. Lampl, S. Laplace, D. Lelas, P. Loch, H. Ma, S. Menke, S. Rajagopalan, D. Rousseau, S. Snyder, and G. Unal, Report No. ATL-LARG-PUB-2008-002, 2008.
- [87] ATLAS Collaboration, *Eur. Phys. J. C* **73**, 2304 (2013).
- [88] ATLAS Collaboration, Report No. ATLAS-CONF-2012-064, 2012.
- [89] ATLAS Collaboration, [arXiv:1406.0076](https://arxiv.org/abs/1406.0076).
- [90] ATLAS Collaboration, Report No. ATLAS-CONF-2013-083, 2013.
- [91] M. Cacciari and G. P. Salam, *Phys. Lett. B* **659**, 119 (2008).
- [92] ATLAS Collaboration, Report No. ATLAS-CONF-2013-013, 2013.
- [93] M. Pivk and F. Le Diberder, *Nucl. Instrum. Methods Phys. Res., Sect. A* **555**, 356 (2005).
- [94] ATLAS Collaboration, Report No. ATLAS-CONF-2014-004, 2014.
- [95] P. Speckmayer, A. Höcker, J. Stelzer, and H. Voss, *J. Phys. Conf. Ser.* **219**, 032057 (2010).
- [96] J. Alwall, M. Herquet, F. Maltoni, O. Mattelaer, and T. Stelzer, *J. High Energy Phys.* 06 (2011) 128.
- [97] K. S. Cranmer, *Comput. Phys. Commun.* **136**, 198 (2001).
- [98] L. A. Piegl and W. Tiller, *The NURBS Book: Monographs in Visual Communication*, 2nd ed. (Springer, New York, 1997) Chap. 2.
- [99] ATLAS Collaboration, *Phys. Rev. D* **86**, 032003 (2012).
- [100] G. Cowan, K. Cranmer, E. Gross, and O. Vitells, *Eur. Phys. J. C* **71**, 1554 (2011).

- [101] ATLAS Collaboration, *Eur. Phys. J. C* **73**, 2518 (2013).
 [102] I. W. Stewart and F. J. Tackmann, *Phys. Rev. D* **85**, 034011 (2012).
 [103] LHC Higgs Cross Section Working Group, Report No. CERN-2013-004, edited by S. Heinemeyer, C. Mariotti, G. Passarino, and R. Tanaka, CERN, Geneva, 2013.
 [104] ATLAS Collaboration, *Phys. Rev. Lett.* **112**, 231806 (2014).
 [105] CMS Collaboration, *J. High Energy Phys.* **12** (2012) 034.

- G. Aad,⁸⁵ B. Abbott,¹¹³ J. Abdallah,¹⁵³ S. Abdel Khalek,¹¹⁷ O. Abdinov,¹¹ R. Aben,¹⁰⁷ B. Abi,¹¹⁴ M. Abolins,⁹⁰ O. S. AbouZeid,¹⁶⁰ H. Abramowicz,¹⁵⁵ H. Abreu,¹⁵⁴ R. Abreu,³⁰ Y. Abulaiti,^{148a,148b} B. S. Acharya,^{166a,166b,b} L. Adamczyk,^{38a} D. L. Adams,²⁵ J. Adelman,¹⁷⁸ S. Adomeit,¹⁰⁰ T. Adye,¹³¹ T. Agatonovic-Jovin,^{13a} J. A. Aguilar-Saavedra,^{126a,126f} M. Agustoni,¹⁷ S. P. Ahlen,²² F. Ahmadov,^{65,c} G. Aielli,^{135a,135b} H. Akerstedt,^{148a,148b} T. P. A. Åkesson,⁸¹ G. Akimoto,¹⁵⁷ A. V. Akimov,⁹⁶ G. L. Alberghi,^{20a,20b} J. Albert,¹⁷¹ S. Albrand,⁵⁵ M. J. Alconada Verzini,⁷¹ M. Aleksa,³⁰ I. N. Aleksandrov,⁶⁵ C. Alexa,^{26a} G. Alexander,¹⁵⁵ G. Alexandre,⁴⁹ T. Alexopoulos,¹⁰ M. Alhroob,^{166a,166c} G. Alimonti,^{91a} L. Alio,⁸⁵ J. Alison,³¹ B. M. M. Allbrooke,¹⁸ L. J. Allison,⁷² P. P. Allport,⁷⁴ A. Aloisio,^{104a,104b} A. Alonso,³⁶ F. Alonso,⁷¹ C. Alpigiani,⁷⁶ A. Altheimer,³⁵ B. Alvarez Gonzalez,⁹⁰ M. G. Alvaggi,^{104a,104b} K. Amako,⁶⁶ Y. Amaral Coutinho,^{24a} C. Amelung,²³ D. Amidei,⁸⁹ S. P. Amor Dos Santos,^{126a,126c} A. Amorim,^{126a,126b} S. Amoroso,⁴⁸ N. Amram,¹⁵⁵ G. Amundsen,²³ C. Anastopoulos,¹⁴¹ L. S. Ancu,⁴⁹ N. Andari,³⁰ T. Andeen,³⁵ C. F. Anders,^{58b} G. Anders,³⁰ K. J. Anderson,³¹ A. Andreazza,^{91a,91b} V. Andrei,^{58a} X. S. Anduaga,⁷¹ S. Angelidakis,⁹ I. Angelozzi,¹⁰⁷ P. Anger,⁴⁴ A. Angerami,³⁵ F. Anghinolfi,³⁰ A. V. Anisenkov,^{109,d} N. Anjos,¹² A. Annovi,⁴⁷ A. Antonaki,⁹ M. Antonelli,⁴⁷ A. Antonov,⁹⁸ J. Antos,^{146b} F. Anulli,^{134a} M. Aoki,⁶⁶ L. Aperio Bella,¹⁸ R. Apolle,^{120,e} G. Arabidze,⁹⁰ I. Aracena,¹⁴⁵ Y. Arai,⁶⁶ J. P. Araque,^{126a} A. T. H. Arce,⁴⁵ J.-F. Arguin,⁹⁵ S. Argyropoulos,⁴² M. Arik,^{19a} A. J. Armbruster,³⁰ O. Arnaez,³⁰ V. Arnal,⁸² H. Arnold,⁴⁸ M. Arratia,²⁸ O. Arslan,²¹ A. Artamonov,⁹⁷ G. Artoni,²³ S. Asai,¹⁵⁷ N. Asbah,⁴² A. Ashkenazi,¹⁵⁵ B. Åsman,^{148a,148b} L. Asquith,⁶ K. Assamagan,²⁵ R. Astalos,^{146a} M. Atkinson,¹⁶⁷ N. B. Atlay,¹⁴³ B. Auerbach,⁶ K. Augsten,¹²⁸ M. Auroousseau,^{147b} G. Avolio,³⁰ G. Azuelos,^{95,f} Y. Azuma,¹⁵⁷ M. A. Baak,³⁰ A. E. Baas,^{58a} C. Bacci,^{136a,136b} H. Bachacou,¹³⁸ K. Bachas,¹⁵⁶ M. Backes,³⁰ M. Backhaus,³⁰ J. Backus Mayes,¹⁴⁵ E. Badescu,^{26a} P. Bagiacchi,^{134a,134b} P. Bagnaia,^{134a,134b} Y. Bai,^{33a} T. Bain,³⁵ J. T. Baines,¹³¹ O. K. Baker,¹⁷⁸ P. Balek,¹²⁹ F. Balli,¹³⁸ E. Banas,³⁹ Sw. Banerjee,¹⁷⁵ A. A. E. Bannoura,¹⁷⁷ V. Bansal,¹⁷¹ H. S. Bansil,¹⁸ L. Barak,¹⁷⁴ S. P. Baranov,⁹⁶ E. L. Barberio,⁸⁸ D. Barberis,^{50a,50b} M. Barbero,⁸⁵ T. Barilliari,¹⁰¹ M. Barisonzi,¹⁷⁷ T. Barklow,¹⁴⁵ N. Barlow,²⁸ B. M. Barnett,¹³¹ R. M. Barnett,¹⁵ Z. Barnovska,⁵ A. Baroncelli,^{136a} G. Barone,⁴⁹ A. J. Barr,¹²⁰ F. Barreiro,⁸² J. Barreiro Guimarães da Costa,⁵⁷ R. Bartoldus,¹⁴⁵ A. E. Barton,⁷² P. Bartos,^{146a} V. Bartsch,¹⁵¹ A. Bassalat,¹¹⁷ A. Basye,¹⁶⁷ R. L. Bates,⁵³ J. R. Batley,²⁸ M. Battaglia,¹³⁹ M. Battistin,³⁰ F. Bauer,¹³⁸ H. S. Bawa,^{145,g} M. D. Beattie,⁷² T. Beau,⁸⁰ P. H. Beauchemin,¹⁶³ R. Beccerle,^{124a,124b} P. Bechtle,²¹ H. P. Beck,¹⁷ K. Becker,¹⁷⁷ S. Becker,¹⁰⁰ M. Beckingham,¹⁷² C. Becot,¹¹⁷ A. J. Beddall,^{19c} A. Beddall,^{19c} S. Bedikian,¹⁷⁸ V. A. Bednyakov,⁶⁵ C. P. Bee,¹⁵⁰ L. J. Beemster,¹⁰⁷ T. A. Beermann,¹⁷⁷ M. Begel,²⁵ K. Behr,¹²⁰ C. Belanger-Champagne,⁸⁷ P. J. Bell,⁴⁹ W. H. Bell,⁴⁹ G. Bella,¹⁵⁵ L. Bellagamba,^{20a} A. Bellerive,²⁹ M. Bellomo,⁸⁶ K. Belotskiy,⁹⁸ O. Beltramo,³⁰ O. Benary,¹⁵⁵ D. Benchekroun,^{137a} K. Bendtz,^{148a,148b} N. Benekos,¹⁶⁷ Y. Benhammou,¹⁵⁵ E. Benhar Noccioli,⁴⁹ J. A. Benitez Garcia,^{161b} D. P. Benjamin,⁴⁵ J. R. Bensinger,²³ K. Benslama,¹³² S. Bentvelsen,¹⁰⁷ D. Berge,¹⁰⁷ E. Bergeaas Kuutmann,¹⁶⁸ N. Berger,⁵ F. Berghaus,¹⁷¹ J. Beringer,¹⁵ C. Bernard,²² P. Bernat,⁷⁸ C. Bernius,⁷⁹ F. U. Bernlochner,¹⁷¹ T. Berry,⁷⁷ P. Berta,¹²⁹ C. Bertella,⁸⁵ G. Bertoli,^{148a,148b} F. Bertolucci,^{124a,124b} C. Bertsche,¹¹³ D. Bertsche,¹¹³ M. I. Besana,^{91a} G. J. Besjes,¹⁰⁶ O. Bessidskaia,^{148a,148b} M. Bessner,⁴² N. Besson,¹³⁸ C. Betancourt,⁴⁸ S. Bethke,¹⁰¹ W. Bhimji,⁴⁶ R. M. Bianchi,¹²⁵ L. Bianchini,²³ M. Bianco,³⁰ O. Biebel,¹⁰⁰ S. P. Bieniek,⁷⁸ K. Bierwagen,⁵⁴ J. Biesiada,¹⁵ M. Biglietti,^{136a} J. Bilbao De Mendizabal,⁴⁹ H. Bilokon,⁴⁷ M. Bindl,⁵⁴ S. Binet,¹¹⁷ A. Bingul,^{19c} C. Bini,^{134a,134b} C. W. Black,¹⁵² J. E. Black,¹⁴⁵ K. M. Black,²² D. Blackburn,¹⁴⁰ R. E. Blair,⁶ J.-B. Blanchard,¹³⁸ T. Blazek,^{146a} I. Bloch,⁴² C. Blocker,²³ W. Blum,^{83,a} U. Blumenschein,⁵⁴ G. J. Bobbink,¹⁰⁷ V. S. Bobrovnikov,^{109,d} S. S. Bocchetta,⁸¹ A. Bocci,⁴⁵ C. Bock,¹⁰⁰ C. R. Boddy,¹²⁰ M. Boehler,⁴⁸ T. T. Boek,¹⁷⁷ J. A. Bogaerts,³⁰ A. G. Bogdanchikov,¹⁰⁹ A. Bogouch,^{92,a} C. Bohm,^{148a} J. Bohm,¹²⁷ V. Boisvert,⁷⁷ T. Bold,^{38a} V. Boldea,^{26a} A. S. Boldyrev,⁹⁹ M. Bomben,⁸⁰ M. Bona,⁷⁶ M. Boonekamp,¹³⁸ A. Borisov,¹³⁰ G. Borissov,⁷² M. Borri,⁸⁴ S. Borroni,⁴² J. Bortfeldt,¹⁰⁰ V. Bortolotto,^{136a,136b} K. Bos,¹⁰⁷ D. Boscherini,^{20a} M. Bosman,¹² H. Boterenbrood,¹⁰⁷ J. Boudreau,¹²⁵ J. Bouffard,² E. V. Bouhova-Thacker,⁷² D. Boumediene,³⁴ C. Bourdarios,¹¹⁷ N. Bousson,¹¹⁴ S. Boutouil,^{137d} A. Boveia,³¹ J. Boyd,³⁰ I. R. Boyko,⁶⁵ I. Bozic,^{13a} J. Bracinik,¹⁸ A. Brandt,⁸ G. Brandt,¹⁵ O. Brandt,^{58a} U. Bratzler,¹⁵⁸ B. Brau,⁸⁶ J. E. Brau,¹¹⁶ H. M. Braun,^{177,a}

- S. F. Brazzale,^{166a,166c} B. Brelier,¹⁶⁰ K. Brendlinger,¹²² A. J. Brennan,⁸⁸ R. Brenner,¹⁶⁸ S. Bressler,¹⁷⁴ K. Bristow,^{147c}
 T. M. Bristow,⁴⁶ D. Britton,⁵³ F. M. Brochu,²⁸ I. Brock,²¹ R. Brock,⁹⁰ C. Bromberg,⁹⁰ J. Bronner,¹⁰¹ G. Brooijmans,³⁵
 T. Brooks,⁷⁷ W. K. Brooks,^{32b} J. Brosamer,¹⁵ E. Brost,¹¹⁶ J. Brown,⁵⁵ P. A. Bruckman de Renstrom,³⁹ D. Bruncko,^{146b}
 R. Bruneliere,⁴⁸ S. Brunet,⁶¹ A. Bruni,^{20a} G. Bruni,^{20a} M. Bruschi,^{20a} L. Bryngemark,⁸¹ T. Buanes,¹⁴ Q. Buat,¹⁴⁴ F. Bucci,⁴⁹
 P. Buchholz,¹⁴³ R. M. Buckingham,¹²⁰ A. G. Buckley,⁵³ S. I. Buda,^{26a} I. A. Budagov,⁶⁵ F. Buehrer,⁴⁸ L. Bugge,¹¹⁹
 M. K. Bugge,¹¹⁹ O. Bulekov,⁹⁸ A. C. Bundock,⁷⁴ H. Burckhart,³⁰ S. Burdin,⁷⁴ B. Burghgrave,¹⁰⁸ S. Burke,¹³¹
 I. Burmeister,⁴³ E. Busato,³⁴ D. Büscher,⁴⁸ V. Büscher,⁸³ P. Bussey,⁵³ C. P. Buszello,¹⁶⁸ B. Butler,⁵⁷ J. M. Butler,²²
 A. I. Butt,³ C. M. Buttar,⁵³ J. M. Butterworth,⁷⁸ P. Butti,¹⁰⁷ W. Buttinger,²⁸ A. Buzatu,⁵³ M. Byszewski,¹⁰
 S. Cabrera Urbán,¹⁶⁹ D. Caforio,^{20a,20b} O. Cakir,^{4a} P. Calafiura,¹⁵ A. Calandri,¹³⁸ G. Calderini,⁸⁰ P. Calfayan,¹⁰⁰
 R. Calkins,¹⁰⁸ L. P. Caloba,^{24a} D. Calvet,³⁴ S. Calvet,³⁴ R. Camacho Toro,⁴⁹ S. Camarda,⁴² D. Cameron,¹¹⁹
 L. M. Caminada,¹⁵ R. Caminal Armadans,¹² S. Campana,³⁰ M. Campanelli,⁷⁸ A. Campoverde,¹⁵⁰ V. Canale,^{104a,104b}
 A. Canepa,^{161a} M. Cano Bret,⁷⁶ J. Cantero,⁸² R. Cantrill,^{126a} T. Cao,⁴⁰ M. D. M. Capeans Garrido,³⁰ I. Caprini,^{26a}
 M. Caprini,^{26a} M. Capua,^{37a,37b} R. Caputo,⁸³ R. Cardarelli,^{135a} T. Carli,³⁰ G. Carlino,^{104a} L. Carminati,^{91a,91b} S. Caron,¹⁰⁶
 E. Carquin,^{32a} G. D. Carrillo-Montoya,^{147c} J. R. Carter,²⁸ J. Carvalho,^{126a,126c} D. Casadei,⁷⁸ M. P. Casado,¹² M. Casolino,¹²
 E. Castaneda-Miranda,^{147b} A. Castelli,¹⁰⁷ V. Castillo Gimenez,¹⁶⁹ N. F. Castro,^{126a} P. Catastini,⁵⁷ A. Catinaccio,³⁰
 J. R. Catmore,¹¹⁹ A. Cattai,³⁰ G. Cattani,^{135a,135b} J. Caudron,⁸³ V. Cavalieri,¹⁶⁷ D. Cavalli,^{91a} M. Cavalli-Sforza,¹²
 V. Cavasinni,^{124a,124b} F. Ceradini,^{136a,136b} B. C. Cerio,⁴⁵ K. Cerny,¹²⁹ A. S. Cerqueira,^{24b} A. Cerri,¹⁵¹ L. Cerrito,⁷⁶ F. Cerutti,¹⁵
 M. Cerv,³⁰ A. Cervelli,¹⁷ S. A. Cetin,^{19b} A. Chafaq,^{137a} D. Chakraborty,¹⁰⁸ I. Chalupkova,¹²⁹ P. Chang,¹⁶⁷ B. Chapleau,⁸⁷
 J. D. Chapman,²⁸ D. Charfeddine,¹¹⁷ D. G. Charlton,¹⁸ C. C. Chau,¹⁶⁰ C. A. Chavez Barajas,¹⁵¹ S. Cheatham,⁸⁷
 A. Chegwidden,⁹⁰ S. Chekanov,⁶ S. V. Chekulaev,^{161a} G. A. Chelkov,^{65,h} M. A. Chelstowska,⁸⁹ C. Chen,⁶⁴ H. Chen,²⁵
 K. Chen,¹⁵⁰ L. Chen,^{33d,i} S. Chen,^{33c} X. Chen,^{33f} Y. Chen,⁶⁷ Y. Chen,³⁵ H. C. Cheng,⁸⁹ Y. Cheng,³¹ A. Cheplakov,⁶⁵
 R. Cherkaoui El Moursli,^{137e} V. Chernyatin,^{25,a} E. Cheu,⁷ L. Chevalier,¹³⁸ V. Chiarella,⁴⁷ G. Chiefari,^{104a,104b} J. T. Childers,⁶
 A. Chilingarov,⁷² G. Chiodini,^{73a} A. S. Chisholm,¹⁸ R. T. Chislett,⁷⁸ A. Chitan,^{26a} M. V. Chizhov,⁶⁵ S. Chouridou,⁹
 B. K. B. Chow,¹⁰⁰ D. Chromek-Burckhart,³⁰ M. L. Chu,¹⁵³ J. Chudoba,¹²⁷ J. J. Chwastowski,³⁹ L. Chytka,¹¹⁵
 G. Ciapetti,^{134a,134b} A. K. Ciftci,^{4a} R. Ciftci,^{4a} D. Cinca,⁵³ V. Cindro,⁷⁵ A. Ciocio,¹⁵ P. Cirkovic,^{13b} Z. H. Citron,¹⁷⁴
 M. Citterio,^{91a} M. Ciubancan,^{26a} A. Clark,⁴⁹ P. J. Clark,⁴⁶ R. N. Clarke,¹⁵ W. Cleland,¹²⁵ J. C. Clemens,⁸⁵ C. Clement,^{148a,148b}
 Y. Coadou,⁸⁵ M. Cobal,^{166a,166c} A. Coccaro,¹⁴⁰ J. Cochran,⁶⁴ L. Coffey,²³ J. G. Cogan,¹⁴⁵ J. Coggeshall,¹⁶⁷ B. Cole,³⁵
 S. Cole,¹⁰⁸ A. P. Colijn,¹⁰⁷ J. Collot,⁵⁵ T. Colombo,^{58c} G. Colon,⁸⁶ G. Compostella,¹⁰¹ P. Conde Muiño,^{126a,126b}
 E. Coniavitis,⁴⁸ M. C. Conidi,¹² S. H. Connell,^{147b} I. A. Connelly,⁷⁷ S. M. Consonni,^{91a,91b} V. Consorti,⁴⁸
 S. Constantinescu,^{26a} C. Conta,^{121a,121b} G. Conti,⁵⁷ F. Conventi,^{104a,j} M. Cooke,¹⁵ B. D. Cooper,⁷⁸ A. M. Cooper-Sarkar,¹²⁰
 N. J. Cooper-Smith,⁷⁷ K. Copic,¹⁵ T. Cornelissen,¹⁷⁷ M. Corradi,^{20a} F. Corriveau,^{87,k} A. Corso-Radu,¹⁶⁵
 A. Cortes-Gonzalez,¹² G. Cortiana,¹⁰¹ G. Costa,^{91a} M. J. Costa,¹⁶⁹ D. Costanzo,¹⁴¹ D. Côté,⁸ G. Cottin,²⁸ G. Cowan,⁷⁷
 B. E. Cox,⁸⁴ K. Cranmer,¹¹⁰ G. Cree,²⁹ S. Crépé-Renaudin,⁵⁵ F. Crescioli,⁸⁰ W. A. Cribbs,^{148a,148b} M. Crispin Ortuzar,¹²⁰
 M. Cristinziani,²¹ V. Croft,¹⁰⁶ G. Crosetti,^{37a,37b} C.-M. Cuciuc,^{26a} T. Cuhadar Donszelmann,¹⁴¹ J. Cummings,¹⁷⁸
 M. Curatolo,⁴⁷ C. Cuthbert,¹⁵² H. Czirr,¹⁴³ P. Czodrowski,³ Z. Czyczula,¹⁷⁸ S. D'Auria,⁵³ M. D'Onofrio,⁷⁴
 M. J. Da Cunha Sargedas De Sousa,^{126a,126b} C. Da Via,⁸⁴ W. Dabrowski,^{38a} A. Dafinca,¹²⁰ T. Dai,⁸⁹ O. Dale,¹⁴ F. Dallaire,⁹⁵
 C. Dallapiccola,⁸⁶ M. Dam,³⁶ A. C. Daniells,¹⁸ M. Dano Hoffmann,¹³⁸ V. Dao,⁴⁸ G. Darbo,^{50a} S. Darmora,⁸
 J. A. Dassoulas,⁴² A. DattaGupta,⁶¹ W. Davey,²¹ C. David,¹⁷¹ T. Davidek,¹²⁹ E. Davies,^{120,e} M. Davies,¹⁵⁵ O. Davignon,⁸⁰
 A. R. Davison,⁷⁸ P. Davison,⁷⁸ Y. Davygora,^{58a} E. Dawe,¹⁴⁴ I. Dawson,¹⁴¹ R. K. Daya-Ishmukhametova,⁸⁶ K. De,⁸
 R. de Asmundis,^{104a} S. De Castro,^{20a,20b} S. De Cecco,⁸⁰ N. De Groot,¹⁰⁶ P. de Jong,¹⁰⁷ H. De la Torre,⁸² F. De Lorenzi,⁶⁴
 L. De Nooij,¹⁰⁷ D. De Pedis,^{134a} A. De Salvo,^{134a} U. De Sanctis,¹⁵¹ A. De Santo,¹⁵¹ J. B. De Vivie De Regie,¹¹⁷
 W. J. Dearnaley,⁷² R. Debbe,²⁵ C. Debenedetti,¹³⁹ B. Dechenaux,⁵⁵ D. V. Dedovich,⁶⁵ I. Deigaard,¹⁰⁷ J. Del Peso,⁸²
 T. Del Prete,^{124a,124b} F. Deliot,¹³⁸ C. M. Delitzsch,⁴⁹ M. Deliyergiyev,⁷⁵ A. Dell'Acqua,³⁰ L. Dell'Asta,²²
 M. Dell'Orso,^{124a,124b} M. Della Pietra,^{104a,j} D. della Volpe,⁴⁹ M. Delmastro,⁵ P. A. Delsart,⁵⁵ C. Deluca,¹⁰⁷ S. Demers,¹⁷⁸
 M. Demichev,⁶⁵ A. Demilly,⁸⁰ S. P. Denisov,¹³⁰ D. Derendarz,³⁹ J. E. Derkaoui,^{137d} F. Derue,⁸⁰ P. Dervan,⁷⁴ K. Desch,²¹
 C. Deterre,⁴² P. O. Deviveiros,¹⁰⁷ A. Dewhurst,¹³¹ S. Dhaliwal,¹⁰⁷ A. Di Ciaccio,^{135a,135b} L. Di Ciaccio,⁵
 A. Di Domenico,^{134a,134b} C. Di Donato,^{104a,104b} A. Di Girolamo,³⁰ B. Di Girolamo,³⁰ A. Di Mattia,¹⁵⁴ B. Di Micco,^{136a,136b}
 R. Di Nardo,⁴⁷ A. Di Simone,⁴⁸ R. Di Sipio,^{20a,20b} D. Di Valentino,²⁹ F. A. Dias,⁴⁶ M. A. Diaz,^{32a} E. B. Diehl,⁸⁹ J. Dietrich,⁴²
 T. A. Dietzschi,^{58a} S. Diglio,⁸⁵ A. Dimitrijevska,^{13a} J. Dingfelder,²¹ C. Dionisi,^{134a,134b} P. Dita,^{26a} S. Dita,^{26a} F. Dittus,³⁰

- F. Djama,⁸⁵ T. Djobava,^{51b} J. I. Djuvsland,^{58a} M. A. B. do Vale,^{24c} A. Do Valle Wemans,^{126a,126g} D. Dobos,³⁰ C. Doglioni,⁴⁹ T. Doherty,⁵³ T. Dohmae,¹⁵⁷ J. Dolejsi,¹²⁹ Z. Dolezal,¹²⁹ B. A. Dolgoshein,^{98,a} M. Donadelli,^{24d} S. Donati,^{124a,124b} P. Dondero,^{121a,121b} J. Donini,³⁴ J. Dopke,¹³¹ A. Doria,^{104a} M. T. Dova,⁷¹ A. T. Doyle,⁵³ M. Dris,¹⁰ J. Dubbert,⁸⁹ S. Dube,¹⁵ E. Dubreuil,³⁴ E. Duchovni,¹⁷⁴ G. Duckeck,¹⁰⁰ O. A. Ducu,^{26a} D. Duda,¹⁷⁷ A. Dudarev,³⁰ F. Dudziak,⁶⁴ L. Duflot,¹¹⁷ L. Duguid,⁷⁷ M. Dührssen,³⁰ M. Dunford,^{58a} H. Duran Yildiz,^{4a} M. Düren,⁵² A. Durglishvili,^{51b} M. Dwuznik,^{38a} M. Dyndal,^{38a} J. Ebke,¹⁰⁰ W. Edson,² N. C. Edwards,⁴⁶ W. Ehrenfeld,²¹ T. Eifert,¹⁴⁵ G. Eigen,¹⁴ K. Einsweiler,¹⁵ T. Ekelof,¹⁶⁸ M. El Kacimi,^{137c} M. Ellert,¹⁶⁸ S. Elles,⁵ F. Ellinghaus,⁸³ N. Ellis,³⁰ J. Elmsheuser,¹⁰⁰ M. Elsing,³⁰ D. Emeliyanov,¹³¹ Y. Enari,¹⁵⁷ O. C. Endner,⁸³ M. Endo,¹¹⁸ R. Engelmann,¹⁵⁰ J. Erdmann,¹⁷⁸ A. Ereditato,¹⁷ D. Eriksson,^{148a} G. Ernis,¹⁷⁷ J. Ernst,² M. Ernst,²⁵ J. Ernwein,¹³⁸ D. Errede,¹⁶⁷ S. Errede,¹⁶⁷ E. Ertel,⁸³ M. Escalier,¹¹⁷ H. Esch,⁴³ C. Escobar,¹²⁵ B. Esposito,⁴⁷ A. I. Etienne,¹³⁸ E. Etzion,¹⁵⁵ H. Evans,⁶¹ A. Ezhilov,¹²³ L. Fabbri,^{20a,20b} G. Facini,³¹ R. M. Fakhruddinov,¹³⁰ S. Falciano,^{134a} R. J. Falla,⁷⁸ J. Faltova,¹²⁹ Y. Fang,^{33a} M. Fanti,^{91a,91b} A. Farbin,⁸ A. Farilla,^{136a} T. Farooque,¹² S. Farrell,¹⁵ S. M. Farrington,¹⁷² P. Farthouat,³⁰ F. Fassi,^{137e} P. Fassnacht,³⁰ D. Fassouliotis,⁹ A. Favareto,^{50a,50b} L. Fayard,¹¹⁷ P. Federic,^{146a} O. L. Fedin,^{123,l} W. Fedorko,¹⁷⁰ M. Fehling-Kaschek,⁴⁸ S. Feigl,³⁰ L. Feligioni,⁸⁵ C. Feng,^{33d} E. J. Feng,⁶ H. Feng,⁸⁹ A. B. Fenyuk,¹³⁰ S. Fernandez Perez,³⁰ S. Ferrag,⁵³ J. Ferrando,¹⁶⁸ A. Ferrari,¹⁶⁸ P. Ferrari,¹⁰⁷ R. Ferrari,^{121a} D. E. Ferreira de Lima,⁵³ A. Ferrer,¹⁶⁹ D. Ferrere,⁴⁹ C. Ferretti,⁸⁹ A. Ferretto Parodi,^{50a,50b} M. Fiascaris,³¹ F. Fiedler,⁸³ A. Filipčič,⁷⁵ M. Filipuzzi,⁴² F. Filthaut,¹⁰⁶ M. Fincke-Keeler,¹⁷¹ K. D. Finelli,¹⁵² M. C. N. Fiolhais,^{126a,126c} L. Fiorini,¹⁶⁹ A. Firan,⁴⁰ A. Fischer,² J. Fischer,¹⁷⁷ W. C. Fisher,⁹⁰ E. A. Fitzgerald,²³ M. Flechl,⁴⁸ I. Fleck,¹⁴³ P. Fleischmann,⁸⁹ S. Fleischmann,¹⁷⁷ G. T. Fletcher,¹⁴¹ G. Fletcher,⁷⁶ T. Flick,¹⁷⁷ A. Floderus,⁸¹ L. R. Flores Castillo,^{60a} A. C. Florez Bustos,^{161b} M. J. Flowerdew,¹⁰¹ A. Formica,¹³⁸ A. Forti,⁸⁴ D. Fortin,^{161a} D. Fournier,¹¹⁷ H. Fox,⁷² S. Fracchia,¹² P. Francavilla,⁸⁰ M. Franchini,^{20a,20b} S. Franchino,³⁰ D. Francis,³⁰ L. Franconi,¹¹⁹ M. Franklin,⁵⁷ S. Franz,⁶² M. Fraternali,^{121a,121b} S. T. French,²⁸ C. Friedrich,⁴² F. Friedrich,⁴⁴ D. Froidevaux,³⁰ J. A. Frost,²⁸ C. Fukunaga,¹⁵⁸ E. Fullana Torregrosa,⁸³ B. G. Fulsom,¹⁴⁵ J. Fuster,¹⁶⁹ C. Gabaldon,⁵⁵ O. Gabizon,¹⁷⁷ A. Gabrielli,^{20a,20b} A. Gabrielli,^{134a,134b} S. Gadatsch,¹⁰⁷ S. Gadomski,⁴⁹ G. Gagliardi,^{50a,50b} P. Gagnon,⁶¹ C. Galea,¹⁰⁶ B. Galhardo,^{126a,126c} E. J. Gallas,¹²⁰ V. Gallo,¹⁷ B. J. Gallop,¹³¹ P. Gallus,¹²⁸ G. Galster,³⁶ K. K. Gan,¹¹¹ J. Gao,^{33b,i} Y. S. Gao,^{145,g} F. M. Garay Walls,⁴⁶ F. Garberson,¹⁷⁸ C. García,¹⁶⁹ J. E. García Navarro,¹⁶⁹ M. Garcia-Sciveres,¹⁵ R. W. Gardner,³¹ N. Garelli,¹⁴⁵ V. Garonne,³⁰ C. Gatti,⁴⁷ G. Gaudio,^{121a} B. Gaur,¹⁴³ L. Gauthier,⁹⁵ P. Gauzzi,^{134a,134b} I. L. Gavrilenko,⁹⁶ C. Gay,¹⁷⁰ G. Gaycken,²¹ E. N. Gazis,¹⁰ P. Ge,^{33d} Z. Gecse,¹⁷⁰ C. N. P. Gee,¹³¹ D. A. A. Geerts,¹⁰⁷ Ch. Geich-Gimbel,²¹ K. Gellerstedt,^{148a,148b} C. Gemme,^{50a} A. Gemmell,⁵³ M. H. Genest,⁵⁵ S. Gentile,^{134a,134b} M. George,⁵⁴ S. George,⁷⁷ D. Gerbaudo,¹⁶⁵ A. Gershon,¹⁵⁵ H. Ghazlane,^{137b} N. Ghodbane,³⁴ B. Giacobbe,^{20a} S. Giagu,^{134a,134b} V. Giangiobbe,¹² P. Giannetti,^{124a,124b} F. Gianotti,³⁰ B. Gibbard,²⁵ S. M. Gibson,⁷⁷ M. Gilchriese,¹⁵ T. P. S. Gillam,²⁸ D. Gillberg,³⁰ G. Gilles,³⁴ D. M. Gingrich,^{3,f} N. Giokaris,⁹ M. P. Giordani,^{166a,166c} R. Giordano,^{104a,104b} F. M. Giorgi,¹⁶ P. F. Giraud,¹³⁸ D. Giugni,^{91a} C. Giuliani,⁴⁸ M. Giulini,^{58b} B. K. Gjelsten,¹¹⁹ S. Gkaitatzis,¹⁵⁶ I. Gkalias,^{156,m} L. K. Gladilin,⁹⁹ C. Glasman,⁸² J. Glatzer,³⁰ P. C. F. Glaysher,⁴⁶ A. Glazov,⁴² G. L. Glonti,⁶⁵ M. Goblirsch-Kolb,¹⁰¹ J. R. Goddard,⁷⁶ J. Godlewski,³⁰ C. Goeringer,⁸³ S. Goldfarb,⁸⁹ T. Golling,¹⁷⁸ D. Golubkov,¹³⁰ A. Gomes,^{126a,126b,126d} L. S. Gomez Fajardo,⁴² R. Gonçalo,^{126a} J. Goncalves Pinto Firmino Da Costa,¹³⁸ L. Gonella,²¹ S. González de la Hoz,¹⁶⁹ G. Gonzalez Parra,¹² S. Gonzalez-Sevilla,⁴⁹ L. Goossens,³⁰ P. A. Gorbounov,⁹⁷ H. A. Gordon,²⁵ I. Gorelov,¹⁰⁵ B. Gorini,³⁰ E. Gorini,^{73a,73b} A. Gorišek,⁷⁵ E. Gornicki,³⁹ A. T. Goshaw,⁶ C. Gössling,⁴³ M. I. Gostkin,⁶⁵ M. Gouighri,^{137a} D. Goujdami,^{137c} M. P. Goulette,⁴⁹ A. G. Goussiou,¹⁴⁰ C. Goy,⁵ S. Gozpinar,²³ H. M. X. Gratas,¹³⁸ L. Graber,⁵⁴ I. Grabowska-Bold,^{38a} P. Grafström,^{20a,20b} K.-J. Grahn,⁴² J. Gramling,⁴⁹ E. Gramstad,¹¹⁹ S. Grancagnolo,¹⁶ V. Grassi,¹⁵⁰ V. Gratchev,¹²³ H. M. Gray,³⁰ E. Graziani,^{136a} O. G. Grebenyuk,¹²³ Z. D. Greenwood,^{79,n} K. Gregersen,⁷⁸ I. M. Gregor,⁴² P. Grenier,¹⁴⁵ J. Griffiths,⁸ A. A. Grillo,¹³⁹ K. Grimm,⁷² S. Grinstein,^{12,o} Ph. Gris,³⁴ Y. V. Grishkevich,⁹⁹ J.-F. Grivaz,¹¹⁷ J. P. Grohs,⁴⁴ A. Grohsjean,⁴² E. Gross,¹⁷⁴ J. Grosse-Knetter,⁵⁴ G. C. Grossi,^{135a,135b} J. Groth-Jensen,¹⁷⁴ Z. J. Grout,¹⁵¹ L. Guan,^{33b} J. Guenther,¹²⁸ F. Gescini,⁴⁹ D. Guest,¹⁷⁸ O. Gueta,¹⁵⁵ C. Guicheney,³⁴ E. Guido,^{50a,50b} T. Guillemin,¹¹⁷ S. Guindon,² U. Gul,⁵³ C. Gumpert,⁴⁴ J. Guo,³⁵ S. Gupta,¹²⁰ P. Gutierrez,¹¹³ N. G. Gutierrez Ortiz,⁵³ C. Gutschow,⁷⁸ N. Guttman,¹⁵⁵ C. Guyot,¹³⁸ C. Gwenlan,¹²⁰ C. B. Gwilliam,⁷⁴ A. Haas,¹¹⁰ C. Haber,¹⁵ H. K. Hadavand,⁸ N. Haddad,^{137e} P. Haefner,²¹ S. Hageböck,²¹ Z. Hajduk,³⁹ H. Hakobyan,¹⁷⁹ M. Haleem,⁴² D. Hall,¹²⁰ G. Halladjian,⁹⁰ K. Hamacher,¹⁷⁷ P. Hamal,¹¹⁵ K. Hamano,¹⁷¹ M. Hamer,⁵⁴ A. Hamilton,^{147a} S. Hamilton,¹⁶³ G. N. Hamity,^{147c} P. G. Hamnett,⁴² L. Han,^{33b} K. Hanagaki,¹¹⁸ K. Hanawa,¹⁵⁷ M. Hance,¹⁵ P. Hanke,^{58a} R. Hanna,¹³⁸ J. B. Hansen,³⁶ J. D. Hansen,³⁶ P. H. Hansen,³⁶ K. Hara,¹⁶² A. S. Hard,¹⁷⁵ T. Harenberg,¹⁷⁷ F. Hariri,¹¹⁷ S. Harkusha,⁹² D. Harper,⁸⁹ R. D. Harrington,⁴⁶ O. M. Harris,¹⁴⁰ P. F. Harrison,¹⁷² F. Hartjes,¹⁰⁷ M. Hasegawa,⁶⁷

- S. Hasegawa,¹⁰³ Y. Hasegawa,¹⁴² A. Hasib,¹¹³ S. Hassani,¹³⁸ S. Haug,¹⁷ M. Hauschild,³⁰ R. Hauser,⁹⁰ M. Havranek,¹²⁷ C. M. Hawkes,¹⁸ R. J. Hawkings,³⁰ A. D. Hawkins,⁸¹ T. Hayashi,¹⁶² D. Hayden,⁹⁰ C. P. Hays,¹²⁰ H. S. Hayward,⁷⁴ S. J. Haywood,¹³¹ S. J. Head,¹⁸ T. Heck,⁸³ V. Hedberg,⁸¹ L. Heelan,⁸ S. Heim,¹²² T. Heim,¹⁷⁷ B. Heinemann,¹⁵ L. Heinrich,¹¹⁰ J. Hejbal,¹²⁷ L. Helary,²² C. Heller,¹⁰⁰ M. Heller,³⁰ S. Hellman,^{148a,148b} D. Hellmich,²¹ C. Helsens,³⁰ J. Henderson,¹²⁰ R. C. W. Henderson,⁷² Y. Heng,¹⁷⁵ C. Henglert,⁴² A. Henrichs,¹⁷⁸ A. M. Henriques Correia,³⁰ S. Henrot-Versille,¹¹⁷ G. H. Herbert,¹⁶ Y. Hernández Jiménez,¹⁶⁹ R. Herrberg-Schubert,¹⁶ G. Herten,⁴⁸ R. Hertenberger,¹⁰⁰ L. Hervas,³⁰ G. G. Hesketh,⁷⁸ N. P. Hessey,¹⁰⁷ R. Hickling,⁷⁶ E. Higón-Rodriguez,¹⁶⁹ E. Hill,¹⁷¹ J. C. Hill,²⁸ K. H. Hiller,⁴² S. Hillert,²¹ S. J. Hillier,¹⁸ I. Hinchliffe,¹⁵ E. Hines,¹²² M. Hirose,¹⁵⁹ D. Hirschbuehl,¹⁷⁷ J. Hobbs,¹⁵⁰ N. Hod,¹⁰⁷ M. C. Hodgkinson,¹⁴¹ P. Hodgson,¹⁴¹ A. Hoecker,³⁰ M. R. Hoeferkamp,¹⁰⁵ F. Hoenig,¹⁰⁰ J. Hoffman,⁴⁰ D. Hoffmann,⁸⁵ M. Hohlfeld,⁸³ T. R. Holmes,¹⁵ T. M. Hong,¹²² L. Hooft van Huysduynen,¹¹⁰ W. H. Hopkins,¹¹⁶ Y. Horii,¹⁰³ J.-Y. Hostachy,⁵⁵ S. Hou,¹⁵³ A. Hoummada,^{137a} J. Howard,¹²⁰ J. Howarth,⁴² M. Hrabovsky,¹¹⁵ I. Hristova,¹⁶ J. Hrvnac,¹¹⁷ T. Hryvn'ova,⁵ C. Hsu,^{147c} P. J. Hsu,⁸³ S.-C. Hsu,¹⁴⁰ D. Hu,³⁵ X. Hu,⁸⁹ Y. Huang,⁴² Z. Hubacek,³⁰ F. Hubaut,⁸⁵ F. Huegging,²¹ T. B. Huffman,¹²⁰ E. W. Hughes,³⁵ G. Hughes,⁷² M. Huhtinen,³⁰ T. A. Hülsing,⁸³ M. Hurwitz,¹⁵ N. Huseynov,^{65,c} J. Huston,⁹⁰ J. Huth,⁵⁷ G. Iacobucci,⁴⁹ G. Iakovidis,¹⁰ I. Ibragimov,¹⁴³ L. Iconomidou-Fayard,¹¹⁷ E. Ideal,¹⁷⁸ Z. Idrissi,^{137e} P. Iengo,^{104a} O. Igolkina,¹⁰⁷ T. Iizawa,¹⁷³ Y. Ikegami,⁶⁶ K. Ikematsu,¹⁴³ M. Ikeno,⁶⁶ Y. Ilchenko,^{31,p} D. Iliadis,¹⁵⁶ N. Ilie,¹⁶⁰ Y. Inamaru,⁶⁷ T. Ince,¹⁰¹ P. Ioannou,⁹ M. Iodice,^{136a} K. Iordanidou,⁹ V. Ippolito,⁵⁷ A. Irles Quiles,¹⁶⁹ C. Isaksson,¹⁶⁸ M. Ishino,⁶⁸ M. Ishitsuka,¹⁵⁹ R. Ishmukhametov,¹¹¹ C. Issever,¹²⁰ S. Istin,^{19a} J. M. Iturbe Ponce,⁸⁴ R. Iuppa,^{135a,135b} J. Ivarsson,⁸¹ W. Iwanski,³⁹ H. Iwasaki,⁶⁶ J. M. Izen,⁴¹ V. Izzo,^{104a} B. Jackson,¹²² M. Jackson,⁷⁴ P. Jackson,¹ M. R. Jaekel,³⁰ V. Jain,² K. Jakobs,⁴⁸ S. Jakobsen,³⁰ T. Jakoubek,¹²⁷ J. Jakubek,¹²⁸ D. O. Jamin,¹⁵³ D. K. Jana,⁷⁹ E. Jansen,⁷⁸ H. Jansen,³⁰ J. Janssen,²¹ M. Janus,¹⁷² G. Jarlskog,⁸¹ N. Javadov,^{65,c} T. Javůrek,⁴⁸ L. Jeanty,¹⁵ J. Jejelava,^{51a,q} G.-Y. Jeng,¹⁵² D. Jennens,⁸⁸ P. Jenni,^{48,r} J. Jentzsch,⁴³ C. Jeske,¹⁷² S. Jézéquel,⁵ H. Ji,¹⁷⁵ J. Jia,¹⁵⁰ Y. Jiang,^{33b} M. Jimenez Belenguer,⁴² S. Jin,^{33a} A. Jinaru,^{26a} O. Jinnouchi,¹⁵⁹ M. D. Joergensen,³⁶ K. E. Johansson,^{148a,148b} P. Johansson,¹⁴¹ K. A. Johns,⁷ K. Jon-And,^{148a,148b} G. Jones,¹⁷² R. W. L. Jones,⁷² T. J. Jones,⁷⁴ J. Jongmanns,^{58a} P. M. Jorge,^{126a,126b} K. D. Joshi,⁸⁴ J. Jovicevic,¹⁴⁹ X. Ju,¹⁷⁵ C. A. Jung,⁴³ R. M. Jungst,³⁰ P. Jussel,⁶² A. Juste Rozas,^{12,o} M. Kaci,¹⁶⁹ A. Kaczmarśka,³⁹ M. Kado,¹¹⁷ H. Kagan,¹¹¹ M. Kagan,¹⁴⁵ E. Kajomovitz,⁴⁵ C. W. Kalderon,¹²⁰ S. Kama,⁴⁰ A. Kamenshchikov,¹³⁰ N. Kanaya,¹⁵⁷ M. Kaneda,³⁰ S. Kaneti,²⁸ V. A. Kantserov,⁹⁸ J. Kanzaki,⁶⁶ B. Kaplan,¹¹⁰ A. Kapliy,³¹ D. Kar,⁵³ K. Karakostas,¹⁰ N. Karastathis,¹⁰ M. J. Kareem,⁵⁴ M. Karnevskiy,⁸³ S. N. Karpov,⁶⁵ Z. M. Karpova,⁶⁵ K. Karthik,¹¹⁰ V. Kartvelishvili,⁷² A. N. Karyukhin,¹³⁰ L. Kashif,¹⁷⁵ G. Kasieczka,^{58b} R. D. Kass,¹¹¹ A. Kastanas,¹⁴ Y. Kataoka,¹⁵⁷ A. Katre,⁴⁹ J. Katzy,⁴² V. Kaushik,⁷ K. Kawagoe,⁷⁰ T. Kawamoto,¹⁵⁷ G. Kawamura,⁵⁴ S. Kazama,¹⁵⁷ V. F. Kazanin,¹⁰⁹ M. Y. Kazarinov,⁶⁵ R. Keeler,¹⁷¹ R. Kehoe,⁴⁰ M. Keil,⁵⁴ J. S. Keller,⁴² J. J. Kempster,⁷⁷ H. Keoshkerian,⁵ O. Kepka,¹²⁷ B. P. Kerševan,⁷⁵ S. Kersten,¹⁷⁷ K. Kessoku,¹⁵⁷ J. Keung,¹⁶⁰ F. Khalil-zada,¹¹ H. Khandanyan,^{148a,148b} A. Khanov,¹¹⁴ A. Khodinov,⁹⁸ A. Khomich,^{58a} T. J. Khoo,²⁸ G. Khoriauli,²¹ A. Khoroshilov,¹⁷⁷ V. Khovanskii,⁹⁷ E. Khramov,⁶⁵ J. Khubua,^{51b} H. Y. Kim,⁸ H. Kim,^{148a,148b} S. H. Kim,¹⁶² N. Kimura,¹⁷³ O. Kind,¹⁶ B. T. King,⁷⁴ M. King,¹⁶⁹ R. S. B. King,¹²⁰ S. B. King,¹⁷⁰ J. Kirk,¹³¹ A. E. Kiryunin,¹⁰¹ T. Kishimoto,⁶⁷ D. Kisielewska,^{38a} F. Kiss,⁴⁸ T. Kittelmann,¹²⁵ K. Kiuchi,¹⁶² E. Kladiva,^{146b} M. Klein,⁷⁴ U. Klein,⁷⁴ K. Kleinknecht,⁸³ P. Klimek,^{148a,148b} A. Klimentov,²⁵ R. Klingenberg,⁴³ J. A. Klinger,⁸⁴ T. Klioutchnikova,³⁰ P. F. Klok,¹⁰⁶ E.-E. Kluge,^{58a} P. Kluit,¹⁰⁷ S. Kluth,¹⁰¹ E. Kneringer,⁶² E. B. F. G. Knoops,⁸⁵ A. Knue,⁵³ D. Kobayashi,¹⁵⁹ T. Kobayashi,¹⁵⁷ M. Kobel,⁴⁴ M. Kocian,¹⁴⁵ P. Kodys,¹²⁹ P. Koevesarki,²¹ T. Koffas,²⁹ E. Koffeman,¹⁰⁷ L. A. Kogan,¹²⁰ S. Kohlmann,¹⁷⁷ Z. Kohout,¹²⁸ T. Kohriki,⁶⁶ T. Koi,¹⁴⁵ H. Kolanoski,¹⁶ I. Koletsou,⁵ J. Koll,⁹⁰ A. A. Komar,^{96,a} Y. Komori,¹⁵⁷ T. Kondo,⁶⁶ N. Kondrashova,⁴² K. Köneke,⁴⁸ A. C. König,¹⁰⁶ S. König,⁸³ T. Kono,^{66,s} R. Konoplich,^{110,t} N. Konstantinidis,⁷⁸ R. Kopeliansky,¹⁵⁴ S. Koperny,^{38a} L. Köpke,⁸³ A. K. Kopp,⁴⁸ K. Korcyl,³⁹ K. Kordas,¹⁵⁶ A. Korn,⁷⁸ A. A. Korol,^{109,d} I. Korolkov,¹² E. V. Korolkova,¹⁴¹ V. A. Korotkov,¹³⁰ O. Kortner,¹⁰¹ S. Kortner,¹⁰¹ V. V. Kostyukhin,²¹ V. M. Kotov,⁶⁵ A. Kotwal,⁴⁵ C. Kourkoumelis,⁹ V. Kouskoura,¹⁵⁶ A. Koutsman,^{161a} R. Kowalewski,¹⁷¹ T. Z. Kowalski,^{38a} W. Kozanecki,¹³⁸ A. S. Kozhin,¹³⁰ V. Kral,¹²⁸ V. A. Kramarenko,⁹⁹ G. Kramberger,⁷⁵ D. Krasnopevtsev,⁹⁸ A. Krasznahorkay,³⁰ J. K. Kraus,²¹ A. Kravchenko,²⁵ S. Kreiss,¹¹⁰ M. Kretz,^{58c} J. Kretzschmar,⁷⁴ K. Kreutzfeldt,⁵² P. Krieger,¹⁶⁰ K. Kroeninger,⁵⁴ H. Kroha,¹⁰¹ J. Kroll,¹²² J. Kroeseberg,²¹ J. Krstic,^{13a} U. Kruchonak,⁶⁵ H. Krüger,²¹ T. Kruker,¹⁷ N. Krumnack,⁶⁴ Z. V. Krumshteyn,⁶⁵ A. Kruse,¹⁷⁵ M. C. Kruse,⁴⁵ M. Kruskal,²² T. Kubota,⁸⁸ H. Kucuk,⁷⁸ S. Kuday,^{4c} S. Kuehn,⁴⁸ A. Kugel,^{58c} A. Kuhl,¹³⁹ T. Kuhl,⁴² V. Kukhtin,⁶⁵ Y. Kulchitsky,⁹² S. Kuleshov,^{32b} M. Kuna,^{134a,134b} J. Kunkle,¹²² A. Kupco,¹²⁷ H. Kurashige,⁶⁷ Y. A. Kurochkin,⁹² R. Kurumida,⁶⁷ V. Kus,¹²⁷ E. S. Kuwertz,¹⁴⁹ M. Kuze,¹⁵⁹ J. Kvita,¹¹⁵ A. La Rosa,⁴⁹ L. La Rotonda,^{37a,37b} C. Lacasta,¹⁶⁹ F. Lacava,^{134a,134b} J. Lacey,²⁹ H. Lacker,¹⁶

- D. Lacour,⁸⁰ V. R. Lacuesta,¹⁶⁹ E. Ladygin,⁶⁵ R. Lafaye,⁵ B. Laforge,⁸⁰ T. Lagouri,¹⁷⁸ S. Lai,⁴⁸ H. Laier,^{58a} L. Lambourne,⁷⁸ S. Lammers,⁶¹ C. L. Lampen,⁷ W. Lampl,⁷ E. Lançon,¹³⁸ U. Landgraf,⁴⁸ M. P. J. Landon,⁷⁶ V. S. Lang,^{58a} A. J. Lankford,¹⁶⁵ F. Lanni,²⁵ K. Lantzsch,³⁰ S. Laplace,⁸⁰ C. Lapoire,²¹ J. F. Laporte,¹³⁸ T. Lari,^{91a} F. Lasagni Manghi,^{20a,20b} M. Lassnig,³⁰ P. Laurelli,⁴⁷ W. Lavrijse, ¹⁵ A. T. Law,¹³⁹ P. Laycock,⁷⁴ O. Le Dortz,⁸⁰ E. Le Guirriec,⁸⁵ E. Le Menedeu,¹² T. LeCompte,⁶ F. Ledroit-Guillon,⁵⁵ C. A. Lee,¹⁵³ H. Lee,¹⁰⁷ J. S. H. Lee,¹¹⁸ S. C. Lee,¹⁵³ L. Lee,¹ G. Lefebvre,⁸⁰ M. Lefebvre,¹⁷¹ F. Legger,¹⁰⁰ C. Leggett,¹⁵ A. Lehan,⁷⁴ M. Lehacher,²¹ G. Lehmann Miotto,³⁰ X. Lei,⁷ W. A. Leight,²⁹ A. Leisos,¹⁵⁶ A. G. Leister,¹⁷⁸ M. A. L. Leite,^{24d} R. Leitner,¹²⁹ D. Lellouch,¹⁷⁴ B. Lemmer,⁵⁴ K. J. C. Leney,⁷⁸ T. Lenz,²¹ G. Lenzen,¹⁷⁷ B. Lenzi,³⁰ R. Leone,⁷ S. Leone,^{124a,124b} C. Leonidopoulos,⁴⁶ S. Leontsinis,¹⁰ C. Leroy,⁹⁵ C. G. Lester,²⁸ C. M. Lester,¹²² M. Levchenko,¹²³ J. Levêque,⁵ D. Levin,⁸⁹ L. J. Levinson,¹⁷⁴ M. Levy,¹⁸ A. Lewis,¹²⁰ G. H. Lewis,¹¹⁰ A. M. Leyko,²¹ M. Leyton,⁴¹ B. Li,^{33b,u} B. Li,⁸⁵ H. Li,¹⁵⁰ H. L. Li,³¹ L. Li,⁴⁵ L. Li,^{33e} S. Li,⁴⁵ Y. Li,^{33c,v} Z. Liang,¹³⁹ H. Liao,³⁴ B. Liberti,^{135a} P. Lichard,³⁰ K. Lie,¹⁶⁷ J. Liebal,²¹ W. Liebig,¹⁴ C. Limbach,²¹ A. Limosani,⁸⁸ S. C. Lin,^{153,w} T. H. Lin,⁸³ F. Linde,¹⁰⁷ B. E. Lindquist,¹⁵⁰ J. T. Linnemann,⁹⁰ E. Lipeles,¹²² A. Lipniacka,¹⁴ M. Lisovyi,⁴² T. M. Liss,¹⁶⁷ D. Lissauer,²⁵ A. Lister,¹⁷⁰ A. M. Litke,¹³⁹ B. Liu,¹⁵³ D. Liu,¹⁵³ J. B. Liu,^{33b} K. Liu,^{33b,x} L. Liu,⁸⁹ M. Liu,⁴⁵ M. Liu,^{33b} Y. Liu,^{33b} M. Livan,^{121a,121b} S. S. A. Livermore,¹²⁰ A. Lleres,⁵⁵ J. Llorente Merino,⁸² S. L. Lloyd,⁷⁶ F. Lo Sterzo,¹⁵³ E. Lobodzinska,⁴² P. Loch,⁷ W. S. Lockman,¹³⁹ T. Loddenkoetter,²¹ F. K. Loebinger,⁸⁴ A. E. Loevschall-Jensen,³⁶ A. Loginov,¹⁷⁸ T. Lohse,¹⁶ K. Lohwasser,⁴² M. Lokajicek,¹²⁷ V. P. Lombardo,⁵ B. A. Long,²² J. D. Long,⁸⁹ R. E. Long,⁷² L. Lopes,^{126a} D. Lopez Mateos,⁵⁷ B. Lopez Paredes,¹⁴¹ I. Lopez Paz,¹² J. Lorenz,¹⁰⁰ N. Lorenzo Martinez,⁶¹ M. Losada,¹⁶⁴ P. Loscutoff,¹⁵ X. Lou,⁴¹ A. Lounis,¹¹⁷ J. Love,⁶ P. A. Love,⁷² A. J. Lowe,^{145,g} F. Lu,^{33a} N. Lu,⁸⁹ H. J. Lubatti,¹⁴⁰ C. Luci,^{134a,134b} A. Lucotte,⁵⁵ F. Luehring,⁶¹ W. Lukas,⁶² L. Luminari,^{134a} O. Lundberg,^{148a,148b} B. Lund-Jensen,¹⁴⁹ M. Lungwitz,⁸³ D. Lynn,²⁵ R. Lysak,¹²⁷ E. Lytken,⁸¹ H. Ma,²⁵ L. L. Ma,^{33d} G. Maccarrone,⁴⁷ A. Macchiolo,¹⁰¹ J. Machado Miguens,^{126a,126b} D. Macina,³⁰ D. Madaffari,⁸⁵ R. Madar,⁴⁸ H. J. Maddocks,⁷² W. F. Mader,⁴⁴ A. Madsen,¹⁶⁸ M. Maeno,⁸ T. Maeno,²⁵ A. Maevskiy,⁹⁹ E. Magradze,⁵⁴ K. Mahboubi,⁴⁸ J. Mahlstedt,¹⁰⁷ S. Mahmoud,⁷⁴ C. Maiani,¹³⁸ C. Maidantchik,^{24a} A. A. Maier,¹⁰¹ A. Maio,^{126a,126b,126d} S. Majewski,¹¹⁶ Y. Makida,⁶⁶ N. Makovec,¹¹⁷ P. Mal,^{138,y} B. Malaescu,⁸⁰ Pa. Malecki,³⁹ V. P. Maleev,¹²³ F. Malek,⁵⁵ U. Mallik,⁶³ D. Malon,⁶ C. Malone,¹⁴⁵ S. Maltezos,¹⁰ V. M. Malyshev,¹⁰⁹ S. Malyukov,³⁰ J. Mamuzic,^{13b} B. Mandelli,³⁰ L. Mandelli,^{91a} I. Mandić,⁷⁵ R. Mandrysch,⁶³ J. Maneira,^{126a,126b} A. Manfredini,¹⁰¹ L. Manhaes de Andrade Filho,^{24b} J. A. Manjarres Ramos,^{161b} A. Mann,¹⁰⁰ P. M. Manning,¹³⁹ A. Manousakis-Katsikakis,⁹ B. Mansoulie,¹³⁸ R. Mantifel,⁸⁷ L. Mapelli,³⁰ L. March,^{147c} J. F. Marchand,²⁹ G. Marchiori,⁸⁰ M. Marcisovsky,¹²⁷ C. P. Marino,¹⁷¹ M. Marjanovic,^{13a} C. N. Marques,^{126a} F. Marroquim,^{24a} S. P. Marsden,⁸⁴ Z. Marshall,¹⁵ L. F. Marti,¹⁷ S. Marti-Garcia,¹⁶⁹ B. Martin,³⁰ B. Martin,⁹⁰ T. A. Martin,¹⁷² V. J. Martin,⁴⁶ B. Martin dit Latour,¹⁴ H. Martinez,¹³⁸ M. Martinez,^{12,o} S. Martin-Haugh,¹³¹ A. C. Martyniuk,⁷⁸ M. Marx,¹⁴⁰ F. Marzano,^{134a} A. Marzin,³⁰ L. Masetti,⁸³ T. Mashimo,¹⁵⁷ R. Mashinistov,⁹⁶ J. Masik,⁸⁴ A. L. Maslennikov,^{109,d} I. Massa,^{20a,20b} L. Massa,^{20a,20b} N. Massol,⁵ P. Mastrandrea,¹⁵⁰ A. Mastroberardino,^{37a,37b} T. Masubuchi,¹⁵⁷ P. Mättig,¹⁷⁷ J. Mattmann,⁸³ J. Maurer,^{26a} S. J. Maxfield,⁷⁴ D. A. Maximov,^{109,d} R. Mazini,¹⁵³ L. Mazzaferro,^{135a,135b} G. Mc Goldrick,¹⁶⁰ S. P. Mc Kee,⁸⁹ A. McCarn,⁸⁹ R. L. McCarthy,¹⁵⁰ T. G. McCarthy,²⁹ N. A. McCubbin,¹³¹ K. W. McFarlane,^{56,a} J. A. McFayden,⁷⁸ G. McHedlidze,⁵⁴ S. J. McMahon,¹³¹ R. A. McPherson,^{171,k} J. Mechnick,¹⁰⁷ M. Medinnis,⁴² S. Meehan,³¹ S. Mehlhase,¹⁰⁰ A. Mehta,⁷⁴ K. Meier,^{58a} C. Meineck,¹⁰⁰ B. Meirose,⁸¹ C. Melachrinos,³¹ B. R. Mellado Garcia,^{147c} F. Meloni,¹⁷ A. Mengarelli,^{20a,20b} S. Menke,¹⁰¹ E. Meoni,¹⁶³ K. M. Mercurio,⁵⁷ S. Mergelmeyer,²¹ N. Meric,¹³⁸ P. Mermod,⁴⁹ L. Merola,^{104a,104b} C. Meroni,^{91a} F. S. Merritt,³¹ H. Merritt,¹¹¹ A. Messina,^{30,z} J. Metcalfe,²⁵ A. S. Mete,¹⁶⁵ C. Meyer,⁸³ C. Meyer,¹²² J.-P. Meyer,¹³⁸ J. Meyer,³⁰ R. P. Middleton,¹³¹ S. Migas,⁷⁴ L. Mijović,²¹ G. Mikenberg,¹⁷⁴ M. Mikestikova,¹²⁷ M. Mikuž,⁷⁵ A. Milic,³⁰ D. W. Miller,³¹ C. Mills,⁴⁶ A. Milov,¹⁷⁴ D. A. Milstead,^{148a,148b} D. Milstein,¹⁷⁴ A. A. Minaenko,¹³⁰ Y. Minami,¹⁵⁷ I. A. Minashvili,⁶⁵ A. I. Mincer,¹¹⁰ B. Mindur,^{38a} M. Mineev,⁶⁵ Y. Ming,¹⁷⁵ L. M. Mir,¹² G. Mirabelli,^{134a} T. Mitani,¹⁷³ J. Mitrevski,¹⁰⁰ V. A. Mitsou,¹⁶⁹ S. Mitsui,⁶⁶ A. Miucci,⁴⁹ P. S. Miyagawa,¹⁴¹ J. U. Mjörnmark,⁸¹ T. Moa,^{148a,148b} K. Mochizuki,⁸⁵ S. Mohapatra,³⁵ W. Mohr,⁴⁸ S. Molander,^{148a,148b} R. Moles-Valls,¹⁶⁹ K. Mönig,⁴² C. Monini,⁵⁵ J. Monk,³⁶ E. Monnier,⁸⁵ J. Montejo Berlingen,¹² F. Monticelli,⁷¹ S. Monzani,^{134a,134b} R. W. Moore,³ N. Morange,⁶³ D. Moreno,⁸³ M. Moreno Llácer,⁵⁴ P. Morettini,^{50a} M. Morgenstern,⁴⁴ M. Morii,⁵⁷ S. Moritz,⁸³ A. K. Morley,¹⁴⁹ G. Mornacchi,³⁰ J. D. Morris,⁷⁶ L. Morvaj,¹⁰³ H. G. Moser,¹⁰¹ M. Mosidze,^{51b} J. Moss,¹¹¹ K. Motohashi,¹⁵⁹ R. Mount,¹⁴⁵ E. Mountricha,²⁵ S. V. Mouraviev,^{96,a} E. J. W. Moyse,⁸⁶ S. Muanza,⁸⁵ R. D. Mudd,¹⁸ F. Mueller,^{58a} J. Mueller,¹²⁵ K. Mueller,²¹ T. Mueller,²⁸ T. Mueller,⁸³ D. Muenstermann,⁴⁹ Y. Munwes,¹⁵⁵ J. A. Murillo Quijada,¹⁸ W. J. Murray,^{172,131} H. Musheghyan,⁵⁴ E. Musto,¹⁵⁴ A. G. Myagkov,^{130,aa} M. Myska,¹²⁸ O. Nackenhorst,⁵⁴ J. Nadal,⁵⁴ K. Nagai,⁶² R. Nagai,¹⁵⁹ Y. Nagai,⁸⁵

- K. Nagano,⁶⁶ A. Nagarkar,¹¹¹ Y. Nagasaka,⁵⁹ M. Nagel,¹⁰¹ A. M. Nairz,³⁰ Y. Nakahama,³⁰ K. Nakamura,⁶⁶ T. Nakamura,¹⁵⁷
 I. Nakano,¹¹² H. Namasivayam,⁴¹ G. Nanava,²¹ R. Narayan,^{58b} T. Nattermann,²¹ T. Naumann,⁴² G. Navarro,¹⁶⁴ R. Nayyar,⁷
 H. A. Neal,⁸⁹ P. Yu. Nechaeva,⁹⁶ T. J. Neep,⁸⁴ P. D. Nef,¹⁴⁵ A. Negri,^{121a,121b} G. Negri,³⁰ M. Negrini,^{20a} S. Nektarijevic,⁴⁹
 C. Nellist,¹¹⁷ A. Nelson,¹⁶⁵ T. K. Nelson,¹⁴⁵ S. Nemecek,¹²⁷ P. Nemethy,¹¹⁰ A. A. Nepomuceno,^{24a} M. Nessi,^{30,bb}
 M. S. Neubauer,¹⁶⁷ M. Neumann,¹⁷⁷ R. M. Neves,¹¹⁰ P. Nevski,²⁵ P. R. Newman,¹⁸ D. H. Nguyen,⁶ R. B. Nickerson,¹²⁰
 R. Nicolaïdou,¹³⁸ B. Nicquevert,³⁰ J. Nielsen,¹³⁹ N. Nikiforou,³⁵ A. Nikiforov,¹⁶ V. Nikolaenko,^{130,aa} I. Nikolic-Audit,⁸⁰
 K. Nikolic,⁴⁹ K. Nikolopoulos,¹⁸ P. Nilsson,⁸ Y. Ninomiya,¹⁵⁷ A. Nisati,^{134a} R. Nisius,¹⁰¹ T. Nobe,¹⁵⁹ L. Nodulman,⁶
 M. Nomachi,¹¹⁸ I. Nomidis,²⁹ S. Norberg,¹¹³ M. Nordberg,³⁰ O. Novgorodova,⁴⁴ S. Nowak,¹⁰¹ M. Nozaki,⁶⁶ L. Nozka,¹¹⁵
 K. Ntekas,¹⁰ G. Nunes Hanninger,⁸⁸ T. Nunnemann,¹⁰⁰ E. Nurse,⁷⁸ F. Nuti,⁸⁸ B. J. O'Brien,⁴⁶ F. O'grady,⁷ D. C. O'Neil,¹⁴⁴
 V. O'Shea,⁵³ F. G. Oakham,^{29,f} H. Oberlack,¹⁰¹ T. Obermann,²¹ J. Ocariz,⁸⁰ A. Ochi,⁶⁷ M. I. Ochoa,⁷⁸ S. Oda,⁷⁰ S. Odaka,⁶⁶
 H. Ogren,⁶¹ A. Oh,⁸⁴ S. H. Oh,⁴⁵ C. C. Ohm,¹⁵ H. Ohman,¹⁶⁸ W. Okamura,¹¹⁸ H. Okawa,²⁵ Y. Okumura,³¹ T. Okuyama,¹⁵⁷
 A. Olariu,^{26a} A. G. Olchevski,⁶⁵ S. A. Olivares Pino,⁴⁶ D. Oliveira Damazio,²⁵ E. Oliver Garcia,¹⁶⁹ A. Olszewski,³⁹
 J. Olszowska,³⁹ A. Onofre,^{126a,126e} P. U. E. Onyisi,^{31,p} C. J. Oram,^{161a} M. J. Oreglia,³¹ Y. Oren,¹⁵⁵ D. Orestano,^{136a,136b}
 N. Orlando,^{73a,73b} C. Oropeza Barrera,⁵³ R. S. Orr,¹⁶⁰ B. Osculati,^{50a,50b} R. Ospanov,¹²² G. Otero y Garzon,²⁷ H. Otono,⁷⁰
 M. Ouchrif,^{137d} E. A. Ouellette,¹⁷¹ F. Ould-Saada,¹¹⁹ A. Ouraou,¹³⁸ K. P. Oussoren,¹⁰⁷ Q. Ouyang,^{33a} A. Ovcharova,¹⁵
 M. Owen,⁸⁴ V. E. Ozcan,^{19a} N. Ozturk,⁸ K. Pachal,¹²⁰ A. Pacheco Pages,¹² C. Padilla Aranda,¹² M. Pagáčová,⁴⁸
 S. Pagan Griso,¹⁵ E. Paganis,¹⁴¹ C. Pahl,¹⁰¹ F. Paige,²⁵ P. Pais,⁸⁶ K. Pajchel,¹¹⁹ G. Palacino,^{161b} S. Palestini,³⁰ M. Palka,^{38b}
 D. Pallin,³⁴ A. Palma,^{126a,126b} J. D. Palmer,¹⁸ Y. B. Pan,¹⁷⁵ E. Panagiotopoulou,¹⁰ J. G. Panduro Vazquez,⁷⁷ P. Pani,¹⁰⁷
 N. Panikashvili,⁸⁹ S. Panitkin,²⁵ D. Pantea,^{26a} L. Paolozzi,^{135a,135b} Th. D. Papadopoulou,¹⁰ K. Papageorgiou,^{156,m}
 A. Paramonov,⁶ D. Paredes Hernandez,¹⁵⁶ M. A. Parker,²⁸ F. Parodi,^{50a,50b} J. A. Parsons,³⁵ U. Parzefall,⁴⁸ E. Pasqualucci,^{134a}
 S. Passaggio,^{50a} A. Passeri,^{136a} F. Pastore,^{136a,136b,a} Fr. Pastore,⁷⁷ G. Pásztor,²⁹ S. Pataraia,¹⁷⁷ N. D. Patel,¹⁵² J. R. Pater,⁸⁴
 S. Patricelli,^{104a,104b} T. Pauly,³⁰ J. Pearce,¹⁷¹ L. E. Pedersen,³⁶ M. Pedersen,¹¹⁹ S. Pedraza Lopez,¹⁶⁹ R. Pedro,^{126a,126b}
 S. V. Peleganchuk,¹⁰⁹ D. Pelikan,¹⁶⁸ H. Peng,^{33b} B. Penning,³¹ J. Penwell,⁶¹ D. V. Perepelitsa,²⁵ E. Perez Codina,^{161a}
 M. T. Pérez García-Estañ,¹⁶⁹ V. Perez Reale,³⁵ L. Perini,^{91a,91b} H. Pernegger,³⁰ S. Perrella,^{104a,104b} R. Perrino,^{73a}
 R. Peschke,⁴² V. D. Peshekhonov,⁶⁵ K. Peters,³⁰ R. F. Y. Peters,⁸⁴ B. A. Petersen,³⁰ T. C. Petersen,³⁶ E. Petit,⁴²
 A. Petridis,^{148a,148b} C. Petridou,¹⁵⁶ E. Petrolo,^{134a} F. Petrucci,^{136a,136b} N. E. Pettersson,¹⁵⁹ R. Pezoa,^{32b} P. W. Phillips,¹³¹
 G. Piacquadio,¹⁴⁵ E. Pianori,¹⁷² A. Picazio,⁴⁹ E. Piccaro,⁷⁶ M. Piccinini,^{20a,20b} R. Piegaia,²⁷ D. T. Pignotti,¹¹¹ J. E. Pilcher,³¹
 A. D. Pilkington,⁷⁸ J. Pina,^{126a,126b,126d} M. Pinamonti,^{166a,166c,cc} A. Pinder,¹²⁰ J. L. Pinfold,³ A. Pingel,³⁶ B. Pinto,^{126a}
 S. Pires,⁸⁰ M. Pitt,¹⁷⁴ C. Pizio,^{91a,91b} L. Plazak,^{146a} M.-A. Pleier,²⁵ V. Pleskot,¹²⁹ E. Plotnikova,⁶⁵ P. Plucinski,^{148a,148b}
 D. Pluth,⁶⁴ S. Poddar,^{58a} F. Podlyski,³⁴ R. Poettgen,⁸³ L. Poggioli,¹¹⁷ D. Pohl,²¹ M. Pohl,⁴⁹ G. Polesello,^{121a}
 A. Pollicchio,^{37a,37b} R. Polifka,¹⁶⁰ A. Polini,^{20a} C. S. Pollard,⁴⁵ V. Polychronakos,²⁵ K. Pommès,³⁰ L. Pontecorvo,^{134a}
 B. G. Pope,⁹⁰ G. A. Popenciu,^{26b} D. S. Popovic,^{13a} A. Poppleton,³⁰ X. Portell Bueso,¹² S. Pospisil,¹²⁸ K. Potamianos,¹⁵
 I. N. Potrap,⁶⁵ C. J. Potter,¹⁵¹ C. T. Potter,¹¹⁶ G. Pouillard,³⁰ J. Poveda,⁶¹ V. Pozdnyakov,⁶⁵ P. Pralavorio,⁸⁵ A. Pranko,¹⁵
 S. Prasad,³⁰ R. Pravahan,⁸ S. Prell,⁶⁴ D. Price,⁸⁴ J. Price,⁷⁴ L. E. Price,⁶ D. Prieur,¹²⁵ M. Primavera,^{73a} M. Proissl,⁴⁶
 K. Prokofiev,⁴⁷ F. Prokoshin,^{32b} E. Protopapadaki,¹³⁸ S. Protopopescu,²⁵ J. Proudfoot,⁶ M. Przybycien,^{38a} H. Przysiezniak,⁵
 E. Ptacek,¹¹⁶ D. Puddu,^{136a,136b} E. Pueschel,⁸⁶ D. Puldon,¹⁵⁰ M. Purohit,^{25,dd} P. Puzo,¹¹⁷ J. Qian,⁸⁹ G. Qin,⁵³ Y. Qin,⁸⁴
 A. Quadt,⁵⁴ D. R. Quarrie,¹⁵ W. B. Quayle,^{166a,166b} M. Queitsch-Maitland,⁸⁴ D. Quilty,⁵³ A. Qureshi,^{161b} V. Radeka,²⁵
 V. Radescu,⁴² S. K. Radhakrishnan,¹⁵⁰ P. Radloff,¹¹⁶ P. Rados,⁸⁸ F. Ragusa,^{91a,91b} G. Rahal,¹⁸⁰ S. Rajagopalan,²⁵
 M. Rammensee,³⁰ A. S. Randle-Conde,⁴⁰ C. Rangel-Smith,¹⁶⁸ K. Rao,¹⁶⁵ F. Rauscher,¹⁰⁰ T. C. Rave,⁴⁸ T. Ravenscroft,⁵³
 M. Raymond,³⁰ A. L. Read,¹¹⁹ N. P. Readioff,⁷⁴ D. M. Rebuzzi,^{121a,121b} A. Redelbach,¹⁷⁶ G. Redlinger,²⁵ R. Reece,¹³⁹
 K. Reeves,⁴¹ L. Rehnisch,¹⁶ H. Reisin,²⁷ M. Relich,¹⁶⁵ C. Rembser,³⁰ H. Ren,^{33a} Z. L. Ren,¹⁵³ A. Renaud,¹¹⁷
 M. Rescigno,^{134a} S. Resconi,^{91a} O. L. Rezanova,^{109,d} P. Reznicek,¹²⁹ R. Rezvani,⁹⁵ R. Richter,¹⁰¹ M. Ridel,⁸⁰ P. Rieck,¹⁶
 J. Rieger,⁵⁴ M. Rijssenbeek,¹⁵⁰ A. Rimoldi,^{121a,121b} L. Rinaldi,^{20a} E. Ritsch,⁶² I. Riu,¹² F. Rizatdinova,¹¹⁴ E. Rizvi,⁷⁶
 S. H. Robertson,^{87,k} A. Robichaud-Veronneau,⁸⁷ D. Robinson,²⁸ J. E. M. Robinson,⁸⁴ A. Robson,⁵³ C. Roda,^{124a,124b}
 L. Rodrigues,³⁰ S. Roe,³⁰ O. Røhne,¹¹⁹ S. Rolli,¹⁶³ A. Romaniouk,⁹⁸ M. Romano,^{20a,20b} E. Romero Adam,¹⁶⁹
 N. Rompotis,¹⁴⁰ M. Ronzani,⁴⁸ L. Roos,⁸⁰ E. Ros,¹⁶⁹ S. Rosati,^{134a} K. Rosbach,⁴⁹ M. Rose,⁷⁷ P. Rose,¹³⁹ P. L. Rosendahl,¹⁴
 O. Rosenthal,¹⁴³ V. Rossetti,^{148a,148b} E. Rossi,^{104a,104b} L. P. Rossi,^{50a} R. Rosten,¹⁴⁰ M. Rotaru,^{26a} I. Roth,¹⁷⁴ J. Rothberg,¹⁴⁰
 D. Rousseau,¹¹⁷ C. R. Royon,¹³⁸ A. Rozanov,⁸⁵ Y. Rozen,¹⁵⁴ X. Ruan,^{147c} F. Rubbo,¹² I. Rubinsky,⁴² V. I. Rud,⁹⁹
 C. Rudolph,⁴⁴ M. S. Rudolph,¹⁶⁰ F. Rühr,⁴⁸ A. Ruiz-Martinez,³⁰ Z. Rurikova,⁴⁸ N. A. Rusakovich,⁶⁵ A. Ruschke,¹⁰⁰

- J. P. Rutherford,⁷ N. Ruthmann,⁴⁸ Y. F. Ryabov,¹²³ M. Rybar,¹²⁹ G. Rybkin,¹¹⁷ N. C. Ryder,¹²⁰ A. F. Saavedra,¹⁵²
 G. Sabato,¹⁰⁷ S. Sacerdoti,²⁷ A. Saddique,³ I. Sadeh,¹⁵⁵ H. F-W. Sadrozinski,¹³⁹ R. Sadykov,⁶⁵ F. Safai Tehrani,^{134a}
 H. Sakamoto,¹⁵⁷ Y. Sakurai,¹⁷³ G. Salamanna,^{136a,136b} A. Salamon,^{135a} M. Saleem,¹¹³ D. Salek,¹⁰⁷ P. H. Sales De Bruin,¹⁴⁰
 D. Salihagic,¹⁰¹ A. Salnikov,¹⁴⁵ J. Salt,¹⁶⁹ D. Salvatore,^{37a,37b} F. Salvatore,¹⁵¹ A. Salvucci,¹⁰⁶ A. Salzburger,³⁰
 D. Sampsonidis,¹⁵⁶ A. Sanchez,^{104a,104b} J. Sánchez,¹⁶⁹ V. Sanchez Martinez,¹⁶⁹ H. Sandaker,¹⁴ R. L. Sandbach,⁷⁶
 H. G. Sander,⁸³ M. P. Sanders,¹⁰⁰ M. Sandhoff,¹⁷⁷ T. Sandoval,²⁸ C. Sandoval,¹⁶⁴ R. Sandstroem,¹⁰¹ D. P. C. Sankey,¹³¹
 A. Sansoni,⁴⁷ C. Santoni,³⁴ R. Santonico,^{135a,135b} H. Santos,^{126a} I. Santoyo Castillo,¹⁵¹ K. Sapp,¹²⁵ A. Sapronov,⁶⁵
 J. G. Saraiva,^{126a,126d} B. Sarrazin,²¹ G. Sartisohn,¹⁷⁷ O. Sasaki,⁶⁶ Y. Sasaki,¹⁵⁷ G. Sauvage,^{5,a} E. Sauvan,⁵ P. Savard,^{160,f}
 D. O. Savu,³⁰ C. Sawyer,¹²⁰ L. Sawyer,^{79,n} D. H. Saxon,⁵³ J. Saxon,¹²² C. Sbarra,^{20a} A. Sbrizzi,^{20a,20b} T. Scanlon,⁷⁸
 D. A. Scannicchio,¹⁶⁵ M. Scarcella,¹⁵² V. Scarfone,^{37a,37b} J. Schaarschmidt,¹⁷⁴ P. Schacht,¹⁰¹ D. Schaefer,³⁰ R. Schaefer,⁴²
 S. Schaepe,²¹ S. Schaetzl,^{58b} U. Schäfer,⁸³ A. C. Schaffer,¹¹⁷ D. Schaile,¹⁰⁰ R. D. Schamberger,¹⁵⁰ V. Scharf,^{58a}
 V. A. Schegelsky,¹²³ D. Scheirich,¹²⁹ M. Schernau,¹⁶⁵ M. I. Scherzer,³⁵ C. Schiavi,^{50a,50b} J. Schieck,¹⁰⁰ C. Schillo,⁴⁸
 M. Schioppa,^{37a,37b} S. Schlenker,³⁰ E. Schmidt,⁴⁸ K. Schmieden,³⁰ C. Schmitt,⁸³ S. Schmitt,^{58b} B. Schneider,¹⁷
 Y. J. Schnellbach,⁷⁴ U. Schnoor,⁴⁴ L. Schoeffel,¹³⁸ A. Schoening,^{58b} B. D. Schoenrock,⁹⁰ A. L. S. Schorlemmer,⁵⁴
 M. Schott,⁸³ D. Schouten,^{161a} J. Schovancova,²⁵ S. Schramm,¹⁶⁰ M. Schreyer,¹⁷⁶ C. Schroeder,⁸³ N. Schuh,⁸³
 M. J. Schultens,²¹ H.-C. Schultz-Coulon,^{58a} H. Schulz,¹⁶ M. Schumacher,⁴⁸ B. A. Schumm,¹³⁹ Ph. Schune,¹³⁸
 C. Schwanenberger,⁸⁴ A. Schwartzman,¹⁴⁵ T. A. Schwarz,⁸⁹ Ph. Schwegler,¹⁰¹ Ph. Schwemling,¹³⁸ R. Schwienhorst,⁹⁰
 J. Schwindling,¹³⁸ T. Schwindt,²¹ M. Schwoerer,⁵ F. G. Sciacca,¹⁷ E. Scifo,¹¹⁷ G. Sciolla,²³ W. G. Scott,¹³¹ F. Scuri,^{124a,124b}
 F. Scutti,²¹ J. Searcy,⁸⁹ G. Sedov,⁴² E. Sedykh,¹²³ S. C. Seidel,¹⁰⁵ A. Seiden,¹³⁹ F. Seifert,¹²⁸ J. M. Seixas,^{24a}
 G. Sekhniaidze,^{104a} S. J. Sekula,⁴⁰ K. E. Selbach,⁴⁶ D. M. Seliverstov,^{123,a} G. Sellers,⁷⁴ N. Semprini-Cesari,^{20a,20b}
 C. Serfon,³⁰ L. Serin,¹¹⁷ L. Serkin,⁵⁴ T. Serre,⁸⁵ R. Seuster,^{161a} H. Severini,¹¹³ T. Sfiligoj,⁷⁵ F. Sforza,¹⁰¹ A. Sfyrla,³⁰
 E. Shabalina,⁵⁴ M. Shamim,¹¹⁶ L. Y. Shan,^{33a} R. Shang,¹⁶⁷ J. T. Shank,²² M. Shapiro,¹⁵ P. B. Shatalov,⁹⁷ K. Shaw,^{166a,166b}
 C. Y. Shehu,¹⁵¹ P. Sherwood,⁷⁸ L. Shi,^{153,ee} S. Shimizu,⁶⁷ C. O. Shimmin,¹⁶⁵ M. Shimojima,¹⁰² M. Shiyakova,⁶⁵
 A. Shmeleva,⁹⁶ M. J. Shochet,³¹ D. Short,¹²⁰ S. Shrestha,⁶⁴ E. Shulga,⁹⁸ M. A. Shupe,⁷ S. Shushkevich,⁴² P. Sicho,¹²⁷
 O. Sidiropoulou,¹⁵⁶ D. Sidorov,¹¹⁴ A. Sidoti,^{134a} F. Siegert,⁴⁴ Dj. Sijacki,^{13a} J. Silva,^{126a,126d} Y. Silver,¹⁵⁵ D. Silverstein,¹⁴⁵
 S. B. Silverstein,^{148a} V. Simak,¹²⁸ O. Simard,⁵ Lj. Simic,^{13a} S. Simion,¹¹⁷ E. Simioni,⁸³ B. Simmons,⁷⁸ R. Simonello,^{91a,91b}
 M. Simonyan,³⁶ P. Sinervo,¹⁶⁰ N. B. Sinev,¹¹⁶ V. Sipica,¹⁴³ G. Siragusa,¹⁷⁶ A. Sircar,⁷⁹ A. N. Sisakyan,^{65,a}
 S. Yu. Sivoklokov,⁹⁹ J. Sjölin,^{148a,148b} T. B. Sjursen,¹⁴ H. P. Skottowe,⁵⁷ K. Yu. Skovpen,¹⁰⁹ P. Skubic,¹¹³ M. Slater,¹⁸
 T. Slavicek,¹²⁸ M. Slawinska,¹⁰⁷ K. Sliwa,¹⁶³ V. Smakhtin,¹⁷⁴ B. H. Smart,⁴⁶ L. Smestad,¹⁴ S. Yu. Smirnov,⁹⁸ Y. Smirnov,⁹⁸
 L. N. Smirnova,^{99,ff} O. Smirnova,⁸¹ K. M. Smith,⁵³ M. Smizanska,⁷² K. Smolek,¹²⁸ A. A. Snesarov,⁹⁶ G. Snidero,⁷⁶
 S. Snyder,²⁵ R. Sobie,^{171,k} F. Socher,⁴⁴ A. Soffer,¹⁵⁵ D. A. Soh,^{153,ee} C. A. Solans,³⁰ M. Solar,¹²⁸ J. Solc,¹²⁸ E. Yu. Soldatov,⁹⁸
 U. Soldevila,¹⁶⁹ A. A. Solodkov,¹³⁰ A. Soloshenko,⁶⁵ O. V. Solovyanov,¹³⁰ V. Solovyev,¹²³ P. Sommer,⁴⁸ H. Y. Song,^{33b}
 N. Soni,¹ A. Sood,¹⁵ A. Sopczak,¹²⁸ B. Sopko,¹²⁸ V. Sopko,¹²⁸ V. Sorin,¹² M. Sosebee,⁸ R. Soualah,^{166a,166c} P. Soueid,⁹⁵
 A. M. Soukharev,^{109,d} D. South,⁴² S. Spagnolo,^{73a,73b} F. Spanò,⁷⁷ W. R. Spearman,⁵⁷ F. Spettel,¹⁰¹ R. Spighi,^{20a} G. Spigo,³⁰
 L. A. Spiller,⁸⁸ M. Spousta,¹²⁹ T. Spreitzer,¹⁶⁰ B. Spurlock,⁸ R. D. St. Denis,^{53,a} S. Staerz,⁴⁴ J. Stahlman,¹²² R. Stamen,^{58a}
 S. Stamm,¹⁶ E. Stanecka,³⁹ R. W. Stanek,⁶ C. Stanescu,^{136a} M. Stanescu-Bellu,⁴² M. M. Stanitzki,⁴² S. Stapnes,¹¹⁹
 E. A. Starchenko,¹³⁰ J. Stark,⁵⁵ P. Staroba,¹²⁷ P. Starovoitov,⁴² R. Staszewski,³⁹ P. Stavina,^{146a,a} P. Steinberg,²⁵ B. Stelzer,¹⁴⁴
 H. J. Stelzer,³⁰ O. Stelzer-Chilton,^{161a} H. Stenzel,⁵² S. Stern,¹⁰¹ G. A. Stewart,⁵³ J. A. Stillings,²¹ M. C. Stockton,⁸⁷
 M. Stoebbe,⁸⁷ G. Stoica,^{26a} P. Stolte,⁵⁴ S. Stonjek,¹⁰¹ A. R. Stradling,⁸ A. Straessner,⁴⁴ M. E. Stramaglia,¹⁷ J. Strandberg,¹⁴⁹
 S. Strandberg,^{148a,148b} A. Strandlie,¹¹⁹ E. Strauss,¹⁴⁵ M. Strauss,¹¹³ P. Strizenec,^{146b} R. Ströhmer,¹⁷⁶ D. M. Strom,¹¹⁶
 R. Stroynowski,⁴⁰ A. Strubig,¹⁰⁶ S. A. Stucci,¹⁷ B. Stugu,¹⁴ N. A. Styles,⁴² D. Su,¹⁴⁵ J. Su,¹²⁵ R. Subramaniam,⁷⁹
 A. Succurro,¹² Y. Sugaya,¹¹⁸ C. Suhr,¹⁰⁸ M. Suk,¹²⁸ V. V. Sulin,⁹⁶ S. Sultansoy,^{4d} T. Sumida,⁶⁸ S. Sun,⁵⁷ X. Sun,^{33a}
 J. E. Sundermann,⁴⁸ K. Suruliz,¹⁴¹ G. Susinno,^{37a,37b} M. R. Sutton,¹⁵¹ Y. Suzuki,⁶⁶ M. Svatos,¹²⁷ S. Swedish,¹⁷⁰
 M. Swiatlowski,¹⁴⁵ I. Sykora,^{146a} T. Sykora,¹²⁹ D. Ta,⁹⁰ C. Taccini,^{136a,136b} K. Tackmann,⁴² J. Taenzer,¹⁶⁰ A. Taffard,¹⁶⁵
 R. Tafirout,^{161a} N. Taiblum,¹⁵⁵ H. Takai,²⁵ R. Takashima,⁶⁹ H. Takeda,⁶⁷ T. Takeshita,¹⁴² Y. Takubo,⁶⁶ M. Talby,⁸⁵
 A. A. Talyshev,^{109,d} J. Y. C. Tam,¹⁷⁶ K. G. Tan,⁸⁸ J. Tanaka,¹⁵⁷ R. Tanaka,¹¹⁷ S. Tanaka,¹³³ S. Tanaka,⁶⁶ A. J. Tanasijczuk,¹⁴⁴
 B. B. Tannenwald,¹¹¹ N. Tannoury,²¹ S. Tapprogge,⁸³ S. Tarem,¹⁵⁴ F. Tarrade,²⁹ G. F. Tartarelli,^{91a} P. Tas,¹²⁹ M. Tasevsky,¹²⁷
 T. Tashiro,⁶⁸ E. Tassi,^{37a,37b} A. Tavares Delgado,^{126a,126b} Y. Tayalati,^{137d} F. E. Taylor,⁹⁴ G. N. Taylor,⁸⁸ W. Taylor,^{161b}
 F. A. Teischinger,³⁰ M. Teixeira Dias Castanheira,⁷⁶ P. Teixeira-Dias,⁷⁷ K. K. Temming,⁴⁸ H. Ten Kate,³⁰ P. K. Teng,¹⁵³

- J. J. Teoh,¹¹⁸ S. Terada,⁶⁶ K. Terashi,¹⁵⁷ J. Terron,⁸² S. Terzo,¹⁰¹ M. Testa,⁴⁷ R. J. Teuscher,^{160,k} J. Therhaag,²¹
 T. Theveneaux-Pelzer,³⁴ J. P. Thomas,¹⁸ J. Thomas-Wilsker,⁷⁷ E. N. Thompson,³⁵ P. D. Thompson,¹⁸ P. D. Thompson,¹⁶⁰
 R. J. Thompson,⁸⁴ A. S. Thompson,⁵³ L. A. Thomsen,³⁶ E. Thomson,¹²² M. Thomson,²⁸ W. M. Thong,⁸⁸ R. P. Thun,^{89,a}
 F. Tian,³⁵ M. J. Tibbetts,¹⁵ V. O. Tikhomirov,^{96,gg} Yu. A. Tikhonov,^{109,d} S. Timoshenko,⁹⁸ E. Tiouchichine,⁸⁵ P. Tipton,¹⁷⁸
 S. Tisserant,⁸⁵ T. Todorov,⁵ S. Todorova-Nova,¹²⁹ B. Toggerson,⁷ J. Tojo,⁷⁰ S. Tokár,^{146a} K. Tokushuku,⁶⁶ K. Tollefson,⁹⁰
 E. Tolley,⁵⁷ L. Tomlinson,⁸⁴ M. Tomoto,¹⁰³ L. Tompkins,³¹ K. Toms,¹⁰⁵ N. D. Topilin,⁶⁵ E. Torrence,¹¹⁶ H. Torres,¹⁴⁴
 E. Torró Pastor,¹⁶⁹ J. Toth,^{85,hb} F. Touchard,⁸⁵ D. R. Tovey,¹⁴¹ H. L. Tran,¹¹⁷ T. Trefzger,¹⁷⁶ L. Tremblet,³⁰ A. Tricoli,³⁰
 I. M. Trigger,^{161a} S. Trincaz-Duvold,⁸⁰ M. F. Tripiana,¹² W. Trischuk,¹⁶⁰ B. Trocmé,⁵⁵ C. Troncon,^{91a}
 M. Trottier-McDonald,¹⁵ M. Trovatelli,^{136a,136b} P. True,⁹⁰ M. Trzebinski,³⁹ A. Trzupek,³⁹ C. Tsarouchas,³⁰ J. C.-L. Tseng,¹²⁰
 P. V. Tsiareshka,⁹² D. Tsionou,¹³⁸ G. Tsipolitis,¹⁰ N. Tsirintanis,⁹ S. Tsiskaridze,¹² V. Tsiskaridze,⁴⁸ E. G. Tskhadadze,^{51a}
 I. I. Tsukerman,⁹⁷ V. Tsulaia,¹⁵ S. Tsuno,⁶⁶ D. Tsybychev,¹⁵⁰ A. Tudorache,^{26a} V. Tudorache,^{26a} A. N. Tuna,¹²²
 S. A. Tupputi,^{20a,20b} S. Turchikhin,^{99,ff} D. Turecek,¹²⁸ I. Turk Cakir,^{4c} R. Turra,^{91a,91b} P. M. Tuts,³⁵ A. Tykhonov,⁴⁹
 M. Tylmad,^{148a,148b} M. Tyndel,¹³¹ K. Uchida,²¹ I. Ueda,¹⁵⁷ R. Ueno,²⁹ M. Uggetto,⁸⁵ M. Ugland,¹⁴ M. Uhlenbrock,²¹
 F. Ukegawa,¹⁶² G. Unal,³⁰ A. Undrus,²⁵ G. Unel,¹⁶⁵ F. C. Ungaro,⁴⁸ Y. Unno,⁶⁶ C. Unverdorben,¹⁰⁰ D. Urbaniec,³⁵
 P. Urquijo,⁸⁸ G. Usai,⁸ A. Usanova,⁶² L. Vacavant,⁸⁵ V. Vacek,¹²⁸ B. Vachon,⁸⁷ N. Valencic,¹⁰⁷ S. Valentini,^{20a,20b}
 A. Valero,¹⁶⁹ L. Valery,³⁴ S. Valkar,¹²⁹ E. Valladolid Gallego,¹⁶⁹ S. Vallecorsa,⁴⁹ J. A. Valls Ferrer,¹⁶⁹
 W. Van Den Wollenberg,¹⁰⁷ P. C. Van Der Deijl,¹⁰⁷ R. van der Geer,¹⁰⁷ H. van der Graaf,¹⁰⁷ R. Van Der Leeuw,¹⁰⁷
 D. van der Ster,³⁰ N. van Eldik,³⁰ P. van Gemmeren,⁶ J. Van Nieuwkoop,¹⁴⁴ I. van Vulpen,¹⁰⁷ M. C. van Woerden,³⁰
 M. Vanadia,^{134a,134b} W. Vandelli,³⁰ R. Vanguri,¹²² A. Vaniachine,⁶ P. Vankov,⁴² F. Vannucci,⁸⁰ G. Vardanyan,¹⁷⁹ R. Vari,^{134a}
 E. W. Varnes,⁷ T. Varol,⁸⁶ D. Varouchas,⁸⁰ A. Vartapetian,⁸ K. E. Varvell,¹⁵² F. Vazeille,³⁴ T. Vazquez Schroeder,⁵⁴
 J. Veatch,⁷ F. Veloso,^{126a,126c} S. Veneziano,^{134a} A. Ventura,^{73a,73b} D. Ventura,⁸⁶ M. Venturi,¹⁷¹ N. Venturi,¹⁶⁰ A. Venturini,²³
 V. Vercesi,^{121a} M. Verducci,^{134a,134b} W. Verkerke,¹⁰⁷ J. C. Vermeulen,¹⁰⁷ A. Vest,⁴⁴ M. C. Vetterli,^{144,f} O. Viazlo,⁸¹
 I. Vichou,¹⁶⁷ T. Vickey,^{147c,ii} O. E. Vickey Boeriu,^{147c} G. H. A. Viehhauser,¹²⁰ S. Viel,¹⁷⁰ R. Vigne,³⁰ M. Villa,^{20a,20b}
 M. Villaplana Perez,^{91a,91b} E. Vilucchi,⁴⁷ M. G. Vincter,²⁹ V. B. Vinogradov,⁶⁵ J. Virzi,¹⁵ I. Vivarelli,¹⁵¹ F. Vives Vaque,³
 S. Vlachos,¹⁰ D. Vladoiu,¹⁰⁰ M. Vlasak,¹²⁸ A. Vogel,²¹ M. Vogel,^{32a} P. Vokac,¹²⁸ G. Volpi,^{124a,124b} M. Volpi,⁸⁸
 H. von der Schmitt,¹⁰¹ H. von Radziewski,⁴⁸ E. von Toerne,²¹ V. Vorobel,¹²⁹ K. Vorobev,⁹⁸ M. Vos,¹⁶⁹ R. Voss,³⁰
 J. H. Vossebeld,⁷⁴ N. Vranjes,¹³⁸ M. Vranjes Milosavljevic,^{13a} V. Vrba,¹²⁷ M. Vreeswijk,¹⁰⁷ T. Vu Anh,⁴⁸ R. Vuillermet,³⁰
 I. Vukotic,³¹ Z. Vykydal,¹²⁸ P. Wagner,²¹ W. Wagner,¹⁷⁷ H. Wahlberg,⁷¹ S. Wahrmund,⁴⁴ J. Wakabayashi,¹⁰³ J. Walder,⁷²
 R. Walker,¹⁰⁰ W. Walkowiak,¹⁴³ R. Wall,¹⁷⁸ P. Waller,⁷⁴ B. Walsh,¹⁷⁸ C. Wang,^{153,jj} C. Wang,⁴⁵ F. Wang,¹⁷⁵ H. Wang,¹⁵
 H. Wang,⁴⁰ J. Wang,⁴² J. Wang,^{33a} K. Wang,⁸⁷ R. Wang,¹⁰⁵ S. M. Wang,¹⁵³ T. Wang,²¹ X. Wang,¹⁷⁸ C. Wanotayaroj,¹¹⁶
 A. Warburton,⁸⁷ C. P. Ward,²⁸ D. R. Wardrope,⁷⁸ M. Warsinsky,⁴⁸ A. Washbrook,⁴⁶ C. Wasicki,⁴² P. M. Watkins,¹⁸
 A. T. Watson,¹⁸ I. J. Watson,¹⁵² M. F. Watson,¹⁸ G. Watts,¹⁴⁰ S. Watts,⁸⁴ B. M. Waugh,⁷⁸ S. Webb,⁸⁴ M. S. Weber,¹⁷
 S. W. Weber,¹⁷⁶ J. S. Webster,³¹ A. R. Weidberg,¹²⁰ P. Weigell,¹⁰¹ B. Weinert,⁶¹ J. Weingarten,⁵⁴ C. Weiser,⁴⁸ H. Weits,¹⁰⁷
 P. S. Wells,³⁰ T. Wenaus,²⁵ D. Wendland,¹⁶ Z. Weng,^{153,ee} T. Wengler,³⁰ S. Wenig,³⁰ N. Wermes,²¹ M. Werner,⁴⁸ P. Werner,³⁰
 M. Wessels,^{58a} J. Wetter,¹⁶³ K. Whalen,²⁹ A. White,⁸ M. J. White,¹ R. White,^{32b} S. White,^{124a,124b} D. Whiteson,¹⁶⁵
 D. Wicke,¹⁷⁷ F. J. Wickens,¹³¹ W. Wiedenmann,¹⁷⁵ M. Wielers,¹³¹ P. Wienemann,²¹ C. Wiglesworth,³⁶
 L. A. M. Wiik-Fuchs,²¹ P. A. Wijeratne,⁷⁸ A. Wildauer,¹⁰¹ M. A. Wildt,^{42,kk} H. G. Wilkens,³⁰ J. Z. Will,¹⁰⁰ H. H. Williams,¹²²
 S. Williams,²⁸ C. Willis,⁹⁰ S. Willocq,⁸⁶ A. Wilson,⁸⁹ J. A. Wilson,¹⁸ I. Wingerter-Seez,⁵ F. Winklmeier,¹¹⁶ B. T. Winter,²¹
 M. Wittgen,¹⁴⁵ T. Wittig,⁴³ J. Wittkowski,¹⁰⁰ S. J. Wollstadt,⁸³ M. W. Wolter,³⁹ H. Wolters,^{126a,126c} B. K. Wosiek,³⁹
 J. Wotschack,³⁰ M. J. Woudstra,⁸⁴ K. W. Wozniak,³⁹ M. Wright,⁵³ M. Wu,⁵⁵ S. L. Wu,¹⁷⁵ X. Wu,⁴⁹ Y. Wu,⁸⁹ E. Wulf,³⁵
 T. R. Wyatt,⁸⁴ B. M. Wynne,⁴⁶ S. Xella,³⁶ M. Xiao,¹³⁸ D. Xu,^{33a} L. Xu,^{33b,ii} B. Yabsley,¹⁵² S. Yacoob,^{147b,mm} R. Yakabe,⁶⁷
 M. Yamada,⁶⁶ H. Yamaguchi,¹⁵⁷ Y. Yamaguchi,¹¹⁸ A. Yamamoto,⁶⁶ K. Yamamoto,⁶⁴ S. Yamamoto,¹⁵⁷ T. Yamamura,¹⁵⁷
 T. Yamanaka,¹⁵⁷ K. Yamauchi,¹⁰³ Y. Yamazaki,⁶⁷ Z. Yan,²² H. Yang,^{33e} H. Yang,¹⁷⁵ U. K. Yang,⁸⁴ Y. Yang,¹¹¹ S. Yanush,⁹³
 L. Yao,^{33a} W.-M. Yao,¹⁵ Y. Yasu,⁶⁶ E. Yatsenko,⁴² K. H. Yau Wong,²¹ J. Ye,⁴⁰ S. Ye,²⁵ I. Yeletskikh,⁶⁵ A. L. Yen,⁵⁷
 E. Yildirim,⁴² M. Yilmaz,^{4b} R. Yoosoofmiya,¹²⁵ K. Yorita,¹⁷³ R. Yoshida,⁶ K. Yoshihara,¹⁵⁷ C. Young,¹⁴⁵ C. J. S. Young,³⁰
 S. Youssef,²² D. R. Yu,¹⁵ J. Yu,⁸ J. M. Yu,⁸⁹ J. Yu,¹¹⁴ L. Yuan,⁶⁷ A. Yurkewicz,¹⁰⁸ I. Yusuff,^{28,nn} B. Zabinski,³⁹ R. Zaidan,⁶³
 A. M. Zaitsev,^{130,aa} A. Zaman,¹⁵⁰ S. Zambito,²³ L. Zanello,^{134a,134b} D. Zanzi,⁸⁸ C. Zeitnitz,¹⁷⁷ M. Zeman,¹²⁸ A. Zemla,^{38a}
 K. Zengel,²³ O. Zenin,¹³⁰ T. Ženiš,^{146a} D. Zerwas,¹¹⁷ G. Zevi della Porta,⁵⁷ D. Zhang,⁸⁹ F. Zhang,¹⁷⁵ H. Zhang,⁹⁰ J. Zhang,⁶
 L. Zhang,¹⁵³ X. Zhang,^{33d} Z. Zhang,¹¹⁷ Z. Zhao,^{33b} A. Zhemchugov,⁶⁵ J. Zhong,¹²⁰ B. Zhou,⁸⁹ L. Zhou,³⁵ N. Zhou,¹⁶⁵

C. G. Zhu,^{33d} H. Zhu,^{33a} J. Zhu,⁸⁹ Y. Zhu,^{33b} X. Zhuang,^{33a} K. Zhukov,⁹⁶ A. Zibell,¹⁷⁶ D. Ziemska,⁶¹ N. I. Zimine,⁶⁵
 C. Zimmermann,⁸³ R. Zimmermann,²¹ S. Zimmermann,²¹ S. Zimmermann,⁴⁸ Z. Zinonos,⁵⁴ M. Ziolkowski,¹⁴³
 G. Zobernig,¹⁷⁵ A. Zoccoli,^{20a,20b} M. zur Nedden,¹⁶ G. Zurzolo,^{104a,104b} V. Zutshi¹⁰⁸ and L. Zwalski³⁰

(ATLAS Collaboration)

¹*Department of Physics, University of Adelaide, Adelaide, Australia*²*Physics Department, SUNY Albany, Albany, New York, USA*³*Department of Physics, University of Alberta, Edmonton, AB, Canada*^{4a}*Department of Physics, Ankara University, Ankara, Turkey*^{4b}*Department of Physics, Gazi University, Ankara, Turkey*^{4c}*Istanbul Aydin University, Istanbul, Turkey*^{4d}*Division of Physics, TOBB University of Economics and Technology, Ankara, Turkey*⁵*LAPP, CNRS/IN2P3 and Université de Savoie, Annecy-le-Vieux, France*⁶*High Energy Physics Division, Argonne National Laboratory, Argonne, Illinois, USA*⁷*Department of Physics, University of Arizona, Tucson, Arizona, USA*⁸*Department of Physics, The University of Texas at Arlington, Arlington, Texas, USA*⁹*Physics Department, University of Athens, Athens, Greece*¹⁰*Physics Department, National Technical University of Athens, Zografou, Greece*¹¹*Institute of Physics, Azerbaijan Academy of Sciences, Baku, Azerbaijan*¹²*Institut de Física d'Altes Energies and Departament de Física de la Universitat Autònoma de Barcelona, Barcelona, Spain*^{13a}*Institute of Physics, University of Belgrade, Belgrade, Serbia*^{13b}*Vinca Institute of Nuclear Sciences, University of Belgrade, Belgrade, Serbia*¹⁴*Department for Physics and Technology, University of Bergen, Bergen, Norway*¹⁵*Physics Division, Lawrence Berkeley National Laboratory and University of California, Berkeley, California, USA*¹⁶*Department of Physics, Humboldt University, Berlin, Germany*¹⁷*Albert Einstein Center for Fundamental Physics and Laboratory for High Energy Physics, University of Bern, Bern, Switzerland*¹⁸*School of Physics and Astronomy, University of Birmingham, Birmingham, United Kingdom*^{19a}*Department of Physics, Bogazici University, Istanbul, Turkey*^{19b}*Department of Physics, Dogus University, Istanbul, Turkey*^{19c}*Department of Physics Engineering, Gaziantep University, Gaziantep, Turkey*^{20a}*INFN Sezione di Bologna, Italy*^{20b}*Dipartimento di Fisica e Astronomia, Università di Bologna, Bologna, Italy*²¹*Physikalisches Institut, University of Bonn, Bonn, Germany*²²*Department of Physics, Boston University, Boston, Massachusetts, USA*²³*Department of Physics, Brandeis University, Waltham, Massachusetts, USA*^{24a}*Universidade Federal do Rio De Janeiro COPPE/EE/IF, Rio de Janeiro, Brazil*^{24b}*Federal University of Juiz de Fora (UFJF), Juiz de Fora, Brazil*^{24c}*Federal University of Sao Joao del Rei (UFSJ), Sao Joao del Rei, Brazil*^{24d}*Instituto de Fisica, Universidade de Sao Paulo, Sao Paulo, Brazil*²⁵*Physics Department, Brookhaven National Laboratory, Upton, New York, USA*^{26a}*National Institute of Physics and Nuclear Engineering, Bucharest, Romania*^{26b}*National Institute for Research and Development of Isotopic and Molecular Technologies, Physics Department, Cluj Napoca, Romania*^{26c}*University Politehnica Bucharest, Bucharest, Romania*^{26d}*West University in Timisoara, Timisoara, Romania*²⁷*Departamento de Física, Universidad de Buenos Aires, Buenos Aires, Argentina*²⁸*Cavendish Laboratory, University of Cambridge, Cambridge, United Kingdom*²⁹*Department of Physics, Carleton University, Ottawa, ON, Canada*³⁰*CERN, Geneva, Switzerland*³¹*Enrico Fermi Institute, University of Chicago, Chicago, Illinois, USA*^{32a}*Departamento de Física, Pontificia Universidad Católica de Chile, Santiago, Chile*^{32b}*Departamento de Física, Universidad Técnica Federico Santa María, Valparaíso, Chile*^{33a}*Institute of High Energy Physics, Chinese Academy of Sciences, Beijing, China*^{33b}*Department of Modern Physics, University of Science and Technology of China, Anhui, China*^{33c}*Department of Physics, Nanjing University, Jiangsu, China*

- ^{33d}School of Physics, Shandong University, Shandong, China
^{33e}Physics Department, Shanghai Jiao Tong University, Shanghai, China
^{33f}Physics Department, Tsinghua University, Beijing 100084, China
- ³⁴Laboratoire de Physique Corpusculaire, Clermont Université and Université Blaise Pascal and CNRS/IN2P3, Clermont-Ferrand, France
- ³⁵Nevis Laboratory, Columbia University, Irvington, New York, USA
³⁶Niels Bohr Institute, University of Copenhagen, Kobenhavn, Denmark
^{37a}INFN Gruppo Collegato di Cosenza, Laboratori Nazionali di Frascati, Italy
^{37b}Dipartimento di Fisica, Università della Calabria, Rende, Italy
- ^{38a}AGH University of Science and Technology, Faculty of Physics and Applied Computer Science, Krakow, Poland
^{38b}Marian Smoluchowski Institute of Physics, Jagiellonian University, Krakow, Poland
- ³⁹The Henryk Niewodniczanski Institute of Nuclear Physics, Polish Academy of Sciences, Krakow, Poland
- ⁴⁰Physics Department, Southern Methodist University, Dallas, Texas, USA
⁴¹Physics Department, University of Texas at Dallas, Richardson, Texas, USA
⁴²DESY, Hamburg and Zeuthen, Germany
- ⁴³Institut für Experimentelle Physik IV, Technische Universität Dortmund, Dortmund, Germany
⁴⁴Institut für Kern- und Teilchenphysik, Technische Universität Dresden, Dresden, Germany
⁴⁵Department of Physics, Duke University, Durham, North Carolina, USA
- ⁴⁶SUPA - School of Physics and Astronomy, University of Edinburgh, Edinburgh, United Kingdom
⁴⁷INFN Laboratori Nazionali di Frascati, Frascati, Italy
- ⁴⁸Fakultät für Mathematik und Physik, Albert-Ludwigs-Universität Freiburg, Germany
⁴⁹Section de Physique, Université de Genève, Geneva, Switzerland
^{50a}INFN Sezione di Genova, Genova, Italy
^{50b}Dipartimento di Fisica, Università di Genova, Genova, Italy
- ^{51a}E. Andronikashvili Institute of Physics, Iv. Javakhishvili Tbilisi State University, Tbilisi, Georgia
^{51b}High Energy Physics Institute, Tbilisi State University, Tbilisi, Georgia
- ⁵²II Physikalisches Institut, Justus-Liebig-Universität Giessen, Giessen, Germany
- ⁵³SUPA - School of Physics and Astronomy, University of Glasgow, Glasgow, United Kingdom
⁵⁴II Physikalisches Institut, Georg-August-Universität, Göttingen, Germany
- ⁵⁵Laboratoire de Physique Subatomique et de Cosmologie, Université Grenoble-Alpes, CNRS/IN2P3, Grenoble, France
⁵⁶Department of Physics, Hampton University, Hampton, Virginia, USA
- ⁵⁷Laboratory for Particle Physics and Cosmology, Harvard University, Cambridge, Massachusetts, USA
- ^{58a}Kirchhoff-Institut für Physik, Ruprecht-Karls-Universität Heidelberg, Heidelberg, Germany
^{58b}Physikalisches Institut, Ruprecht-Karls-Universität Heidelberg, Heidelberg, Germany
- ^{58c}ZITI Institut für technische Informatik, Ruprecht-Karls-Universität Heidelberg, Mannheim, Germany
- ⁵⁹Faculty of Applied Information Science, Hiroshima Institute of Technology, Hiroshima, Japan
- ^{60a}Department of Physics, The Chinese University of Hong Kong, Shatin, N.T., Hong Kong, China
^{60b}Department of Physics, The University of Hong Kong, Hong Kong, China
- ^{60c}Department of Physics, The Hong Kong University of Science and Technology, Clear Water Bay, Kowloon, Hong Kong, China
⁶¹Department of Physics, Indiana University, Bloomington, Indiana, USA
- ⁶²Institut für Astro- und Teilchenphysik, Leopold-Franzens-Universität Innsbruck, Austria
⁶³University of Iowa, Iowa City, Iowa, USA
- ⁶⁴Department of Physics and Astronomy, Iowa State University, Ames, Iowa, USA
⁶⁵Joint Institute for Nuclear Research, JINR Dubna, Dubna, Russia
- ⁶⁶KEK, High Energy Accelerator Research Organization, Tsukuba, Japan
⁶⁷Graduate School of Science, Kobe University, Kobe, Japan
⁶⁸Faculty of Science, Kyoto University, Kyoto, Japan
⁶⁹Kyoto University of Education, Kyoto, Japan
- ⁷⁰Department of Physics, Kyushu University, Fukuoka, Japan
- ⁷¹Instituto de Física La Plata, Universidad Nacional de La Plata and CONICET, La Plata, Argentina
⁷²Physics Department, Lancaster University, Lancaster, United Kingdom
^{73a}INFN Sezione di Lecce, Lecce, Italy
^{73b}Dipartimento di Matematica e Fisica, Università del Salento, Lecce, Italy
- ⁷⁴Oliver Lodge Laboratory, University of Liverpool, Liverpool, United Kingdom
- ⁷⁵Department of Physics, Jožef Stefan Institute and University of Ljubljana, Ljubljana, Slovenia
- ⁷⁶School of Physics and Astronomy, Queen Mary University of London, London, United Kingdom
⁷⁷Department of Physics, Royal Holloway University of London, Surrey, United Kingdom

- ⁷⁸Department of Physics and Astronomy, University College London, London, United Kingdom
⁷⁹Louisiana Tech University, Ruston, Louisiana, USA
- ⁸⁰Laboratoire de Physique Nucléaire et de Hautes Energies, UPMC and Université Paris-Diderot and CNRS/IN2P3, Paris, France
⁸¹Fysiska institutionen, Lunds universitet, Lund, Sweden
- ⁸²Departamento de Fisica Teorica C-15, Universidad Autonoma de Madrid, Madrid, Spain
⁸³Institut für Physik, Universität Mainz, Mainz, Germany
- ⁸⁴School of Physics and Astronomy, University of Manchester, Manchester, United Kingdom
⁸⁵CPPM, Aix-Marseille Université and CNRS/IN2P3, Marseille, France
- ⁸⁶Department of Physics, University of Massachusetts, Amherst, Massachusetts, USA
⁸⁷Department of Physics, McGill University, Montreal, QC, Canada
⁸⁸School of Physics, University of Melbourne, Victoria, Australia
- ⁸⁹Department of Physics, The University of Michigan, Ann Arbor, Michigan, USA
- ⁹⁰Department of Physics and Astronomy, Michigan State University, East Lansing, Michigan, USA
^{91a}INFN Sezione di Milano, Milano, Italy
^{91b}Dipartimento di Fisica, Università di Milano, Milano, Italy
- ⁹²B.I. Stepanov Institute of Physics, National Academy of Sciences of Belarus, Minsk, Republic of Belarus
⁹³National Scientific and Educational Centre for Particle and High Energy Physics, Minsk, Republic of Belarus
- ⁹⁴Department of Physics, Massachusetts Institute of Technology, Cambridge, Massachusetts, USA
⁹⁵Group of Particle Physics, University of Montreal, Montreal, QC, Canada
⁹⁶P.N. Lebedev Institute of Physics, Academy of Sciences, Moscow, Russia
⁹⁷Institute for Theoretical and Experimental Physics (ITEP), Moscow, Russia
⁹⁸National Research Nuclear University MEPhI, Moscow, Russia
- ⁹⁹D.V. Skobeltsyn Institute of Nuclear Physics, M.V. Lomonosov Moscow State University, Moscow, Russia
¹⁰⁰Fakultät für Physik, Ludwig-Maximilians-Universität München, München, Germany
¹⁰¹Max-Planck-Institut für Physik (Werner-Heisenberg-Institut), München, Germany
¹⁰²Nagasaki Institute of Applied Science, Nagasaki, Japan
- ¹⁰³Graduate School of Science and Kobayashi-Maskawa Institute, Nagoya University, Nagoya, Japan
^{104a}INFN Sezione di Napoli, Napoli, Italy
^{104b}Dipartimento di Fisica, Università di Napoli, Napoli, Italy
- ¹⁰⁵Department of Physics and Astronomy, University of New Mexico, Albuquerque, New Mexico, USA
¹⁰⁶Institute for Mathematics, Astrophysics and Particle Physics, Radboud University Nijmegen/Nikhef, Nijmegen, Netherlands
- ¹⁰⁷Nikhef National Institute for Subatomic Physics and University of Amsterdam, Amsterdam, Netherlands
¹⁰⁸Department of Physics, Northern Illinois University, DeKalb, Illinois, USA
¹⁰⁹Budker Institute of Nuclear Physics, SB RAS, Novosibirsk, Russia
¹¹⁰Department of Physics, New York University, New York, New York, USA
¹¹¹Ohio State University, Columbus, Ohio, USA
¹¹²Faculty of Science, Okayama University, Okayama, Japan
- ¹¹³Homer L. Dodge Department of Physics and Astronomy, University of Oklahoma, Norman, Oklahoma, USA
¹¹⁴Department of Physics, Oklahoma State University, Stillwater, Oklahoma, USA
¹¹⁵Palacký University, RCPMT, Olomouc, Czech Republic
- ¹¹⁶Center for High Energy Physics, University of Oregon, Eugene, Oregon, USA
¹¹⁷LAL, Université Paris-Sud and CNRS/IN2P3, Orsay, France
¹¹⁸Graduate School of Science, Osaka University, Osaka, Japan
¹¹⁹Department of Physics, University of Oslo, Oslo, Norway
- ¹²⁰Department of Physics, Oxford University, Oxford, United Kingdom
^{121a}INFN Sezione di Pavia, Pavia, Italy
^{121b}Dipartimento di Fisica, Università di Pavia, Pavia, Italy
- ¹²²Department of Physics, University of Pennsylvania, Philadelphia, Pennsylvania, USA
¹²³Petersburg Nuclear Physics Institute, Gatchina, Russia
^{124a}INFN Sezione di Pisa, Pisa, Italy
^{124b}Dipartimento di Fisica E. Fermi, Università di Pisa, Pisa, Italy
- ¹²⁵Department of Physics and Astronomy, University of Pittsburgh, Pittsburgh, Pennsylvania, USA
^{126a}Laboratorio de Instrumentacao e Física Experimental de Particulas - LIP, Lisboa, Portugal
^{126b}Faculdade de Ciências, Universidade de Lisboa, Lisboa, Portugal
^{126c}Department of Physics, University of Coimbra, Coimbra, Portugal
^{126d}Centro de Física Nuclear da Universidade de Lisboa, Lisboa, Portugal

- ^{126e}*Departamento de Fisica, Universidade do Minho, Braga, Portugal*
- ^{126f}*Departamento de Fisica Teorica y del Cosmos and CAFPE, Universidad de Granada, Granada (Spain), Portugal*
- ^{126g}*Dep Fisica and CEFITEC of Faculdade de Ciencias e Tecnologia, Universidade Nova de Lisboa, Caparica, Portugal*
- ¹²⁷*Institute of Physics, Academy of Sciences of the Czech Republic, Praha, Czech Republic*
- ¹²⁸*Czech Technical University in Prague, Praha, Czech Republic*
- ¹²⁹*Faculty of Mathematics and Physics, Charles University in Prague, Praha, Czech Republic*
- ¹³⁰*State Research Center Institute for High Energy Physics, Protvino, Russia*
- ¹³¹*Particle Physics Department, Rutherford Appleton Laboratory, Didcot, United Kingdom*
- ¹³²*Physics Department, University of Regina, Regina, SK, Canada*
- ¹³³*Ritsumeikan University, Kusatsu, Shiga, Japan*
- ^{134a}*INFN Sezione di Roma, Roma, Italy*
- ^{134b}*Dipartimento di Fisica, Sapienza Università di Roma, Roma, Italy*
- ^{135a}*INFN Sezione di Roma Tor Vergata, Roma, Italy*
- ^{135b}*Dipartimento di Fisica, Università di Roma Tor Vergata, Roma, Italy*
- ^{136a}*INFN Sezione di Roma Tre, Roma, Italy*
- ^{136b}*Dipartimento di Matematica e Fisica, Università Roma Tre, Roma, Italy*
- ^{137a}*Faculté des Sciences Ain Chock, Réseau Universitaire de Physique des Hautes Energies - Université Hassan II, Casablanca, Morocco*
- ^{137b}*Centre National de l'Energie des Sciences Techniques Nucleaires, Rabat, Morocco*
- ^{137c}*Faculté des Sciences Semlalia, Université Cadi Ayyad, LPHEA-Marrakech, Morocco*
- ^{137d}*Faculté des Sciences, Université Mohamed Premier and LPTPM, Oujda, Morocco*
- ^{137e}*Faculté des sciences, Université Mohammed V-Agdal, Rabat, Morocco*
- ¹³⁸*DSM/IRFU (Institut de Recherches sur les Lois Fondamentales de l'Univers), CEA Saclay (Commissariat à l'Energie Atomique et aux Energies Alternatives), Gif-sur-Yvette, France*
- ¹³⁹*Santa Cruz Institute for Particle Physics, University of California Santa Cruz, Santa Cruz, California, USA*
- ¹⁴⁰*Department of Physics, University of Washington, Seattle, Washington, USA*
- ¹⁴¹*Department of Physics and Astronomy, University of Sheffield, Sheffield, United Kingdom*
- ¹⁴²*Department of Physics, Shinshu University, Nagano, Japan*
- ¹⁴³*Fachbereich Physik, Universität Siegen, Siegen, Germany*
- ¹⁴⁴*Department of Physics, Simon Fraser University, Burnaby, BC, Canada*
- ¹⁴⁵*SLAC National Accelerator Laboratory, Stanford, California, USA*
- ^{146a}*Faculty of Mathematics, Physics & Informatics, Comenius University, Bratislava, Slovak Republic*
- ^{146b}*Department of Subnuclear Physics, Institute of Experimental Physics of the Slovak Academy of Sciences, Kosice, Slovak Republic*
- ^{147a}*Department of Physics, University of Cape Town, Cape Town, South Africa*
- ^{147b}*Department of Physics, University of Johannesburg, Johannesburg, South Africa*
- ^{147c}*School of Physics, University of the Witwatersrand, Johannesburg, South Africa*
- ^{148a}*Department of Physics, Stockholm University, Stockholm, Sweden*
- ^{148b}*The Oskar Klein Centre, Stockholm, Sweden*
- ¹⁴⁹*Physics Department, Royal Institute of Technology, Stockholm, Sweden*
- ¹⁵⁰*Departments of Physics & Astronomy and Chemistry, Stony Brook University, Stony Brook, New York, USA*
- ¹⁵¹*Department of Physics and Astronomy, University of Sussex, Brighton, United Kingdom*
- ¹⁵²*School of Physics, University of Sydney, Sydney, Australia*
- ¹⁵³*Institute of Physics, Academia Sinica, Taipei, Taiwan*
- ¹⁵⁴*Department of Physics, Technion: Israel Institute of Technology, Haifa, Israel*
- ¹⁵⁵*Raymond and Beverly Sackler School of Physics and Astronomy, Tel Aviv University, Tel Aviv, Israel*
- ¹⁵⁶*Department of Physics, Aristotle University of Thessaloniki, Thessaloniki, Greece*
- ¹⁵⁷*International Center for Elementary Particle Physics and Department of Physics, The University of Tokyo, Tokyo, Japan*
- ¹⁵⁸*Graduate School of Science and Technology, Tokyo Metropolitan University, Tokyo, Japan*
- ¹⁵⁹*Department of Physics, Tokyo Institute of Technology, Tokyo, Japan*
- ¹⁶⁰*Department of Physics, University of Toronto, Toronto, ON, Canada*
- ^{161a}*TRIUMF, Vancouver, BC, Canada*
- ^{161b}*Department of Physics and Astronomy, York University, Toronto, ON, Canada*
- ¹⁶²*Faculty of Pure and Applied Sciences, University of Tsukuba, Tsukuba, Japan*
- ¹⁶³*Department of Physics and Astronomy, Tufts University, Medford, Massachusetts, USA*
- ¹⁶⁴*Centro de Investigaciones, Universidad Antonio Narino, Bogota, Colombia*

¹⁶⁵*Department of Physics and Astronomy, University of California Irvine, Irvine, California, USA*^{166a}*INFN Gruppo Collegato di Udine, Sezione di Trieste, Udine, Italy*^{166b}*ICTP, Trieste, Italy*^{166c}*Dipartimento di Chimica, Fisica e Ambiente, Università di Udine, Udine, Italy*¹⁶⁷*Department of Physics, University of Illinois, Urbana, Illinois, USA*¹⁶⁸*Department of Physics and Astronomy, University of Uppsala, Uppsala, Sweden*¹⁶⁹*Instituto de Física Corpuscular (IFIC) and Departamento de Física Atómica, Molecular y Nuclear and Departamento de Ingeniería Electrónica and Instituto de Microelectrónica de Barcelona (IMB-CNM), University of Valencia and CSIC, Valencia, Spain*¹⁷⁰*Department of Physics, University of British Columbia, Vancouver, BC, Canada*¹⁷¹*Department of Physics and Astronomy, University of Victoria, Victoria, BC, Canada*¹⁷²*Department of Physics, University of Warwick, Coventry, United Kingdom*¹⁷³*Waseda University, Tokyo, Japan*¹⁷⁴*Department of Particle Physics, The Weizmann Institute of Science, Rehovot, Israel*¹⁷⁵*Department of Physics, University of Wisconsin, Madison, Wisconsin, USA*¹⁷⁶*Fakultät für Physik und Astronomie, Julius-Maximilians-Universität, Würzburg, Germany*¹⁷⁷*Fachbereich C Physik, Bergische Universität Wuppertal, Wuppertal, Germany*¹⁷⁸*Department of Physics, Yale University, New Haven, Connecticut, USA*¹⁷⁹*Yerevan Physics Institute, Yerevan, Armenia*¹⁸⁰*Centre de Calcul de l'Institut National de Physique Nucléaire et de Physique des Particules (IN2P3), Villeurbanne, France*^aDeceased.^bAlso at Department of Physics, King's College London, London, United Kingdom.^cAlso at Institute of Physics, Azerbaijan Academy of Sciences, Baku, Azerbaijan.^dAlso at Novosibirsk State University, Novosibirsk, Russia.^eAlso at Particle Physics Department, Rutherford Appleton Laboratory, Didcot, United Kingdom.^fAlso at TRIUMF, Vancouver, BC, Canada.^gAlso at Department of Physics, California State University, Fresno, CA, USA.^hAlso at Tomsk State University, Tomsk, Russia.ⁱAlso at CPPM, Aix-Marseille Université and CNRS/IN2P3, Marseille, France.^jAlso at Università di Napoli Parthenope, Napoli, Italy.^kAlso at Institute of Particle Physics (IPP), Canada.^lAlso at Department of Physics, St. Petersburg State Polytechnical University, St. Petersburg, Russia.^mAlso at Department of Financial and Management Engineering, University of the Aegean, Chios, Greece.ⁿAlso at Louisiana Tech University, Ruston, LA, USA.^oAlso at Institutio Catalana de Recerca i Estudis Avancats, ICREA, Barcelona, Spain.^pAlso at Department of Physics, The University of Texas at Austin, Austin, TX, USA.^qAlso at Institute of Theoretical Physics, Ilia State University, Tbilisi, Georgia.^rAlso at CERN, Geneva, Switzerland.^sAlso at Ochadai Academic Production, Ochanomizu University, Tokyo, Japan.^tAlso at Manhattan College, New York, NY, USA.^uAlso at Institute of Physics, Academia Sinica, Taipei, Taiwan.^vAlso at LAL, Université Paris-Sud and CNRS/IN2P3, Orsay, France.^wAlso at Academia Sinica Grid Computing, Institute of Physics, Academia Sinica, Taipei, Taiwan.^xAlso at Laboratoire de Physique Nucléaire et de Hautes Energies, UPMC and Université Paris-Diderot and CNRS/IN2P3, Paris, France.^yAlso at School of Physical Sciences, National Institute of Science Education and Research, Bhubaneswar, India.^zAlso at Dipartimento di Fisica, Sapienza Università di Roma, Roma, Italy.^{aa}Also at Moscow Institute of Physics and Technology State University, Dolgoprudny, Russia.^{bb}Also at Section de Physique, Université de Genève, Geneva, Switzerland.^{cc}Also at International School for Advanced Studies (SISSA), Trieste, Italy.^{dd}Also at Department of Physics and Astronomy, University of South Carolina, Columbia, SC, USA.^{ee}Also at School of Physics and Engineering, Sun Yat-sen University, Guangzhou, China.^{ff}Also at Faculty of Physics, M.V. Lomonosov Moscow State University, Moscow, Russia.^{gg}Also at National Research Nuclear University MEPhI, Moscow, Russia.^{hh}Also at Institute for Particle and Nuclear Physics, Wigner Research Centre for Physics, Budapest, Hungary.ⁱⁱAlso at Department of Physics, Oxford University, Oxford, United Kingdom.

^{jj} Also at Department of Physics, Nanjing University, Jiangsu, China.

^{kk} Also at Institut für Experimentalphysik, Universität Hamburg, Hamburg, Germany.

^{ll} Also at Department of Physics, The University of Michigan, Ann Arbor, MI, USA.

^{mm} Also at Discipline of Physics, University of KwaZulu-Natal, Durban, South Africa.

ⁿⁿ Also at University of Malaya, Department of Physics, Kuala Lumpur, Malaysia.